Transport of Laser-Ablated Impurities in TCV

by

Edgar Scavino

Laurea in Ingegneria Nucleare, Politecnico di Torino

A thesis presented to the Physics Department

Ecole Polytechnique Fédérale de Lausanne

for the degree of

Docteur ès Sciences

submitted February 2003

Thesis Director: Dr. Henri Weisen

Version abrégée

La compréhension du transport des impuretés dans les plasmas confinés magnetiquement est une question cruciale pour l'optimisation d'un futur réacteur à fusion thermonucléaire. Les ions de petite à moyenne charge atomique comme le carbone, l'oxygène et les métaux sont présents dans presque tous les plasmas de tokamak, et la production d'hélium sera une conséquence intrinsèque des réactions de fusion. Le rayonnement dû aux impuretés jouera un rôle crucial dans le bilan de puissance dans les réacteurs de fusion. Le Tokamak à Configuration Variable (TCV) a fourni, pour ce travail, des plasmas-cible dans lesquels des impuretés à faible taux de recyclage ont été injectées en faibles quantité et instants connus. La capacité de TCV à produire des plasmas d'une grande variété de formes a permis l'étude de la géométrie du plasma sur le transport des impuretés.

Un ensemble étendu de diagnostics a été utilisé pour mesurer l'évolution de la concentration des impuretés après l'ablation et l'injection dans le plasma. Le système d'ablation des impuretés, qui utilise un laser à rubis pulsé, a été construit, mis en opération et systématiquement exploité pour la réalisation de cette thèse. Le système de photodiodes pour rayons x-mous (SXR) à 200 canaux a été le diagnostic clé pour la mesure de la radiation provenant du centre du plasma, et un spectromètre SPRED a été utilisé pour la détection des émissions dans l'ultraviolet rayonnées par des atomes partiellement ionisés au bord du plasma. Un certain nombre d'outils d'analyse ont été utilisés, notamment la technique GSVD pour séparer les signaux provenant des impuretés de la contribution à dents-de-scie des particules du plasma. Egalement on a exploité des techniques standard d'inversion tomographique pour la détermination de la densité de puissance rayonnée par les impuretés, et des routines d'ajustage de paramètres pour l'évaluation de la décroissance exponentielle des signaux qui est reliée au temps de confinement des impuretés. Le code 1D STRAHL a été largement utilisé pour la reproduction de l'évolution temporelle des signaux SXR en fonction des paramètres mesurés des plasmas et de profils radiaux choisis de la diffusivité et de la vitesse de convection des impuretés. Ces profils ont été changés par des routines d'ajustage de paramètres pour déterminer les valeurs pour lesquelles les signaux simulés reproduisent le mieux les observations expérimentales.

Afin d'étudier les effets de la géométrie du plasma sur le transport, l'élongation et la trian-

gularité ont été balayées en séries de décharges dédiées de plasmas ohmiques, limités, au mode de bas confinement (mode L). Les effets de la géométrie sont évidents dans les deux balayages. Le confinement des impuretés suit les mêmes tendances que celui de l'énergie des électrons dans le balayage de triangularité; cependant une augmentation de l'élongation du plasma entraîne une réduction du temps de confinement des impuretés alors que celui de la chaleur reste sensiblement constant. Ce résultat pourrait avoir une grande importance dans le cadre d'un réacteur à fusion, où la limitation de la concentration d'impuretés dans le centre du plasma constituera une exigence crucial. En plus, ces balayages ont conduit à l'observation que le temps de confinement des impuretés décroît à champs magnétique élevé, en désaccord avec ce qu'on pourrait attendre à priori.

Des investigations ultérieures ont été effectuées avec le code STRAHL. La simulation numérique a permis de découvrir que les propriétés du confinement des impuretés dans TCV sont très sensibles au transport en périphérie du plasma. L'activité de dents-de-scie au centre s'est révélée moins déterminante sur le confinement, bien qu'elle soit localement dominante sur les autres formes de transport. La vitesse de convection, dans toutes les situations explorées, s'est avérée positive, c'est à dire dirigé vers l'extérieur du plasma, en désaccord avec les observations effectuées sur autres tokamaks et avec les prédictions de la théorie néoclassique du transport.

En conclusion, les possibilités du TCV de produire plasmas fortement façonnés ont été exploitées pour l'investigation des effets de la géométrie sur les propriété de transport des impuretés pour un ensemble de plasmas. Les faibles valeurs du temps de confinement à hautes élongations pourraient être attrayantes pour le projet de réacteurs avancés, si les mêmes tendances seront confirmées dans les régimes d'opération et de chauffage appropriés.

Abstract

Understanding the transport of impurities in magnetically confined plasmas is a crucial issue for the optimization of a future thermonuclear fusion reactor. Light and moderate-Z ions, like carbon, oxygen or metals are constituents of almost all tokamak plasmas, and the production of He ash will be an intrinsic consequence of fusion reactions. The radiation of impurities will have a crucial role in the power balance of any fusion reactor. The Tokamak à Configuration Variable (TCV) has been used to produce target plasmas for the injection of trace, non recycling impurities in known quantity at known times. The unique capability of TCV in producing various plasma shapes has allowed the study of the effect of the plasma geometry on the impurity transport.

A set of diagnostics have been exploited to produce the impurities and monitor the evolution of their concentration after injection in plasmas. The impurity production system, using a single pulse ruby laser, was built, commissioned and systematically exploited for the realisation of this work. The key diagnostic was the 200-channel soft x-ray (SXR) photodiode array for measuring the radiation from the plasma core, while a SPRED spectrometer was used for monitoring the ultraviolet emission from partially stripped ions at the plasma edge. A number of analysis tools have been used, namely the GSVD technique to separate the impurity contribution to the signal from the sawtoothing background from the plasma particles, standard techniques of tomographic inversion, fit routines for the evaluation of the confinement time of impurities. The 1D code STRAHL has been widely used in order to reproduce the time evolution of the line integrated SXR signals as a function of the measured plasma parameters and of ad-hoc profiles of the impurity radial diffusivity and convective velocity. These profiles were changed by bestfitting routines in order to find the values for which the reconstructed signals best matched the experimental observations.

For the study of transport on plasma geometry, the elongation and the triangularity were explored in series of dedicated discharges of ohmic L-mode limiter plasmas. The effect of geometry is evident in both scans, the confinement being in agreement with the electron energy in the case of variation of triangularity, while an increase of the plasma elongation leads to a reduction of the confinement time of impurities without affecting that of heat. Such a result could be useful in environments like a fusion reactor in which one of the main requirements

will surely be the limitation of impurity concentrations in the plasma core. These scans have led to the observation that the impurity confinement time decreases with increasing magnetic field.

Further investigation on these results has been performed using the 1D simulation code STRAHL. This numerical simulation allowed to verify that the confinement properties of impurities in TCV plasmas are more sensitive to the transport in the peripheral region, the central sawtoothing activity being less relevant, even if locally dominant over other forms of transport. Surprisingly, the convective velocity at the plasma edge has been always found to be directed outward, in disagreement with observations made on other tokamaks and with the predictions of the neoclassical theory of transport.

In conclusion, the extreme shaping possibilities of the TCV tokamak have been exploited for the investigation of the effects of the plasma geometry on the transport of impurities for a class of plasmas. The low values of the confinement times at high elongations may be attracting for the designs of advanced reactors, if confirmed in the relevant auxiliary heated and current driven regimes.

Table of Contents

1. INTRODUCTION

1.1 Nuclear fusion

The global need of primary energy is constantly increasing in concert with the growth of the world population and economy. The consumption of petroleum, coal, natural gas, and electrical energy of hydro, nuclear, geothermal, solar and wind origin increases with a rate of a few percent per year[1], being around $4.0*10^{20}$J/year in 1997. All kinds of projections foresee a substantial increase of energy consumption for the next 20 to 30 years, predicting an average rise of 50% for 2020.

Fuel	Proven Reserves	Years of use at current consumption
Coal	$1.0\ 10^{12}$ tons	270
Crude Oil	$950\ 10^{9}$ barrels	40-50
Natural gas	$120\ 10^{12}$ m^3	60-70
Uranium	$2.0\ 10^{6}$ tons	2400-3000 (^{235}U + ^{238}U in fast breeder reactors)

Table 1.1: Estimated world energy reserves

These amounts of proven fossil reserves[2] cannot provide a sustainable development on time scales of thousands of years. Moreover it is clear that the necessary amount of energy cannot be supplied by fuels which would release gigantic quantities of CO_2 in the decades to come. The global warming of the planet due to greenhouse effect[3] can be expected to produce dramatic climate changes, and new sources of energy are nevertheless required to meet the world demand.

One promising option for the future is controlled thermonuclear fusion, which is considered to be a long term environmentally friendly energy source. The fact that a nuclear fusion plant would produce almost no high Z long-lived radioactive waste and the intrinsic safety in the control of the reaction, together with the abundance of fuel in nature, will probably win the public acceptance of such a technology.

Among the nuclear reactions which can easily be produced on earth, the most promising is the deuterium-tritium fusion reaction, which shows the highest cross section for relatively low energies:

$$D + T \rightarrow He^4(3.5MeV) + n(14.1MeV) \tag{1.1}$$
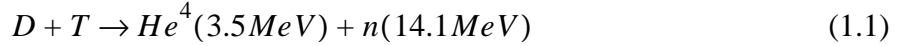
The peak of the rate coefficient, $\langle \sigma(v)v \rangle \approx 10^{-22} m^3 s^{-1}$, is obtained at temperatures around 10keV, thus easily accessible with the present technology.

The deuterium has a natural abundance in hydrogen of 1 part in 6700 and consequently is a plentiful resource in water. While the oceans could provide enough deuterium for several millions years, covering the global electricity production, tritium does not exist in nature, being radioactive with a half life of 12.3 years. However it can be produced from lithium by means of the following nuclear reactions:

$$Li^6 + n \rightarrow He^4 + T + 4.8MeV \tag{1.2}$$

$$Li^7 + n \rightarrow T + He^4 + n + 2.5MeV \tag{1.3}$$
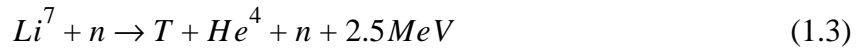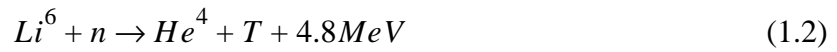
and in principle it could be bred in fusion reactors. Lithium being very abundant in the earth crust and in the sea water, fuel for fusion is potentially available for millions of years[4].

1.2 Magnetic confinement and tokamaks

At the temperatures required for nuclear fusion to occur, the hydrogen isotopes are fully ionised. The electrostatic charge of the positive nuclei is compensated by an equal negative charge by electrons, resulting in a neutral gas called plasma. In order to maintain the integrity of the containing machine, as well as the purity and temperature of the plasma, the contact to material walls has to be minimised. The plasma being composed by charged particles, a magnetic field can provide the necessary confinement. Due to the Lorentz force, a ion or an electron follows a helical path when moving in a magnetic field. While the parallel velocity is not affected, in perpendicular direction the trajectory has a radial extent, or gyro-radius, given by:

$$\rho = \frac{mv_\perp}{qB} \tag{1.4}$$

with $v_\perp$ being the velocity perpendicular to the magnetic field B.

The particle motion is thus restricted to follow the direction of the magnetic field, which is the basis of magnetic confinement. However, in a linear configuration with open ends the magnetic field lines escape out of the vessel at both sides, and consequently such a device

suffers from plasma losses.

The simplest way to overcome the edge losses is to close the magnetic field lines, producing a toroidal configuration. The original idea of the tokamak (from the russian "Toroidalnaya Kamera Magnitnaya Katuschka", meaning toroidal chamber with magnetic coils) was proposed in the early 1950s by Igor Tamm and Andrei Sakharov. In 1968, in the frame of a research led by Lev Artsimovich, a tokamak at the Kurchatov Institute produced much higher plasma temperatures than in any other magnetic configuration at that time[5].Confirmation of such result by independent groups led to a boom of tokamak experiments.
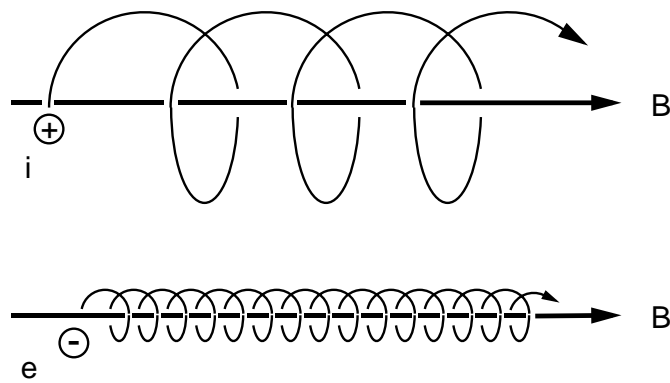
Fig.1.1 - Trajectories of charged particles in a homogeneous magnetic field B

The toroidal magnetic field alone is not sufficient to produce plasma stability, as the radial gradient and the curvature of the magnetic field would induce a vertical drift which would displace the electrons and ion in opposite direction. The charge separation generates an electric field $\vec{E}$ perpendicular to the toroidal magnetic field and causes an outward $\vec{E} \times \vec{B}$-drift motion which expands the plasma ring.

This problem is overcome by twisting the field lines to an helical configuration by means of a poloidal field, so that each field line passes the upper and lower part of the torus. Thus, an averaging along the path of particles leads to a cancelling of the vertical drift motion and avoids the build up of an electrical field. In tokamaks, the poloidal component of the field, B_p, is produced by a current flow in the plasma itself. The current is usually generated by transformer effect, in which the plasma acts as a single secondary winding, while a central solenoid acts as the primary turns. In addition to the toroidal and the poloidal components of the magnetic field, a vertical magnetic field produced by external toroidal coils is required to

balance hoop forces arising from the radial decrease of the magnetic field pressure which tend to expand the plasma along its minor radius.

The magnetic structure of a tokamak plasma consists of an infinite set of nested magnetic surfaces, called *flux surfaces*, which can be labelled by means of the toroidal or poloidal fluxes of the magnetic field. A widely used univocal labelling is provided by the following expression:

$$\rho_{pol} = \sqrt{\frac{\Psi - \Psi_{axis}}{\Psi_{LCFS} - \Psi_{axis}}} \qquad (1.5)$$

in which the poloidal magnetic flux is defined:

$$\psi = \int_{A_{tor}} \vec{B}\vec{ds} \qquad (1.6)$$

with A_{tor} being an arbitrary toroidal cross section of a flux surface.

The twist of the field lines in each surface is characterised by the so-called *safety factor q*, defined for a general geometry as:

$$q = \frac{1}{2\pi}\oint \frac{1}{R}\frac{B_{\varphi}}{B_p}ds \qquad (1.7)$$

The integral is carried out along a single poloidal circuit around the flux surface, and the ratio B_{φ}/B_p can be identified as the pitch of the field line. The safety factor can be identified as
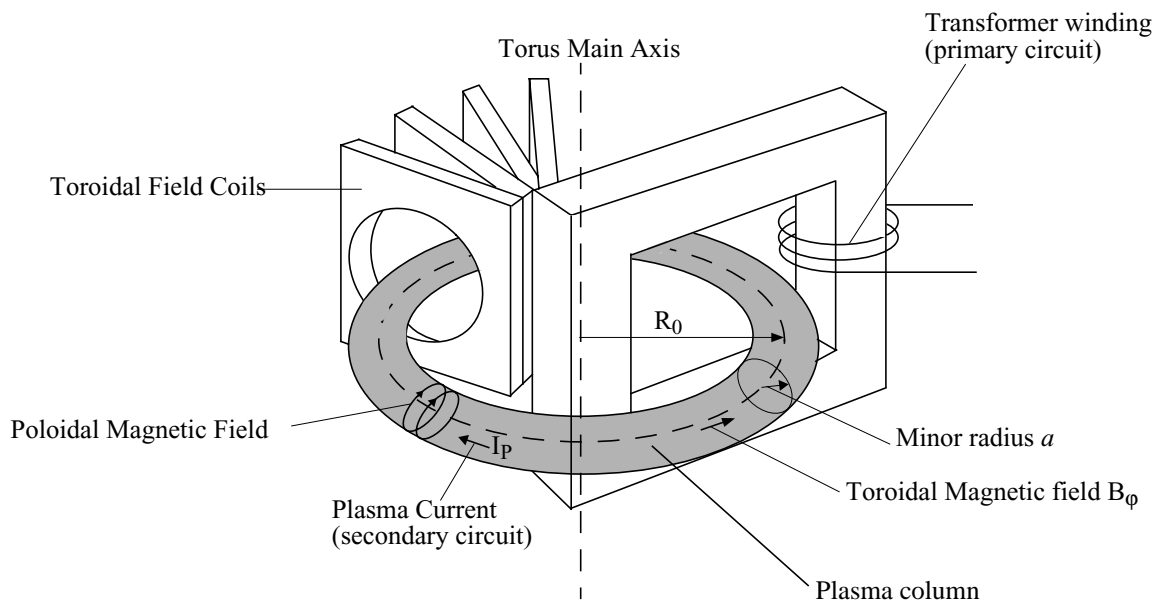

Fig.1.2 - Schematics of a tokamak. The plasma is the single secondary loop of a transformer. The induced plasma current is necessary for a stable confinement.

the number of toroidal turns a field line needs to perform a single poloidal turn, and for large aspect-ratio tokamak the following approximation holds:

$$q = \frac{r}{R_0}\frac{B_\varphi}{B_p} \qquad (1.8)$$

While the tokamak configuration has the advantage of retaining the toroidal symmetry, the production of plasma current by induction allows only pulsed operation. Nevertheless, the plasma current is used as a basic means of heating the plasma to temperatures up to a few keV in large devices, but this method is ineffective for higher temperatures and hence additional heating is necessary for fusion to occur. A limitation to such heating is the rapid decrease of the plasma resistivity, which is mainly proportional to $T_e^{-3/2}$. Moreover, the maximum plasma current is limited by an ideal kink instability which imposes $q_{edge} > 2$.

1.3 Fusion plant considerations

In a fusion power plant, the temperature of the D-T mixture is in general sustained jointly by the injection of power by means of a particle beam or electromagnetic radiation, and by the the energy transfer of the 3.5MeV α-particles which are produced by the fusion reaction of Eq.(1.1). A fusion power multiplication factor Q is defined, as the ratio of the fusion power of the α-particles divided by the externally injected power density.

Being charged, the α-particles are confined in the plasma by the magnetic field and can transfer their energy by means of Coulomb collisions. It is important that their confinement is good enough to allow them to equilibrate the plasma thermal energy in the bulk before leaving the plasma.

In contrast to the α-particles, the neutrons have no interactions with the plasma and the magnetic field, and will be consequently absorbed in a lithium blanket surrounding the reactor vessel. The neutrons, reacting with lithium according to Eq.(1.2) and (1.3), will breed the necessary tritium for plasma refuelling, and their energy will be transferred to suitable coolants for the ultimate generation of electricity.

While the minimum economically useful Q value is $Q = 1$ [6], the most desirable operating mode for a fusion plant reactor is at $Q = \infty$, where the plasma temperature is sustained only by the energy deposition of fusion α-particles; this state is referred to as equilibrium ignition condition. In order for ignition to occur, the following power balance gives an estimate of the

requirement of a fusion reaction. The reaction rate for a 50%-50% mixture of deuterium and tritium is calculated by averaging the cross section, σ_{D-T}, over a thermal velocity distribution:

$$R_{D-T} = \frac{1}{4}n^2\langle\sigma_{D-T}v\rangle_v \tag{1.9}$$

with n being the total ion density. The heating power density from α-particles is then given by $p_\alpha = R_{D-T}E_\alpha$, where E_α is the kinetic energy of a generated α-particle. The energy loss can be expressed by the energy confinement time τ_E:

$$P_{loss} = \frac{W}{\tau_E} = \frac{\int 3nTdV}{\tau_E} \tag{1.10}$$

In Eq.(1.10) the total energy W is expressed by the volume integral of the energy density, which is given by $\frac{1}{2}nT$ multiplied by 3 degrees of freedom for ion and electrons.

Taking constant electron density and temperature for simplicity, the following condition for ignition can be derived:

$$n\tau_E > \frac{12}{\langle\sigma_{D-T}v\rangle_v}\frac{T}{E_\alpha} \tag{1.11}$$

The condition for the product density and temperature has a broad minimum around 30keV, around which $\langle\sigma_{D-T}v\rangle_v = 1.1 \cdot 10^{-24}T^2$ m^3/s, T in keV, within a 10% approximation. The substitution of this value in Eq.(1.11) leads to the ignition criterion for the triple product[4]:

$$\hat{n}\hat{T}\hat{\tau}_E > 5 \cdot 10^{21} \text{ m}^{-3} \text{ keV s} \tag{1.12}$$

which refers to the peak values of density and temperature for parabolic profiles.

Fig.1.3 shows how the experimental achieved triple product has approached the reactor requirement over the years. However, the condition emerging from Eq.(1.12) is an approximation, as it depends not only on the shape of the density and temperature profiles, but also on the presence of impurities and helium ashes in plasma.

The criterion for ignition in Eq.(1.12) shows that high densities at high plasma temperatures are essential to meet the condition for a fusion power plant. Increasing the plasma pressure $p = nT$ means advancing towards economical power plant conditions. The dimensionless parameter beta:

$$\beta = \frac{\langle p\rangle}{B_0^2/2\mu_0} \tag{1.13}$$

with $\langle \ \rangle$ denoting the volume average, is particularly important since it is used as a figure of merit for the efficiency of a tokamak. While the plasma pressure is related to the possibility of achieving fusion, the size and price of the machine depends on the value of the magnetic field. The achievable beta is limited by magnetohydrodynamic instabilities in the plasma. It has been shown[7] that the following semi-empirical ideal beta limit applies:

$$\beta \leq c_T \frac{I[\text{MA}]}{a[\text{m}]B[\text{T}]} \tag{1.14}$$

with c_T being a constant in the range $0.028 < c_T < 0.035$. This limit has been verified experimentally in various tokamaks for a range of shapes and aspect ratios. As the total plasma current I is itself limited by the stability requirement $q_a > 2$, the maximum plasma pressure and consequently the triple product of Eq.(1.12) are set by the value of the magnetic field B.
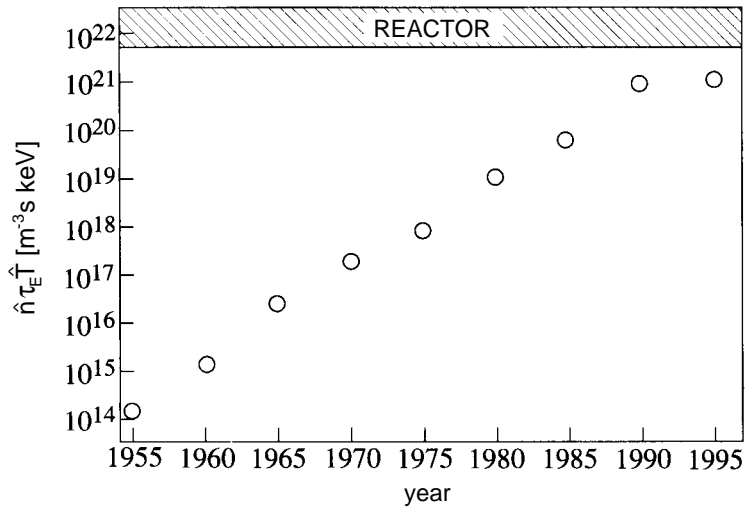
Fig.1.3 - Progress in increasing the triple product $\hat{n}\hat{T}\hat{\tau}_E$ over the years, leading towards reactor conditions.

In this frame, the presence of impurities in a fusion plasma plays a fundamental role in the so-called fuel dilution, as an increased impurity density generally implies a reduction of the fuel density. Ideally, the replacement of a single hydrogen ion with an impurity of charge Z would increase the electron density and hence the total plasma pressure. The same total pressure would be obtained with the removal of $(Z + 1)/2$ hydrogen ions.

A more refined evaluation of the ignition criterion must take into account not only the dilution of density of the D-T fuel in the plasma core, but also the increase in plasma radiation

which is reflected in a different and lower value of the energy confinement time τ_E.

For an impurity concentration $f_Z = n_Z/n_e$ the ratio between the density of the impurity of charge Z and the electron density, the heating power density from α-particles is then given by:

$$p_\alpha = \frac{1}{4}E_\alpha n_e^2(1-fZ)^2\langle\sigma_{D-T}v\rangle_v \tag{1.15}$$

in which the dilution of fuel has been taken into account. The power loss density is increased by the electromagnetic emission from impurities, which consists mainly of bremsstrahlung at the typical temperatures of fusion plasmas in a reactor machine, except for very high Z elements, which would not be completely stripped:

$$p_{loss} = \frac{3n_eT}{\tau_E} + bn_e(n_D+n_T)T^{1/2} + bZ^2n_en_ZT^{1/2} \tag{1.16}$$

It has to be stressed that this constitutes only a lower limit, as different radiation processes (recombination, charge-exchange, line emission) are not taken into account in these calculations.

The requirement $p_\alpha > p_{loss}$ necessary to yield the plasma ignition leads to the relation[8]:

$$n_e\tau_E > \frac{3T}{\frac{1}{4}(1-fZ)^2\langle\sigma_{D-T}v\rangle_vE_\alpha - bT^{1/2}(1-fZ+fZ^2)} \tag{1.17}$$

It is interesting to evaluate the ratio between the power loss due to bremsstrahlung and the power provided by α-particles for a plasma temperature of 10keV:

$$\frac{p_{BS}}{p_\alpha} \sim 0.107\frac{(1-fZ+fZ^2)}{(1-fZ)^2} \tag{1.18}$$

In Fig.1.4 the ratio of Eq.(1.18) is plotted versus concentrations of Fe, O, He which can be typically found in a fusion plasma. It is remarkable how a few percent of such impurities can waste the whole power produced by fusion and prevent ignition. In the case of a pure deuterium/tritium plasma, for which $f = 0$, it would be found $\frac{p_{BS}}{p_\alpha} \sim 0.107$ indi-
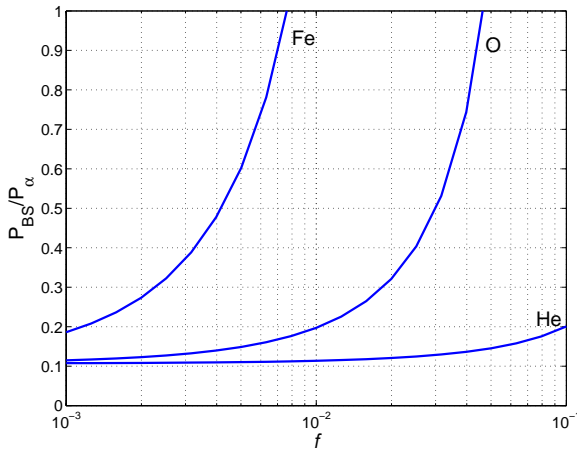

Fig.1.4 - Ratio between the power lost by bremsstrahlung from impurities and the power generated by α-particles of fusion origin, for a 50-50% D-T plasma at the temperature of 10keV.

cating that, in a ignition configuration, 10% of the fusion power is lost by bremsstrahlung of electrons colliding against the deuterium ions.

The maximum permitted impurity fraction in a fusion plasma, or critical fraction f_{Zc}, depends on the required multiplication factor Q, on the plasma temperature and on the impurity species. Such dependencies are discussed in Refs.[6, 8] in which a zero-dimensional power balance, based on the corona model (described in Section 2.1.3), has been applied. Moreover, in those cases for which Q has a finite value, the plasma heating has been considered to be performed by a deuterium beam. For a given value of Q, including ignition ($Q = \infty$) the critical fraction f_{Zc} is principally due to the fuel dilution in the case of light elements, while for heavier ones it is due to the strong radiation emission. In both cases, a higher value of Q implies lower values of f_{Zc}. For a given plasma temperature f_{Zc} scales as $Z^{-2.2 \div -2.5}$, while for increasing temperature the critical fraction increases thanks to the higher fusion reactivity and to the reduced radiation emission of partially stripped impurity ions.
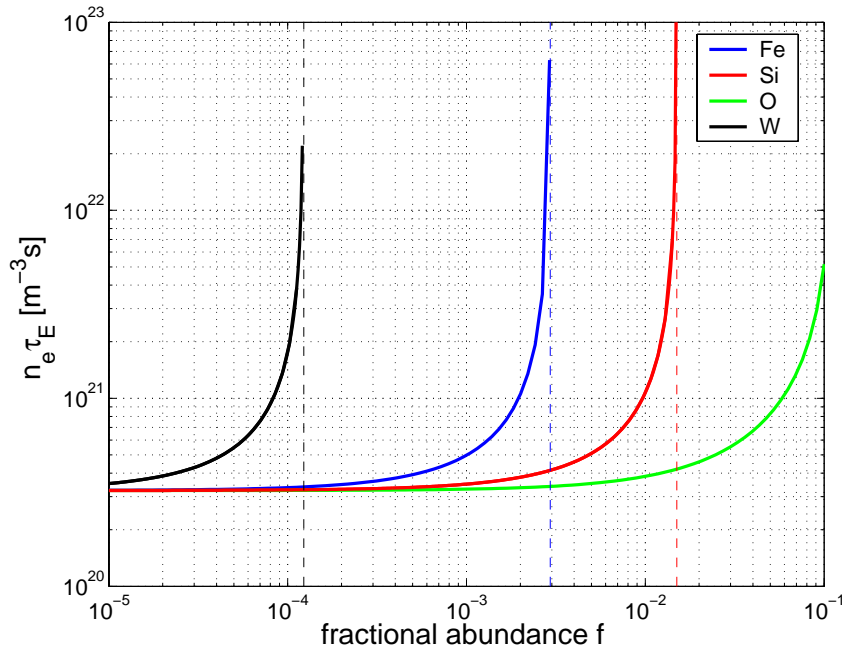
Fig.1.5 - $n_e\tau_E$ requirements in order to sustain ignition in a 50-50% D-T plasma at the temperature (identical for electrons and ions) of 10keV, as a function of the impurity fractional abundance $f=n_{imp}/n_e$. The vertical dashed lines identify the fatal fractions f_{Zc}.

As far as ignition is concerned, the $n_e\tau_E$ requirement in order to sustain this condition in a 50-50% D-T plasma at the temperature of 10keV, following Eq.(1.17), is reported in Fig.(1.5) as a function of the fractional abundance and the species of the impurity. It is evident that minimal concentrations of high-Z elements like tungsten can even prevent ignition, while un-

avoidable low-Z elements can be present up to a few percent of the electron density. The critical fraction f_{Zc}, sometimes called in this case "fatal fraction", has been found[6] to be proportional to $Z^{-2.5}$ for the temperature range $T_e < 20\,\text{keV}$ beyond which a low-β reactor will probably not operate.

In addition of the helium ashes, which constitute an unavoidable impurity in the plasma core, there will be impurity sources from the first wall and the divertor. The cleanliness of a fusion plasma will thus depend on many transport phenomena: the inward flux of fuel and outward flux of helium ashes have to be sufficient to sustain ignition, and the impurity level has to be kept as low as possible. Their concentration f_Z depends on their confinement time and on the recycling rate from the wall, and it can be shown that an excessive value of τ_{imp}/τ_E can prevent ignition in a reactor. The value of τ_{imp} to be considered is the apparent confinement time which takes recycling into account. The condition $\tau_{imp}/\tau_E \sim 10$ is considered an upper limit beyond which no ignition can be reached, even for He poisoning[9, 10].

1.4 Energy confinement and shape dependence in TCV

1.4.1 The TCV tokamak

The Tokamak à Configuration Variable (TCV) has started its operations in November 1992 at the Centre de Recherche en Physique des Plasmas (CRPP) site in Lausanne. It is a compact, medium size tokamak designed to study the effect of different plasma shapes on confinement and stability[11]. The design parameters of TCV are reported in Table 1.2 and a schematic view is shown in Fig.1.6.

TCV is equipped with an axial ohmic transformer for plasma current generation; the toroidal magnetic field is produced by 16 poloidal coils which are connected in series. The unique shaping capabilities of TCV are allowed by two groups of independent coils, which are mounted internally and externally, and driven with an active feedback system. The external group, mounted in vertical stacks and connected to a power supply whose time response is in the order of 1ms, is used for vertical stabilisation as well. The in-vessel coils have a much faster time response (~0.1ms)[11] and are used only to provide stabilisation of highly elongated plasmas ($\kappa > 2$). The vessel is covered almost completely by graphite tiles and the standard bakeout and boronisation procedures allow a vacuum in the range of 10^{-8}mbar during

standard operation. The carbon tiles have been put in place for several reasons, among which there is the reduction of plasma contamination by metallic ions. For a given intrinsic impurity density inside the plasma, carbon has the advantage of lower fuel dilution and radiation emission when compared with moderate or high-Z elements. Moreover, carbon does not melt in case of heat overload, but sublimates at a significant rate at the temperature above ~2500K.

Parameters	Symbol	Value
Major radius	R_0	0.88 m
Minor radius	a	0.25 m
Nominal aspect ratio	$\varepsilon = R_0/a$	≈ 3.5
Vacuum vessel elongation	κ_{TCV}	2.9
Maximum plasma current	I_P	1.2 MA
Maximum central toroidal field	B_0	1.54 T
Maximum loop voltage	V_{loop}	10 V
Discharge duration		< 4 s

Table 1.2: Main parameters of TCV

Parameters	Symbol	Value
Central electron density	n_{e0}	$1 - 20 \times 10^{19}$ m^{-3}
Central electron temperature	T_{e0}	< 1.2 keV (ohmic) ≤ 10 keV (ECH)
Central ion temperature	T_{i0}	< 800 eV (ohmic) < 500 eV (ECH)
Electron cyclotron frequency	$f_{ce} = eB/(2\pi m_e)$	≈ 41 GHz
Elongation at the edge	κ_a	$1 - 2.82$
Triangularity at the edge	δ_a	$(-0.8) - (+0.9)$

Table 1.3: Typical parameters in ohmic and ECH TCV discharges

1.4.2   Plasma shapes and confinement of energy

TCV is capable of producing a large variety of plasmas in both limiter and diverted configurations, among which single (SND) and double null (DND) discharges; ohmic L-modes and H-modes have been produced in diverted and limiter configurations. The geometric parameters span from -0.8 to 0.9 for triangularity, from 1 to 2.82 for elongation, rectangular shapes

and doublets have been produced. The plasma current can be sustained up to 1MA and a value of 210kA has been obtained in purely non-inductive, ECCD driven mode. In Table 1.3 typical values of TCV plasma parameters are reported, while in Fig.1.7 various extreme configurations and shapes are shown.
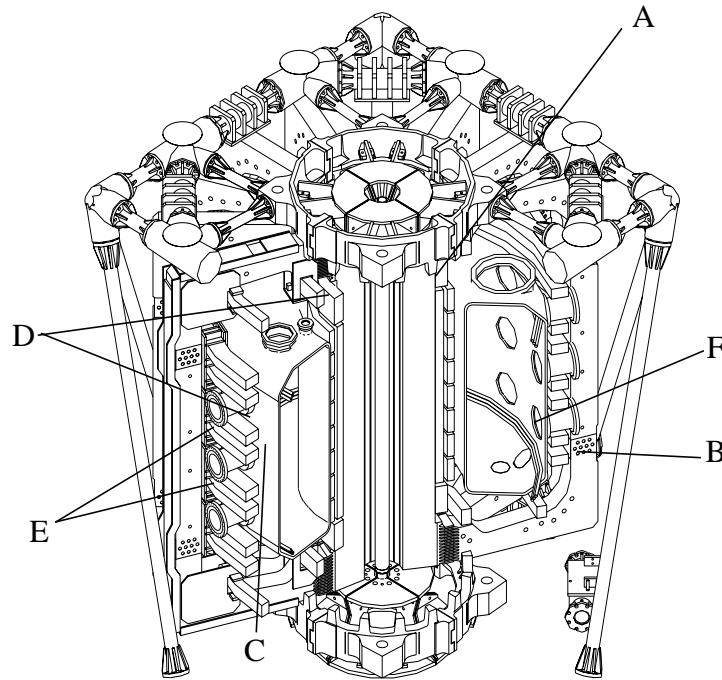
Fig.1.6 - Schematic view of the TCV tokamak: (A) the ohmic transformer coils, (B) the toroidal field coils, (C) the vacuum vessel, (D) the shaping coils, (E) observation ports and (F) internal fast shaping coils.

The main area of investigation which has been extensively studied in TCV plasmas is the dependence of shape on the confinement of energy[12, 13, 14, 15], which, as shown, is directly related to the approach to reactor conditions. The energy confinement time, defined in Eq.(1.10), has been systematically studied as a function of the plasma shape, the electron density and temperature, the safety factor, the ELM activity in ohmic limited and diverted plasmas in stationary conditions.

The extended study of the shape effect on the transport of energy is useful for the study of the impurity confinement as well, as the plasma geometry could have analogous consequenc-

es on electrons, bulk ions and impurities. As it is commonly assumed, impurity confinement times will probably have the same behaviour as energy confinement times.

For a given plasma shape, the ohmic energy confinement time follows[12] the usual neo-Al-

a) #9849 – t=0.50s
Limited (κ=1.2, δ=0.0, Ip=230kA)

b) #6010 – t=0.80s
SND upper (Ip=330kA)

c) #5650 – t=0.80s
SND lower (Ip=335kA)

d) #8856 – t=0.29s
DND (Ip=325kA)

e) #11368 – t=0.65s
Highest current, Ip=1.06MA

f) #18548 – t=1.50s
Highest fully ECCD driven current, Ip=210kA

g) #6442 – t=0.50s
Pear shape (Ip=360kA)

h) #10159 – t=0.01s
Doublet shape (Ip=115kA)

i) #19373 – t=0.42s
Highest elongation, κ=2.80

j) #8890 – t=0.75s
Highest triangularity, δ=0.86

k) #11928 – t=0.67s
Lowest triangularity, δ=−0.77

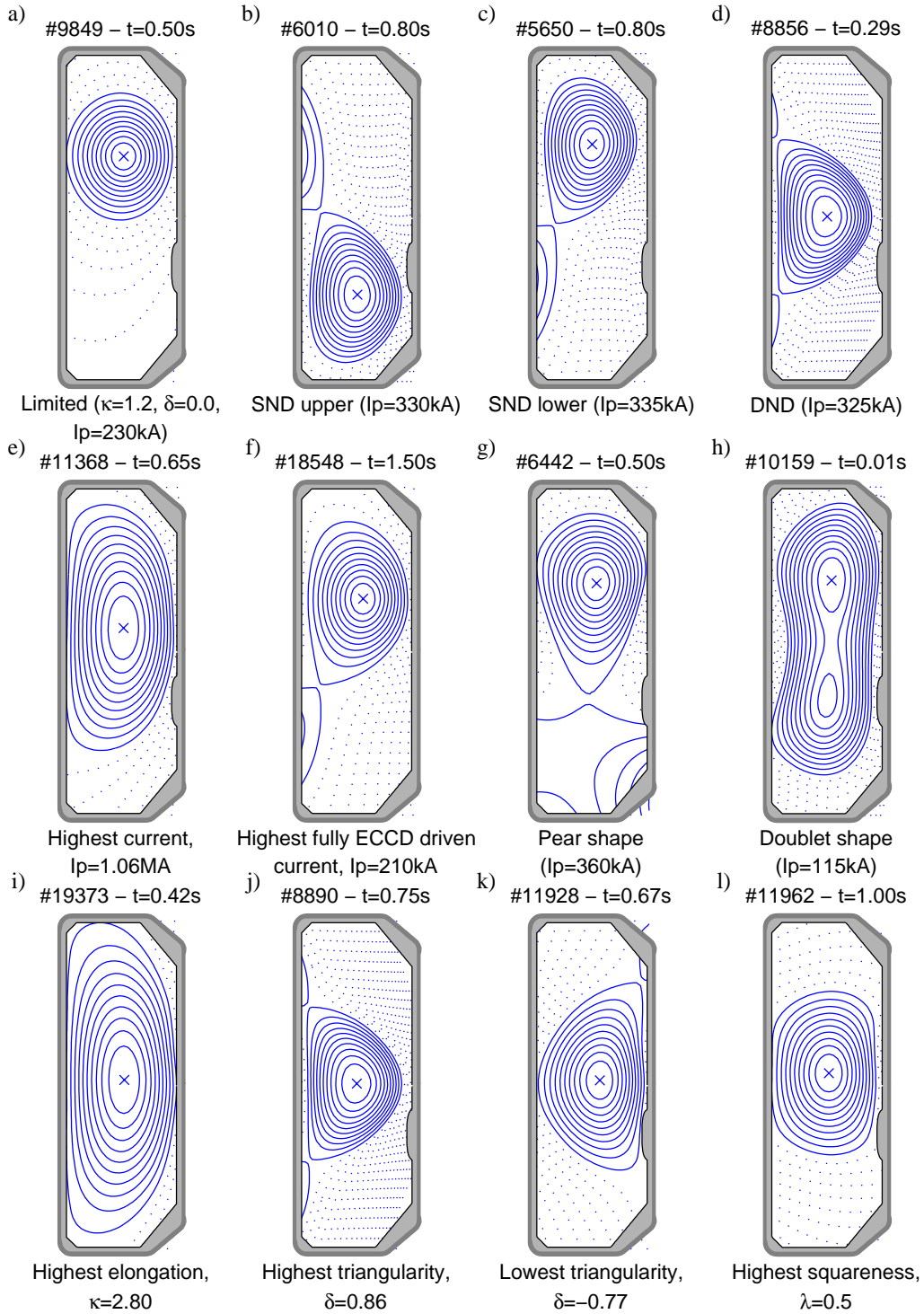l) #11962 – t=1.00s
Highest squareness, λ=0.5

Fig.1.7 - Various plasma configurations and shapes produced in the TCV tokamak.

cator scaling[16]. Scans of plasma current in many different fixed shapes show an increase of τ_E with the edge safety factor q_a, and a linear dependence on the line averaged electron density $\bar{n}_e$ is observed. In all conditions, a strong dependence of τ_E on the plasma shape has been found as, for fixed q_a, an improvement of the confinement with the plasma elongation and a marked decrease with triangularity have been observed.

These variations in the energy confinement time are not found to be related to variations of radiation losses or changes in the sawtooth dynamics, which will be described later in this Section. Rather, the dependence of the global confinement on the plasma shape has been explained solely by the changes in the temperature gradients induced by the geometrical effects of flux expansion and compression, which become important as the plasma shape is far from being circular. Since the correlation between gradients and fluxes is a well established experimental fact[17], the thermal flux must be expected to be affected by the shaping for given temperature profiles. Conventionally the heat flux as power per unit surface is expressed as $q = -n\chi\nabla T$ where χ is the thermal diffusivity. Due to the large diffusivity along the magnetic field lines, the ion and electron temperatures are assumed to be constant on each magnetic surface. The flux geometry can be highlighted by writing:

$$q = -n\chi\frac{dT}{dr}\frac{dr}{d\psi}\nabla\psi \tag{1.19}$$

in which the effects of the plasma shape are described by the gradient geometrical factor $(dr/d\psi)\nabla\psi$. In the case of plasmas with negative triangularity or high elongation, extended zones with high flux expansion arise near the tips, while for positive triangularity the flux surfaces are unfavourably compressed over a wide region at the low field side[12].

To quantify the influence of the geometry alone, the energy confinement time of a shaped plasma is compared to that of a cylindrical plasma with the same horizontal width, thermal diffusivity profile χ and heat flux averaged over magnetic surfaces q_{in}. Assuming that the thermal diffusion coefficient is independent on the poloidal angle and the temperature gradient, the global energy confinement time of the cylindrical plasma can be calculated by integration. A parameter is defined, called shape enhancement factor, as the ratio of the confinement time to that of the reference plasma with same profiles including temperature and density:

$$H_s = \frac{W/P}{W_0/P_0} = \left[S_0\int_0^a\left(\int_r^a\frac{q_{in}}{n\chi}\frac{1}{\langle\nabla\psi\rangle}\frac{d\psi}{dr}dr'\right)ndV\right]\bigg/\left[S\int_0^a\left(\int_r^a\frac{q_{in}}{n\chi}dr'\right)ndV_0\right] \tag{1.20}$$

where W is the total stored energy, P the total heating power, *S* refers to the area of the last close flux surface (LCFS) and the index '0' refers to the equivalent cylindrical plasma. It has to be remarked that the practical evaluation of the shape enhancement factor is based on experimental temperature and density profiles and it is generally obtained for real plasmas. Values of $H_s > 1$ imply an improvement of energy confinement with respect to a circular plasma. The calculated shape enhancement factor is higher for negative triangularities and high elongations, in agreement with the observed behaviour of the energy confinement time. It has been shown[12] that the correction of the electron energy confinement time by the factor H_s explains almost completely the dependence on elongation and triangularity. Following the definition given in Eq.(1.10), the electron energy confinement time is defined as[15]:

$$\frac{3}{2}\frac{\int n_e T_e}{P_{in}} \tag{1.21}$$

where P_{in} is the total heating power.

The phenomenon of power degradation can be accounted for a posteriori by assuming an empirical power law of the form $\tau_E \propto H_s (P_{oh}/S)^{-1/2}$.

The shape enhancement factor can be used in global scaling expressions to describe the effect of geometry. For example, the Neo-Alcator (NA) scaling law as given in Ref.[18]:

$$\tau_{NA} = 0.07 \cdot 10^{-20} \langle n_e \rangle a R_0^2 \cdot \frac{5}{2}\frac{a^2 B_T}{R_0 I_P}[1 + \kappa^2(1 + 2\delta^2 - 1.2\delta^3)] \tag{1.22}$$

which integrates implicitly the power degradation and it is valid for cylindrical plasmas with pure ohmic heating, can be modified with H_s in order to account for the shape effects[14]. In Eq.(1.22), $\langle n_e \rangle$ is the volume averaged electron density. The scaling expression which provides the bestfitting relationship between the experimental total energy confinement time and the plasma parameters is written as[14]:

$$\tau_{NA-TCV} = 0.23 \cdot 10^{-20} H_s \langle n_e \rangle a R_0^2 / \langle j \rangle^* \tag{1.23}$$

where $\langle j \rangle^* = \mu_0 R_0 \langle j \rangle / B_T$ is a non-dimensional current density which replaces the $1/q_a$ dependence in Eq.(1.22).

In addition to the effects of geometry on temperature gradients and therefore on the confinement of the energy, the shape of the plasma is directly linked to MHD phenomena, like sawteeth and edge-localised modes (ELMs), which globally affect the transport of particles.

1.4.3 Sawtooth and ELM activity in tokamaks

The sawtooth crashes in ohmically heated plasmas consist in periodic relaxations of the central electron temperature and density which develop when the central safety factor q_0 drops below unity[19]. A slow rise of temperature and density, determined by heat deposition and transport, is followed by a rapid drop of the central values, during typically $\approx 100\,\mu s$, during which a fast redistribution of the energy takes place inside the so-called mixing radius r_{mix}. The sawtooth crash is triggered by the instability of the internal $m/n=1/1$ kink mode which develops on the $q = 1$ surface. The corresponding outward transport of energy defines the inversion radius r_{inv}, which separates the central region where energy is lost, from
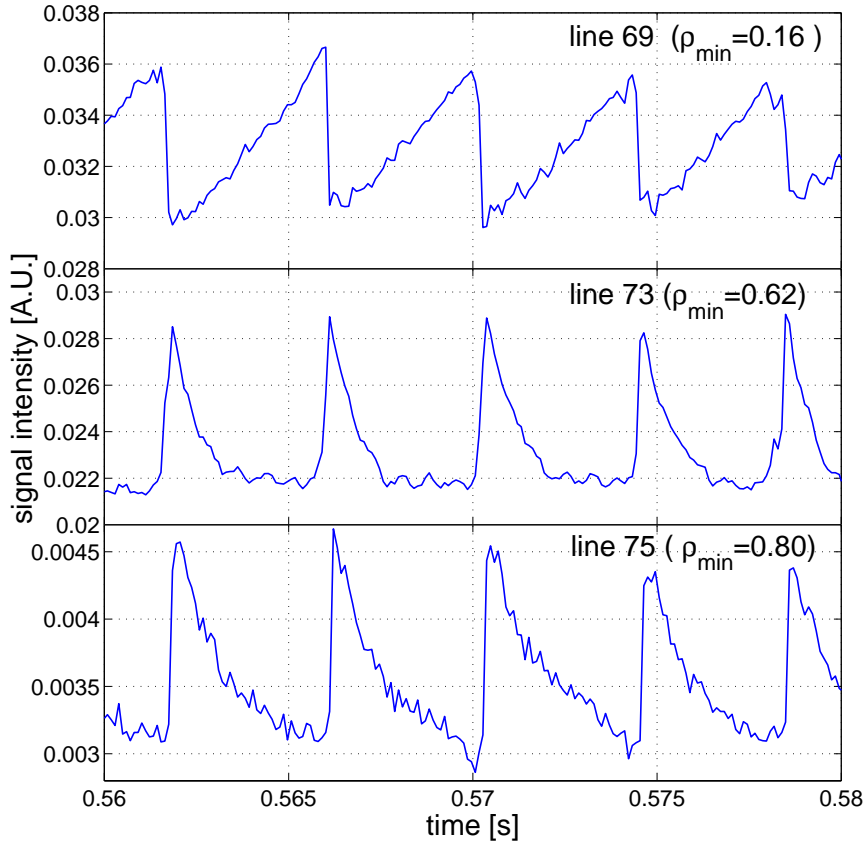
Fig.1.8 - Line integrated soft x-ray signals along different chords, viewing the plasma centre (line 69) and the plasma periphery outside the inversion radius (lines 73 and 75), observed in shot #21022, for which ρ_{inv}=0.48. The temporal signature of the sawtooth crashes is inverted, as a net flow of energy takes place out of the plasma centre. The sawtooth signals are visible also in line 75, which does not intersect the mixing radius at ρ_{mix}=0.68.

an outer region between r_{inv} and r_{mix} where energy is deposited. However, the effects of sawteeth are extended beyond the mixing radius, as the heat pulse which follows the crash provokes an outward transport of energy with $\Delta t \sim \chi_{heat}^{-1}(\Delta r)^2$, where χ_{heat} is the energy

diffusion coefficient. Assuming $\chi_{heat} = 10\,\mathrm{m^2/s}$, the heat pulse can extend its effects of a non negligible fraction of the minor radius, $\Delta r \sim 3\,\mathrm{cm}$, in a time equal to the sawtooth crash time. In Fig.1.8 the line integrated signals of the soft x-ray emissivity are shown. The signal measured on the chords which receive most of their contribution from the plasma centre show the typical fast intensity decrease when the sawtooth crash takes place, while the peripheric chords present the opposite behaviour and even the signals from chords outside the mixing radius contain the typical sawtooth signature. The mixing radius can be hard to define experimentally because the heat pulse can travel a substantial fraction of the minor radius. The definition of the inversion radius is presented in Fig.1.9, on the basis of the profiles of emissivity in the soft x-ray spectral range. Such profiles have been obtained by the tomographic inversion of the line integrated signals, which will be described in detail in Chapter 3. The main contribution to the sudden central decrease is due to the reduction of the electron temperature.

Both the sawtooth period and the crash amplitude are observed to strongly depend on the shape of the plasma poloidal cross section[19]. Small sawteeth with short periods (1.5ms typically) are observed at high elongations or low and negative triangularity, while large sawteeth with long periods (6ms) are observed for low elongations or high triangularity[20]. The sawtooth period is affected by the plasma line averaged density, to which it is roughly proportional[21]. It has to be remarked that at high triangularity the confinement degradation cannot be ascribed to the sawtoothing activity alone.

The rapid transport which accompanies the sawtooth crash can involve a large fraction of the plasma and is supposed to produce the same mixing effects both on electrons and ions, including moderate-Z impurities. In the simplest approximation, the profiles of the densities of electrons, of bulk ion and of any impurity are flattened inside the mixing radius. This phenomenon can lead to a net influx of impurities to the centre in the case of a hollow radial profile which follows short impurity bursts at the plasma edge, or a net outflux if their profile is peaked.

Since sawteeth are correlated with the safety factor, the normalised inversion radius depends mainly on the plasma current profile and on the toroidal magnetic field, and the following approximated relation holds for ohmic plasmas[19, 22]:

$$\rho_{inv} \approx \frac{\langle j \rangle \mu_0 R_0}{B_0 (\kappa_0 + \kappa_0^{-1})} = \frac{\langle j \rangle}{j_0 q_0} \tag{1.24}$$

in which $B_0 \cong B_{0vac}(1 + 0.054(1 - \beta_p)\langle j\rangle*^2)$, with $\langle j\rangle* = \langle j\rangle\mu_0 R_0 / B_{0vac}$ is an accurate approximation of paramagnetic and diamagnetic corrections.

The evaluation of the mixing radius can be done following the magnetic reconnection model of a sawtooth crash which was proposed by Kadomtsev[23]. During the sawtooth crash, the helical flux between the axis and the surface at $q = 1$ reconnects with an equal and opposite flux outside the $q = 1$ surface[4]. The process continues up to the plasma radius for which the helical flux equals that at the magnetic axis. With the following definition of the helical flux[4],

$$\psi(r) \equiv \int_0^r B_{pol}(r')(1 - q(r'))dr' \qquad (1.25)$$

the mixing radius is defined by the condition $\psi(r_{mix}) = 0$.

In a future fusion tokamak reactor the role of sawtooth activity is expected to be important in view of the edge safety factor, $q_a \approx 3$, at which diverted discharges are intended to operate. The repetitive flattening of the central temperature and density profiles would take place over more than a half of the poloidal cross section, and would reduce the fusion yield when compared to peaked profiles. On the other hand, the fast radial transport to which the sawtooth activity is related would improve the refuelling and the He ash removal from the plasma centre, as well as prevent possible central accumulation of moderate-Z impurities.
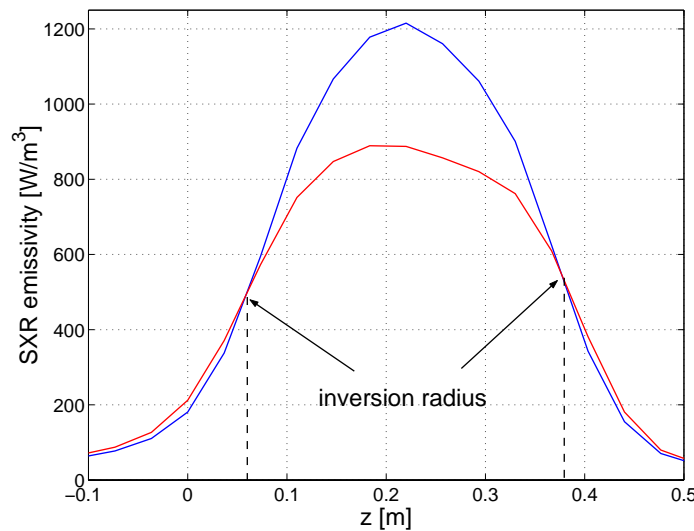
Fig.1.9 - Vertical cut of the soft x-ray emissivity profile along a central chord in shot #21022. The two profiles have been obtained just before and after the sawtooth crash at t=0.57s.

Edge-localised modes, which have been observed in TCV ohmic H-mode plasmas[24], are found to expel a non negligible part of the electron content and energy from the plasma edge, according to the ELM frequency and the size, as well as to the plasma configuration (Single

Null, Double Null D-shape, limiter). In a series of dedicated discharges in which the ELM frequency varied between 50Hz and 300Hz, it has been found[25] that in the DND configurations each ELM event expels 2.2% of the electron content and 2.6% of the stored energy, while for SN plasma configuration the corresponding numbers are 3.4% and 7.2%.

The particle loss at the plasma edge, following an ELM event, has been observed[24] to cause a higher flux of neutral particles from the walls. However, the balance of the measured impurity content in the ELM phase in TCV shows that impurities are more likely to be expelled from the plasma edge, as their rate of change lies between 6% and 10% per event.

The ELM activity brings naturally to a reduction of the particles and energy confinement times τ_p and τ_e, as defined in Ref.[25], according to the expressions:

$$\tau_p = \tau_{up}(1 - \tau_{up}f_{ELM}\langle\Delta N\rangle/N)^{-1} \tag{1.26}$$
$$\tau_e = \tau_{ue}(1 - \tau_{ue}f_{ELM}\langle\Delta W\rangle/W)^{-1}$$

where "u" refers to the phase between consecutive ELM events. The reduction of the energy confinement time is evaluated to be around 18%, depending on the ELM frequency. However, due to the enhanced expulsion of impurities with respect to the energy content, ELMs are a natural way for removal of fusion produced He ashes as well[26].

1.5 Overview of experiments with laser blow-off impurities

Impurity injection by laser blow-off in fusion relevant plasmas is a proven technique which has been widely used in the last three decades[27, 28, 29, 30, 31, 32]. The production of a short beam of neutral atoms or clusters by means of a short-pulsed laser reproduces qualitatively the release of metallic atoms coming from internal structures into the plasma edge during tokamak discharges[33]. The ablation technique allows the injection of solid state non recycling impurities in controlled quantity and timing. The short duration of the puff, typically of the order of 300μs[29], allows the observation of the influx phase alone without the bias of a prolonged source. The use of non recycling elements allows the separate identification of the influx and the depletion phase in the time evolution of the electromagnetic emission by the impurities. VUV and soft x-ray radiation produced by partially stripped moderate-Z ions is usually observed with spectroscopic methods or broadband detectors and the decay time of the central ion brightness is identified with the impurity confinement times and are often used to compare different discharge regimes.

The main components of most of the injection systems are a pulsed laser, a vacuum system and a target which is made of a thin film, deposited on a glass substrate[29], of the material to be injected. The details of the ablation system on TCV are presented in Section 3.1. Apart from the laser blow-off method, small pellets or macroscopic clusters[34, 35, 36] have been injected in plasmas, as well as gaseous impurities by means of short or continuous puffs at the plasma edge[37, 38]. In the following, results on impurity injections from present and past experiments are summarised, with particular attention to non recycling ablated impurities, but observations from trace gas injections are included as well.

In many experiments, particular interest has been given to the evaluation of the transport coefficients in the frame of a diffusive and convective transport of impurities[32, 37, 39, 40], and global confinement times have been obtained for many discharges[41, 42, 43]. However, the global impurity confinement times are machine-dependent, as the effect of the plasma size on their values is very strong. The experimental energy confinement times are commonly compared between devices with different sizes by means of scaling laws which are used for reactor size extrapolation. Nevertheless, data obtained on impurities are still sparse and unsystematic, but providing a similar scaling law for impurities is a goal of fusion research. Comparable values can come from the transport parameters. The bestfitting radial profiles of the transport coefficients have been compared with the values provided by the neoclassical theory[32, 37, 44] (described in Section 2.3).

As a general result, the diffusion coefficient has been found to be much lower in the plasma core rather than at the periphery: for example, typical values obtained in JET L-mode discharges[32, 39] are $D_{in} = 0.1 \div 0.3 \, \text{m}^2/\text{s}$ and $D_{out} = 2 \div 4 \, \text{m}^2/\text{s}$ respectively, with a step profile in the diffusivity, during Ni injections. The convective velocity is directed inward, with a negligible value in the plasma core and of the order of 1.5m/s at the edge. The sawtooth activity is modelled with a sudden increase of the diffusivity inside the inversion radius to values of $D_{in} = 10^2 \div 10^3 \, \text{m}^2/\text{s}$ for the crash duration. In ASDEX Upgrade[37] the transport of Ar has been simulated with an exponential profile for the diffusion coefficient ranging between $D_{in} = 0.02 \, \text{m}^2/\text{s}$ and $D_{out} = 2 \, \text{m}^2/\text{s}$ with no convective velocity. Results from Tore Supra L-mode discharges[40], with injection of Ni, verified the supposed existence of a transition radius separating a low diffusivity region in the plasma core, and a high diffusivity region at the periphery, with the observed values of $D_{in} = 0.2 \, \text{m}^2/\text{s}$ and D_{out} decreasing after each sawtooth crash from 20m^2/s to 1m^2/s; the edge inward velocity decreases as well

from $v_{edge} = 70\,\text{m/s}$ to $v_{edge} = 6\,\text{m/s}$.

The effects of the electron density and the plasma current on the transport parameters have been investigated in the TEXT tokamak[45], following injection of Sc by laser ablation. The transport coefficients D and v are almost not affected by different values of the electron density and of the plasma current. The transport coefficients which were obtained for scandium have been used to calculate the equilibrium profiles of hydrogen, which appeared to be consistent with the experimental observations. Moreover, the diffusion coefficient of scandium is quantitatively very similar to that of the electron energy.

The experimental values for the diffusivity in the plasma core show in some cases a rather good agreement with the neoclassical predictions, especially for low-Z impurities[37, 43, 44]. In other observations, the neoclassical theory cannot account for the high values of the diffusion coefficient both in centre and at the plasma edge. The central values are found to be moderately anomalous with up a factor of 10 in JET[39], and often strongly anomalous at the plasma edge. In JET, the calculated edge values of $D_{out} = 0.06\,\text{m}^2/\text{s}$ and $v_{edge} = 0.4\,\text{m/s}$ fail by far to approach the experimental values reported above.

The Z dependence on the impurity transport has been investigated in ASDEX Upgrade[37], JET[42] and Tore Supra[40]. No correlation to the ion charge was found in Tore Supra, where the span of values of Z was quite limited, the injected impurities being Ni, Ti, Mn. This lack of dependence on the injected elements confirms the results obtained at JET, where Ti, Fe, Mo were used in consecutive shots and the same evolution of soft x-ray radiation was observed. Similar results were found in Alcator-C after laser blow-off injection of Al, Si, Ti, Mo[46]. While the value of the diffusion coefficient is very low in the centre and rises exponentially in ASDEX Upgrade, the transport was found to become strongly convective with increasing Z with inwardly directed convective velocities, leading to very peaked impurity profiles. The pronounced peaking developed during the buildup phase of sawteeth and disappeared during the crashes that produced flat or hollow profiles.

Most of these experiments were performed with the injection of trace quantities of impurities, and the plasma parameters were not affected by the moderately increased power emission during the transient phase of impurity transport in plasmas. However, when perturbative quantities of metallic atoms were injected, effects on the plasma temperature were found. Investigations on JET[47, 48] reveal that the electron temperature in the plasma core following ablation decreases with a time response which is not explained by the value of the electron

thermal conductivity alone; this parameter can however explain the time scales of the following relaxation phase. For larger amounts of injected material the whole plasma periphery is involved in a dramatic electron temperature drop whose propagation speed can be explained only by a non local change of the of the heat transport coefficients. The plasma responds to the edge perturbation by increasing its heat diffusivity practically instantly, even in areas which cannot have been affected directly by the impurity induced edge cooling.

1.6 Aim and outline of the thesis

This thesis is part of a general study on the effects of the plasma geometry on the transport of energy and particles, and addresses the behaviour of impurities.

Impurities determine radiation losses, contribute to fuel dilution and hence play an important role in fusion plasmas. In view of advanced, strongly shaped reactor designs, one important and frequently neglected aspect is the effect of operating modes and plasma geometry on the confinement of fuel particles and impurities, specifically in relation with the energy confinement. In this thesis, the spatial and temporal evolution of the impurity density and their radiation will be studied by means of the laser blow-off technique, which allows the separate observation of the inflow and depletion phases separately. The plasma elongation and triangularity in particular, as well as of magnetic field, current and electron density will be related to the impurity confinement time. The behaviour of this parameter will be compared to that of energy confinement time for the same plasma discharges or for equivalent plasma conditions. The determination of the transport coefficients of impurities in different operational regimes and plasma shapes of TCV, by means of a standard simulation program, will be made.

In this chapter an outline on the possible exploitation of nuclear fusion as a future energy source has been given. The basic concepts on the present scientific and technological status for the actual achievement of a controlled fusion reactor have been presented, together with some considerations on the role of moderate-Z impurities and helium ashes on the energy balance of a reactor machine. The results from TCV on the plasma shape dependence on the energy confinement time have been described, together with a review of other experiments on the injection of non recycling impurities in plasmas. The possibility to extend the research on impurity transport in non conventional plasma shapes, thanks to the unique TCV features,

is presented.

- In Chapter 2 the theoretical background is given on the interactions of impurity ions and plasma. The atomic physics which determines the populations of ion species and the populations of bound electrons in excited states is described, together with the phenomena which lead to the electromagnetic emission due to the ions in plasma. The corona model, which provides a fairly good approximation to the measured populations in low density plasmas, is presented. A well established theory on particle transport in plasma, the neoclassical model, is described. The discrepancies between the theoretical predictions and the transport measurements in many tokamak experiments are referred to as anomalous transport, whose theory is undeveloped especially when dealing with impurities. A general time-dependent model, in which the transport parameters are supposed to be quantitatively determined by comparison of measured and simulated signals, is presented.

- In Chapter 3 the TCV tokamak, the impurity injection system and the diagnostics which are more relevant for the analysis of the impurity behaviour in TCV are described. Details are given of the ruby laser system, the optical apparatus and the ablation target. Among the diagnostic systems, a particular attention is given to the array of 200 soft x-ray photodiodes, which allows the detailed tracking of the impurity concentrations in the plasma core, and the SPRED ultraviolet spectrometer, which has been used to detect light from partially stripped impurities in the plasma edge.
A short description is given on the diagnostics which allow the plasma characterisation, like the magnetic probe array and the Thomson scattering system.

- Chapter 4 starts with the description of the time evolution of the signals which are collected by the soft x-ray photodiodes, and how their shapes are correlated to the transport of impurities in TCV. It is shown that the actual quantities of injected material do not perturb the plasma background in terms of electron density and temperature. The scan of many parameters was performed with the aim of studying the behaviour of the lifetime for different geometrical plasma configurations. Scans of the electron density, plasma current, triangularity, elongation and toroidal magnetic field have been carried out in limiter, ohmic L-mode plasmas.

- Chapter 5 deals with the 1-D simulation code STRAHL, which simulates the soft x-ray emissions from the impurities. The code calculates the time evolution of the x-ray signals for any chosen radial dependence of transport parameters (diffusivity and convective velocity), while the sawteeth radius and frequency, and the plasma parameters are given as input parameters.

  In the first part of the chapter the correlation between the transport parameters and the shape of the simulated signals is presented. Simulations can also be performed for plasmas in which the sawteeth radius or frequency is different from the experimental values, in order to determine their role in the transport of particles.

  In the second part of the chapter the search of the bestfitting transport parameters is done in relation to the actual shapes of the line integrated signals. Many of the signals obtained in the experimental campaign have been reproduced with chosen profiles of the diffusivity and the convective velocity, and these parameters have been correlated to the different plasma conditions. Particular attention has been given to those cases in which the lifetime is strongly affected by the variation of the plasma parameters.

- In Chapter 6 conclusions are drawn and suggestions for future experiments with impurities in TCV are presented.

2. THEORY OF RADIATION AND TRANSPORT IN PLASMAS

Depending on operation conditions, 10-100% of the power delivered to the plasma is lost in the form of radiation. The measurement of this electromagnetic emission by the plasma is of fundamental importance to evaluate many plasma parameters. Relevant examples are the local and global power emissions which are needed to evaluate the energy transport and confinement. A number of diagnostics, which are based on the detection of the plasma radiation, are used to measure the degree of plasma purity, the content of different ionized impurities and their species[49], the particle transport in the plasma.

In order to correlate the radiation emission to the particles in plasmas, it is necessary to know the densities of free electrons, the fractional abundances of the bulk plasma ions and the moderate-Z ions in all the different charges, the populations of bound electrons in all possible states. Depending on conditions, these populations can be in a steady state or can be changing in time.

In current fusion plasma experiments there are particles whose populations can easily reach a steady state equilibrium, like the electrons, the main plasma species, the main impurities coming from the first wall of the vessel and also deliberate impurity gas puffs, like argon or neon. In this case, simple models exist by means of which the various populations can be predicted with good precision. On the contrary, the analysis of transient events like the presence of non recycling heavy impurities requires the calculation of time varying fluxes, ionisation, recombination and radiation emission.

As far as the atomic physics is concerned, two tractable plasma models refer either to very low or very high electron densities, and are called the *corona equilibrium model* (Section 2.1.3) and the *local thermodynamic equilibrium (LTE) model* respectively. However, only the former can find its applicability on plasmas like those produced in TCV, while the latter refers to far higher electron densities[50] and will not be detailed in this Chapter.

In almost all the experimental plasmas the transport of particles across zones where the plasma parameters are not uniform leads to the existence of populations of ions which are not described by either the corona or the LTE equilibria. This is for example the case for short-

lived phenomena like the impurity contamination of the plasma by means of a blow-off injection of moderate-Z non recycling particles.This phenomenon, arising from the radial transport of the impurities in many different ionised stated, requires the use of time dependent models for a quantitative description.

The only mature theory, which provides quantitative predictions for impurity transport is the neoclassical theory (Section 2.3) which provides the calculation of the parallel and radial particle fluxes. The observed difference between the theoretical results and the experimental observations show that the transport has anomalous contributions. However, a theory explaining the excess of particle transport is still undeveloped.

The radial transport of ions and the subsequent transition between different ionised states are often analysed by means of numerical codes, one of which, STRAHL[51], has been extensively used for the interpretation of this work, using empirical transport coefficients.

In the following, the principal processes relevant to the balance in the populations of different ionised states are briefly reviewed.

2.1 State balances

Collisional processes among particles in a plasma have a fundamental role in the determination of the populations of bound electrons in different energy levels[52], and of different ion species following a ionisation or recombination event. In laboratory plasmas such as those produced in TCV, the radiative events, generated by the collisions between ions -or neutrals- and photons are much less frequent than the collisional events between particles, because of the low density of the radiation, and in the following will often be neglected. The events which change the ion charge are the collisional ionisation, which is not accompanied by electromagnetic emission, and the radiative, dielectronic and charge exchange recombinations which normally leave the ion in an excited state and are followed by the emission of one or more photons. The collisional excitation does not change the charge of the involved ion -or neutral atom- but the excited state decays with the emission of a photon.

In what follows, the rate coefficients of each event, taken from Ref.[52], are briefly presented and correlated to the fractional abundances of impurity ions in a plasma.

2.1 State balances

2.1.1 Ionisation state distribution

<u>Collisional ionisation</u>. Most ionisations result from collisions of free electrons with neutral atoms or partially stripped ions, in which the part of the energy of the free electron is used to remove a bound electron. The process can be written

$$A^Z + e \rightarrow A^{Z+1} + 2e. \tag{2.1}$$

A semi-empirical formula for the rate coefficient (number of events per unit density and time) of a given bound state i can be found in Ref.[52]:

$$\langle \sigma_i v \rangle = 1.7 \cdot 10^{-14} \bar{g} \left(\frac{R_y}{\chi_i}\right) \left(\frac{T_e}{R_y}\right)^{1/2} \exp\left(-\frac{\chi_i}{T_e}\right) \left[1 - \exp\left(-\frac{5\chi_i}{T_e}\right)\right] \; [\text{m}^3/\text{s}] \tag{2.2}$$

where $\bar{g} = 1 + (\sqrt{3}/\pi) \ln|1 + T_e/\chi_i|$ is the Maxwellian-averaged Gaunt factor, χ_i is the ionisation potential of the state considered and R_y the Rydberg constant. The total rate coefficient is the sum on all contributing electrons in the ion, but usually only the uppermost levels of the ion have to be considered.

<u>Radiative and dielectronic recombination</u>. Radiative recombinations is the capture by an ion A^{Z+1} of charge $Z + 1$ of a free electron into an excited bound state. This process is accompanied by the emission of a photon and can be described as:

$$A^{Z+1} + e \rightarrow A^Z + h\nu \tag{2.3}$$

The rate coefficient for a radiative recombination to the bound state n in the ion i is usually calculated using the Kramer's formula[52]:

$$\langle \sigma_{in} v \rangle = 5.2 \cdot 10^{-20} \bar{g} Z \left(\frac{\chi_{in}}{T_e}\right)^{3/2} \exp\left(\frac{\chi_{in}}{T_e}\right) Ei\left(\frac{\chi_{in}}{T_e}\right) \; [\text{m}^3/\text{s}] \tag{2.4}$$

This rate coefficient has to be multiplied by the fraction of free holes in partially filled electron shells in the ion. In Eq.(2.4) the Gaunt factor $\bar{g}$ can be taken equal to 1 and

$$Ei(y) = \int_y^\infty \frac{\exp(-s)}{s} ds. \tag{2.5}$$

For high-Z ions the dielectronic recombination can play an important role in the charge state balance and contribute significantly to the power radiated by impurities in the plasma. This phenomenon occurs when a free electron is captured into a highly excited state and the released energy is used by a inner bound electron to move to a higher bound state. The final

result of such a process is an ion in double excited, very unstable state which normally decays radiatively:

$$A^{Z+1} + e \rightarrow A^{Z^{\circ\circ}} \rightarrow A^{Z^{\circ}} + hv \rightarrow A^Z + hv' \tag{2.6}$$
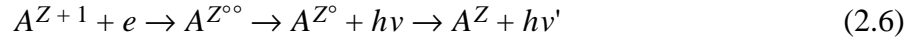
but which can also lead to an autoionisation process in which the captured electron is expelled again.

A widely used expression for the rate coefficient is based on empirical fits to a variety of theoretical calculations:

$$\langle \sigma_{ij} v \rangle = 8.8 \cdot 10^{-18} f_{ij} Z^{2/3} \left(\frac{R_y}{T_e} \right)^{3/2} \frac{E_{ij}}{R_y} \exp\left(-\frac{E_{ij}}{T_e} \right) [\text{m}^3/\text{s}] \tag{2.7}$$

where f_{ij} is the dimensionless oscillator strength[52], whose magnitude is in the order of unity.

Charge exchange recombination. A further process which takes place in a population of partially stripped ions in plasmas is charge exchange, in which an electron, during a collision, is transferred to an ion normally from a neutral atom. This reaction is most likely to happen when an impurity collides with a neutral hydrogen (or D, T) atom:

$$A^{Z+1} + H^0 \rightarrow A^{Z^{\circ}} + H^1 + hv \rightarrow A^{Z-1} + H^1 + hv' \tag{2.8}$$
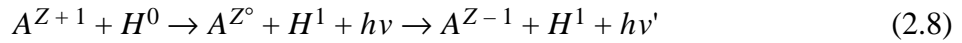
The details on the rate coefficient $\langle \sigma v \rangle_{CX}$ of this process can be found in Ref.[53].

In hot plasma experiments, the total rate of charge exchange recombination events, which is
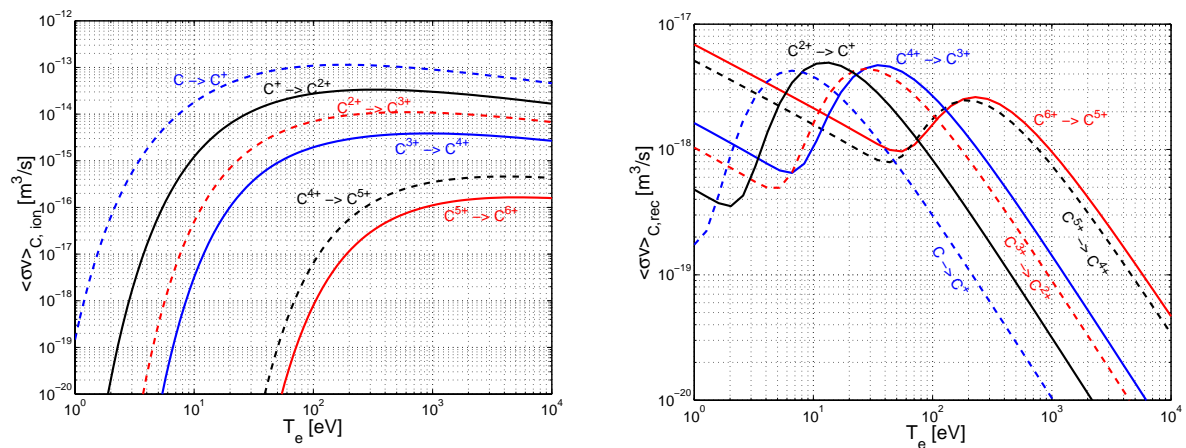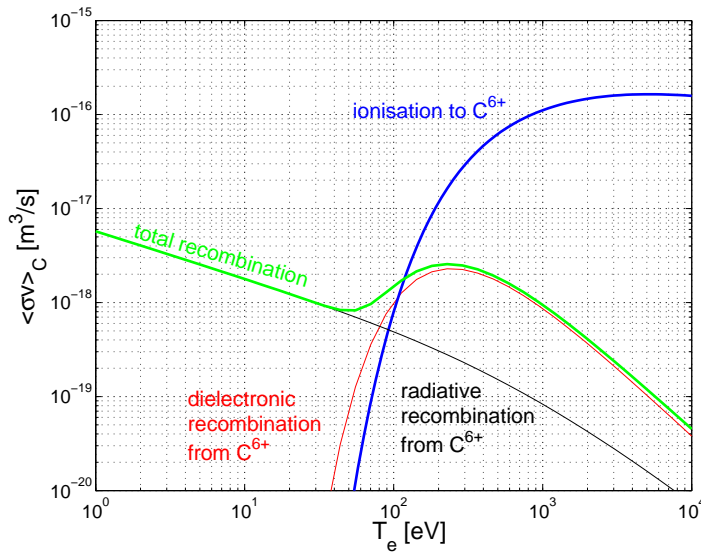

Fig.2.1 - (a) The collisional ionisation rate coefficients for carbon ions versus the electron temperature. (b) The collisional recombination rate coefficients for carbon ions versus the electron temperature.

2.1 State balances

equal to $n_0 n_Z \langle \sigma v \rangle_{CX}$ where n_0 is the density of neutrals, is far smaller if compared to the competitive recombination processes as the number of neutrals is much less that the number of electrons. Normally the charge exchange effect becomes significant only when neutral beams are injected in the plasma.

As an example concerning typical TCV plasmas, the collisional rate coefficients for carbon are shown in Fig.2.1. In the plasma centre of TCV the electron density can be assumed to be around $5 \cdot 10^{19} \, \text{m}^{-3}$, thus the typical characteristic time for the slowest ionisation, from C^{5+} to C^{6+}, is about 10^{-4}s, which is much less the time scales of most of the transport processes (except sawtooth crashes). As shown in Fig.2.2, for an electron temperature higher than ~120eV, the ionisation rate exceeds recombination and consequently fully stripped carbon is the dominant form over most of the plasma cross section.

On the other hand, even in the peripheral part of the plasma, where the electron temperature

Fig.2.2 - The collisional ionisation and radiative rate coefficients for the transition between C^{5+} and C^{6+} versus the electron temperature.

is of the order of 1eV, the total collisional recombination rate for the process C^{6+} to C^{5+} is never higher than a few 10^{-18}m^3/s. In this case the characteristic recombination time is about 10ms or more, considering that the electron density can be lower than the central value. As this time is of the same order of the transport times across the minor radius of the plasma, highly ionised impurities may be found even at the plasma last closed flux surface where the electron temperature would be too low to produce them by ionisation.

2.1.2 Excited states distribution

In a plasma in which the interactions with photons are negligible because of a low radiation density, the populations of bound electrons in excited states are produced by two processes which result to an excited bound electron. Recombination described in the previous Section normally lead to an excited state in the ion or neutral after the electron capture, and the rate coefficients relative to the particular final excited states, of the form given in Eqs.(2.4, 2.7) can be found in Ref.[52].

In plasmas, most populations of excited electrons in bound states derive from collisions between ions in ground state and free electrons which are not captured in the reaction. The rate coefficient can be obtained by means of the perturbation theory in quantum mechanics for the levels of the electrons in the ion, and reads:

$$\langle \sigma_{ij} v \rangle = 3.15 \cdot 10^{-13} f_{ij} \left(\frac{R_y}{T_e} \right)^{1/2} \frac{R_y}{E_{ij}} \exp\left(-\frac{E_{ij}}{T_e} \right) \bar{g} \ \ [\mathrm{m^3/s}] \tag{2.9}$$

where f_{ij} is the dimensionless oscillator strength. The Gaunt factor $\bar{g}$ can be chosen equal to the one for bremsstrahlung, which will presented in Section 2.2.1.

The populations of electrons in excited states are then influenced by the decay to a lower state, whose process is accompanied by the emission of a photon. The decay can be spontaneous or triggered by a collision with a photon or a free electron. While the collisional rate for the decay is dependent on the electron or photon density, the timescale of the radiative spontaneous decay is determined by atomic physics considerations alone and it is quantified by the Einstein coefficients A_{ij}. A given Einstein coefficient A_{ij} defines the probability per unit time of a spontaneous transition from a state i to a state j, and the expression

$$\tau_i = \left[\sum_{j<i} A_{ij} \right]^{-1} \tag{2.10}$$

defines the radiative lifetime of the state i.

A rough approximation[52] for the Einstein coefficients is given by

$$A_{ij} \approx 10^{-8} Z^4 \tag{2.11}$$

and consequently the spontaneous relaxation times from excited levels are very short compared to the typical transport and ionisation/recombination times. Exceptions exist in which metastable states are formed and the scaling law given in Eq.(2.11) is no longer valid; an example is given in Section 2.1.3 and is presented as a limit of the corona model.

2.1 State balances

The collisional processes can be neglected as soon as the electron and radiation densities are low enough. This is one of the assumptions for the validity of the corona model, which is described in the following Section.

2.1.3 Corona model

In the early 1950s, the corona model was proposed to explain some observed features in the spectrum of the solar corona and it has also been applied in the description of low density laboratory plasmas. The fundamental approximation of this model is that all the upward transitions are collisional (since the radiation density is low) and all the downward transitions are radiative. The plasma has to be optically thin, thus all photons simply escape the plasma without being reabsorbed, and the downward transitions are spontaneous and independent of electron density.

Each excited state has a population arising from the equilibrium between the collisional excitation and the spontaneous radiative decay, without transport of ions from regions with different temperature. In the case of excitation from the ground state to the level i, the following balance holds:

$$\frac{n_i}{n_0} = (n_e \langle \sigma v \rangle_{o \to i}) / \left(\sum_{j < i} A_{ij} \right) \tag{2.12}$$

where the summation involves all the Einstein coefficients for the decay from the state i to all the states j.

A similar balance occurs between different ion species, in which it is assumed that the ionisation and recombination rate coefficients do not depend on the excitation states of the ions:

$$\frac{n_Z}{n_{Z+1}} = \frac{\langle \sigma v \rangle_{Z+1 \to Z}}{\langle \sigma v \rangle_{Z \to Z+1}} \tag{2.13}$$

in which $\langle \sigma v \rangle_{Z \to Z+1}$ is the collisional ionisation rate coefficient and $\langle \sigma v \rangle_{Z+1 \to Z}$ the radiative recombination rate coefficient. Eq.(2.13) shows that the ratios of ion species of a given element are independent of the electron density and only depend on the electron temperature.

In Fig.2.3 the distribution of carbon ion species in plasmas is shown as a function of the electron temperature. The assumption of corona equilibrium is made, thus the representation is very general and device-independent, when the requirements for the model to be valid are satisfied.

Some features of such distributions are correlated to atomic physics properties of the energy levels. For example, the broad temperature range in which the C^{4+} ion exists is due to the relative stability of the helium-like ion. This stability can be observed in Fig.2.1, which shows that the ionisation rate coefficient for the C^{4+} to the C^{5+} ionisation is much lower than the rates for the previous steps.
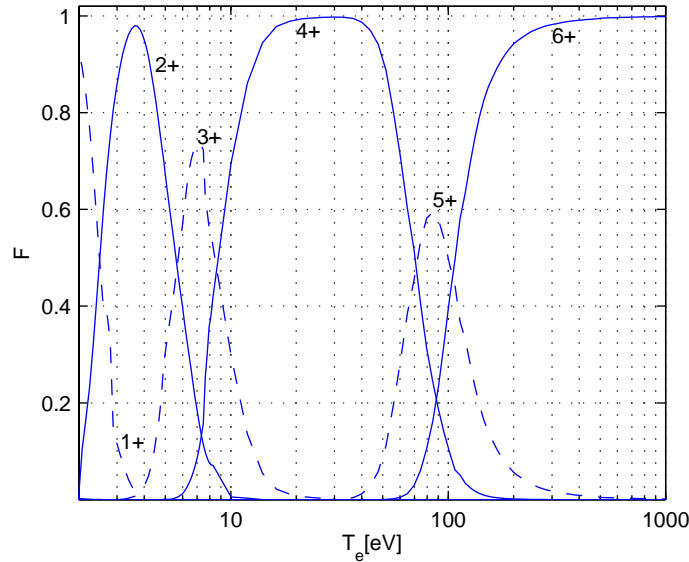

Fig.2.3 - Fractional abundances of different ionisation states of carbon in corona equilibrium as a function of the electron temperature.

Fig.2.4 shows the ion distribution in the case of Si, for which again some particularly stable configurations become dominant, like the Ne-like state at the plasma periphery and the He-like state which dominates in plasma centre. In the core of Ohmic TCV plasmas (at 700-1200eV) this state coexists with H-like and fully stripped silicon. Only for temperatures above 5keV, which are obtained in TCV plasmas with auxiliary heating, almost all the silicon ions are fully stripped.

A simple way to approximate the highest ionised stage which is reached by impurities in a plasma can be given by means of the following formula[52]:

$$Z \approx \sqrt{5 T_e / R_y}. \tag{2.14}$$

The corona model can be applied as long as radiative de-excitation dominates over collisional processes. As far as the electron density is concerned, the limit is reached at the point where collisions of the ions with free electrons induce the transition of the excited electrons

2.1 State balances

to a neighbouring excited level at non negligible rate[50]. In this way the radiative decay of the excited level is reduced. A criterion for the use of the corona model can be obtained by assuming that for a given electron density there are as many radiative decays as collisional transitions out of a level, thus resulting in a line intensity which deviates of 50% from the corona model value. This criterion can be written as:

$$n_e \langle \sigma v \rangle_{pq} < \sum_{s<p} A_{ps} \tag{2.15}$$

where $\langle \sigma v \rangle_{pq}$ is the collisional rate coefficient for the transition from the excited state p to q and A_{ps} the Einstein coefficients for the radiative decay to a state s.
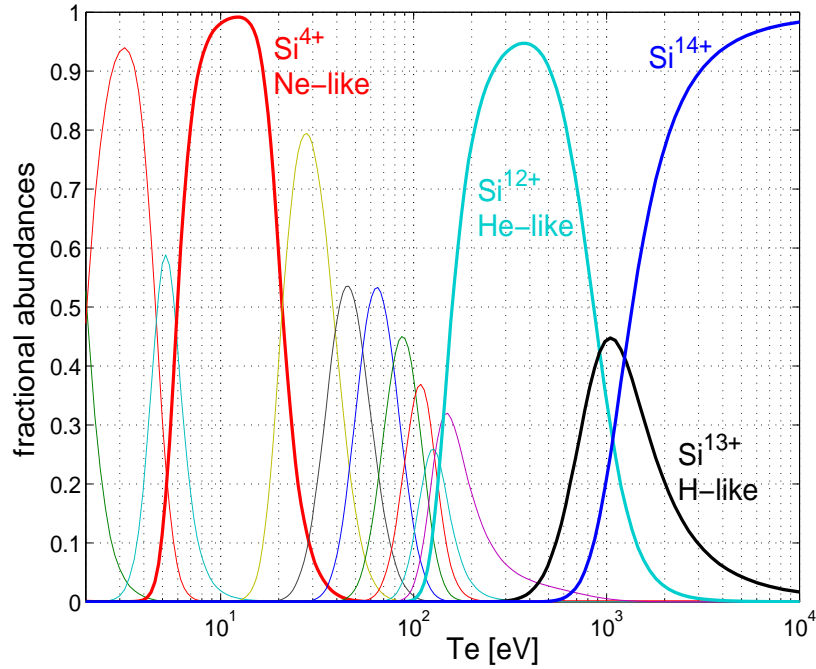
Fig.2.4 - Fractional abundances of different ionized states of silicon as a function of electron temperature in corona model.

Ideally the density limit should be set in order to respect Eq.(2.15) for all the states p. However, a detailed inspection of the values of the various coefficients indicates that there is always some level for which the criterion is not satisfied, as for higher principal quantum numbers the probability of a spontaneous decay is decreased with respect to that of a collisional decay. As an example, the limit density for a hydrogenic ion of charge Z, and a value $p = 6$ can be evaluated to give[50]:

$$n_{e,crit} \approx 6.5 \cdot 10^{16} (Z+1)^6 \sqrt{T_e} e^{0.1(Z+1)/T_e} \ [\mathrm{m^{-3}}] \tag{2.16}$$

33

and in the case of carbon in a plasma with $T_e = 100\,\text{eV}$, the found limit density is $n_{e,\,crit} \approx 3 \cdot 10^{22}\,\text{m}^{-3}$ which is 2-3 orders of magnitude larger than the common electron densities in fusion plasmas. Such considerations however do not take into account the possible existence of metastable states where collisional decays may be significant compared to radiative decays, like for example the 2s2p ^{3}P state of the C^{2+} ion.

In conclusion, the corona model can be a useful tool to give an estimate of the ionised species of moderate-Z impurities in TCV, as the predictions are general, machine independent and the plasma temperature is the only sensitive parameter as soon as the model hypothesis are valid. However, the radial transport of impurities may play an important role on the fractional abundances of impurity ions, especially in view of the fairly low recombination rate. As a consequence, the ion densities and the radiation distribution need to be described with a more general model which takes transport into account.

2.2 Radiation from plasmas

In Section 2.1 the description was given of the theory which gives a quantitative evaluation of the transition rates of the different ionised and excited states for ions in a plasma, which participate in the balance of the various states. Most of the transitions which have been described are accompanied by the emission of electromagnetic radiation, which contributes to the total emitted power with a continuum spectrum or discrete spectral lines. These processes are the most relevant and will be detailed in the following:

- Bremsstrahlung radiation arises from electron-ion collisions, which normally consist of small angle deviations of electrons as a result of Coulomb scattering in the electric field of the ions. The bremsstrahlung radiation results from a free-free interaction, as the initial and final states of the electrons are not bound, and its spectrum is consequently a continuum.

- Recombination radiation produces a continuum spectrum as the initial state of the involved electron is free. The final state is bound and usually excited as result of the capture of the electron by an ion and usually a radiative decay follows the capture.

- Line radiation originates from the transition of a bound electron from an excited state of an ion to another state of lower energy. A photon of energy $E = h\nu = E_{ini} - E_{fin}$ is

emitted and the overall spectrum, in the ions rest frame, is discrete.

- Cyclotron radiation arises from the gyromotion of charged particles around the magnetic field lines. Electrons, due to their low mass and consequently high cyclotron frequency $\omega = eB/m_e$, provide the most of the radiation, while the contribution from main and impurity ions is negligible. In the case of typical fusion experiments, in which $B = 1 \div 10\,\text{T}$, the radiation is mainly emitted in the microwave spectral range. An estimate of the emitted power density is given in Ref.[54] in the assumption of an optically thick plasma for the spectral range of interest. For typical TCV plasmas the emitted cyclotron radiation power is in the order of 1W and can be neglected in comparison of other loss mechanisms.

2.2.1 Bremsstrahlung

In fusion plasmas the main contribution to bremsstrahlung radiation comes from electron-ion interactions. The contribution from electron-electron Coulomb collisions is generally negligible for non-relativistic energies as the invariance in the motion of the centre of charge does not produce dipole emission.

The radiation per unit volume of the plasma can be obtained by integration of the power emitted by each event of electron-ion scattering, integrated on the velocity distribution and the collision parameter. In the case of a Maxwellian isotropic distribution, and in the classical approximation, the power per unit frequency is given by[52]:

$$j(\nu) = \bar{g} n_e n_Z Z^2 \left(\frac{e^2}{4\pi\varepsilon_0}\right)^3 \frac{16\pi}{3\sqrt{3}m^2c^3}\left(\frac{2m}{\pi T_e}\right)^{1/2}\exp\left(-\frac{h\nu}{T_e}\right) \tag{2.17}$$

where $\bar{g}$ is the Maxwellian-averaged Gaunt factor. Corrections due to quantum mechanics as well as relativistic effects are generally taken into account inside the Gaunt factor. This factor, in the classical limit, is plotted in Fig.2.5 as a function of $h\nu/T_e$ for different approximations, which are correlated to the typical scattering angle of an electron in a plasma. For $T_e \ll Z^2 R_y$ and low frequency, the following Kramers approximation is valid:

$$\bar{g} = \frac{\sqrt{3}}{\pi}\ln\left|3.24 \cdot 10^{-5} T_e[keV]^{3/2} h\nu[keV]Z^{-1}\right| \tag{2.18}$$

For $T_e \gg Z^2 R_y$ the Born approximation can be used:

$$\bar{g} = \frac{\sqrt{3}}{\pi}K_0\left(\frac{h\nu}{2T_e}\right)\exp\left(\frac{h\nu}{2T_e}\right) \tag{2.19}$$

where K_0 is the modified Henkel function of order 0.

It has to be remarked that the Gaunt factor lies between 0.3 and 2 for a wide range of temperatures which can be found in typical fusion plasmas experiments. Therefore, almost all the temperature and radiation frequency dependence of the emitted power is found in the $T_e^{-1/2}\exp(-h\nu/T_e)$ term, and consequently the average photon energy is approximately equal to the electron temperature. For plasmas of interest in thermonuclear fusion the bremsstrahlung emission is mainly in the x-ray spectral range.
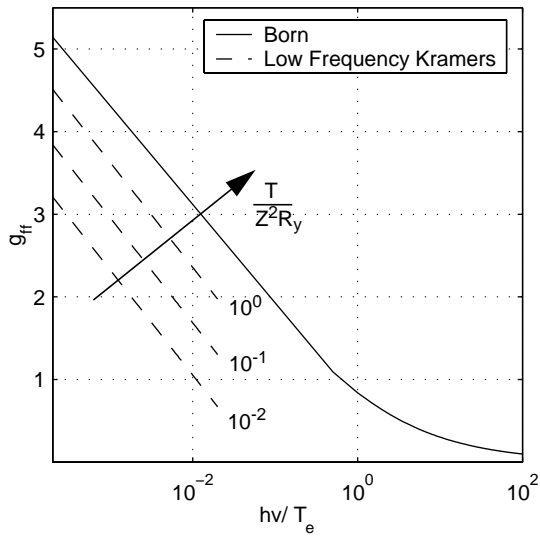

Fig.2.5 - Maxwellian-averaged Gaunt factor as calculated from Kramers and Born analytical approximations given respectively in Eq.(2.18) and Eq.(2.19).

Let apart a small effect on the Gaunt factor (Fig.2.5), the effect of high-Z ions in a typical hydrogen plasma is evident from Eq.(2.17). The emitted power by bremsstrahlung grows with a Z^2 law and a small quantity of heavy impurities can easily lead to an important loss of energy from the plasma core where impurities can concentrate and be fully stripped.

When bremsstrahlung dominates, however, provided the Gaunt factor to be the same for all species, the emission is proportional to:

$$\sum_i n_e n_i Z_i^2 = n_e^2 Z_{eff} \tag{2.20}$$

in which the definition of Z_{eff} is included. Using the quasi-neutrality condition $n_e = \sum n_i Z_i$, Z_{eff} can be equivalently be expressed as:

$$Z_{eff} = \sum n_i Z_i^2 / \sum n_i Z_i. \tag{2.21}$$

Z_{eff} is a measure of the impurity contamination of fusion plasmas. It is usually derived from measurements in the visible and near infrared, where recombination radiation is negligible.

2.2.2 Recombination radiation

In the frame of free electron collisions with ions a major role in the determination of the emitted radiation is taken by the recombination process in which the final state of the electron is bound. The final spectrum of recombination is continuous and reflects the kinetic energy distribution of the electrons of the plasma, as each electron contributes with its kinetic energy to the spectral distribution of the emitted power. The subsequent decay of the captured electron in an excited state causes the emission of a photon, according to the processes described in Section 2.2.3.

As far as the continuum contribution is concerned, it has to be observed that any given atomic level contributes to the spectrum only with photons of energy

$$h\nu = \frac{1}{2}mv^2 + R_y\frac{Z^2}{n^2} \tag{2.22}$$

To obtain the total recombination continuum radiation from the plasma, the recombination rates given in Eqs.(2.4, 2.7) have to be taken into account. The power contribution from free electrons of energy $[E, E + dE]$ recombining to the level i is given by:

$$\frac{dn_e}{dE}n_i\langle\sigma v\rangle_i(E - E_i)dE \tag{2.23}$$

where dn_e/dE is the energy distribution of the free electrons, which can normally be Maxwellian. The total recombination power is obtained by integration of Eq.(2.23) on the whole energy spectrum of the electrons and summing on all free states of the ions. The explicit expressions can be found in Ref.[52].

2.2.3 Line radiation

Depending on plasma conditions, a large contribution to the total emitted power may come from transitions of bound electrons between different energy levels of neutral or partially ionized impurities. The radiation is produced in the form of narrow spectral lines without a continuum background, as single photons are emitted at the energy corresponding to the difference of energies of the initial and final state of the ion, $h\nu = E_i - E_f$.

Provided the plasma is optically thin, the power density relative to the spectral line arising from this transition is given by[52]:

$$I_{pq} = n_{Z,p}A_{Z,pq}(h\nu_{pq}) \tag{2.24}$$

where $A_{Z,pq}$ is the Einstein coefficient giving the probability of transition from the state p to q in ion Z per unit time and $n_{Z,p}$ is the density of ions with charge Z which have an electron in the excited state p. In order to determine the total line radiation loss from the plasma, it is necessary to know the abundance of each population of ions with given excited states. For tokamak plasma conditions, each abundance $n_{Z,p}$ has to be determined from the collisional excitation and the recombination rate coefficient. A simplified evaluation can be derived for example by assuming the validity of the corona equilibrium model, as described in Section 2.1.3. In this frame, from Eq.(2.12) the population of electrons in the level p of the ion Z is determined:

$$n_{Z,p} = n_e n_{Z,g} \langle \sigma v \rangle_{Z,gp} \sum_{q < p} A_{Z,pq} \tag{2.25}$$

in which $\langle \sigma v \rangle_{Z,gp}$ is the collisional excitation coefficient from the ground level of the ion Z to the excited state p. The total power emitted can thus be expressed as:

$$I_{pq} = n_e n_{Z,g} \langle \sigma v \rangle_{Z,gp} \left(A_{Z,pq} \bigg/ \sum_{q < p} A_{Z,pq} \right) (h\nu_{pq}) \tag{2.26}$$

which only requires the knowledge of the ground state population $n_{Z,g}$ of each ionic species.

2.2.4 Energy integrated spectral emissivity

For practical purposes, the calculation of the total emitted local power of an ion population in a plasma can be expressed as function of temperature, without distinguishing the kind of electromagnetic emission. The total plasma emissivity is obtained by summing the contributions of all ion species, including the main plasma ion, and is given by the following expression:

$$E(r) = \sum_Z \varepsilon_Z(r) n_e(r) n_Z(r) \tag{2.27}$$

which has the advantage to correlate the emissivity to local parameters only and to include all the contributions in the energy integrated spectral emissivity, shortly called radiation parameter $\varepsilon_Z(r)$. This parameter, which corresponds to the power emitted by a species per unit electron and its own density, depends on the excited and ionised populations for each element, thus it is affected by the electron temperature and the transport.

Assuming a transport free coronal equilibrium, it is possible to evaluate this parameter in a general configuration and machine independent situation, as it depends only on the electron

temperature. Moreover it can take into account filtering and the sensitivity of detectors, without loss of generality. As an example, the corona radiation parameter $\varepsilon(r)$ is shown in Fig.2.6 for silicon and carbon. It can be remarked that the highest values of the emissivity
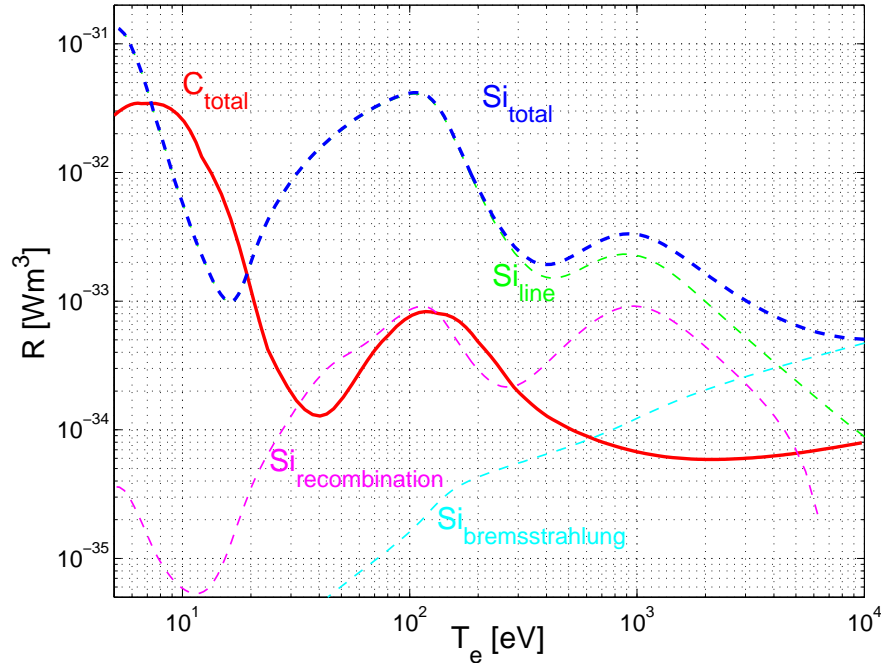

Fig.2.6 - The total radiation parameters for silicon and carbon as obtained by STRAHL database. For silicon the partial radiation parameters are shown. R corresponds to the emission by an ion in corona equilibrium with plasma, given per unit electron and impurity density.

are found at low temperature. Impurities, depending on their concentration and on the electron density, can dominate the power balance in the low temperature regions of the plasma. For silicon, the partial contributions to the total radiation parameter are shown in Fig.2.6. At low electron temperature, recombination and bremsstrahlung are negligible, while they become more important above 100eV. For higher temperatures beyond 5keV, only the bremsstrahlung contribution is important for silicon, since there are no more bound electrons to contribute to the line radiation, and the recombination rate is dramatically reduced. In this case, the total emitted bremsstrahlung power from different elements follows the Z^2 dependence, as shown in Eq.(2.17).

2.3 Particle transport models

In the basic corona model, bulk transport of different ion species in the plasma is not taken into account. In many situations the populations are not in corona equilibrium, as the characteristic times of transport are in the same order of magnitude as the times needed to reach the equilibrium. Moreover, any steady state model cannot take into account transient phenomena which are common during perturbations in the plasma density, temperature or composition.

The problem of the quantitative evaluation of the transport properties in a plasma is of fundamental importance as they affect the confinement time of any species, including bulk ions and electrons. Over the decades, models accounting for the radial transport of particles, due to various local microscopic or global plasma properties, have been proposed[55, 56, 57]. The classical theory takes into account Coulomb collisions between charged particles which affect the Larmor orbits, whereas the so-called neoclassical transport is caused by collisions affecting the guiding centre orbits created by the magnetic field of the toroidal confinement system. This theory, while being used as a comparison reference for most of the experimental data, cannot explain the observed radial transport occurring in tokamaks, which in the majority of conditions is significantly larger than the one which can be ascribed only to collisional effects. The amount of transport which cannot be explained by the neoclassical theory is called anomalous.

In the following Section the classical approach to the collision-driven transport in plasmas is presented. The theory of neoclassical transport, which makes quantitative predictions of the radial fluxes of particles in a typical toroidal plasma for experimental fusion, is described in Section 2.3.2. The general time dependent evolution of transient phenomena of transport of impurity ions in a plasma will be presented in Section 2.3.4.

2.3.1   Classical approach of particle transport

The basic property of both the classical and the neoclassical transport theories is the concept of Coulomb collision frequency between the considered test particle and the surrounding species. Depending on the particles involved, a deviation of the trajectory takes place whose intensity depends on the charges, masses and the impact parameter. However, in case of heavy ions, the assumption can be safely made that collisions with electrons do not affect the ion trajectories. Without entering in the details of Coulomb scattering, it can be found[58,

2.3 Particle transport models

59] that the collision frequency of a species 'a' with a species 'b' can be expressed, for equal temperatures, as:

$$\nu_{ab} = \frac{4\sqrt{2\pi}e^4}{3}\frac{1}{m_a}\sqrt{\frac{m_a m_b}{m_a + m_b}}\frac{Z_a^2 Z_b^2 \ln\Lambda}{(kT)^{3/2}}n_b \tag{2.28}$$

in which $\ln\Lambda$ is the Coulomb logarithm. The total collision frequency of the species 'a' is the sum $\nu_a = \sum_b \nu_{ab}$ referring to all the 'b' ion species present in the plasma.

The test particle of the species 'a' can be assumed to follow a random walk driven by independent scattering events (Brownian random process)[58], and the diffusion coefficient can be thus calculated:

$$D = \frac{\langle(\Delta r)^2\rangle}{2}\nu_a \tag{2.29}$$

where Δr is the radial displacement of the test particle for collisions taking place at time intervals τ_i. The expression in Eq.(2.29) is valid for a wide class of problems relating to the random walk diffusion. In the case of motion through a magnetic field, the relation holds:

$$\langle(\Delta r)^2\rangle = 2\rho_L^2 \tag{2.30}$$

ρ_L being the Larmor radius. From Eqs.(2.29, 2.30), the classical diffusion coefficient $D_{CL} = \rho_L^2 \nu_a$ is obtained.

2.3.2 Neoclassical transport

A step beyond in the analysis of the transport of particles in toroidal geometry is based on the fact that, in a collisionless plasma, the guiding centres of electrons and ions tend to follow orbits which imply a natural radial displacement along their natural motion. These can be passing orbits, which involve full toroidal turns or the so-called banana orbits[4], the latter being most important for transport. In real plasmas, the effects of Coulomb collisions superpose to the radial motion and make particles move to different orbits. The collision frequency is a parameter upon which different transport regimes are identified. The different regimes arise from the possibility for trapped particles to complete a bounce orbit before being deviated to a different orbit by a collisional event.

The condition for which the bounce frequency is lower than the frequency of events (one or more collisions) for which a particle deviates its trajectory enough to be detrapped can be expressed as:

41

$$\nu_a{}^* \; = \; \frac{\nu_a q R}{\varepsilon^{3/2} v_{th}} < 1 \tag{2.31}$$

In Eq.(2.31), which contains the definition of the collisionality ν^*, q is the safety factor and $\varepsilon = a/R$ is the inverse plasma aspect ratio. While this inequality typically holds for electrons and main ions in low density, high temperature plasmas for which the collision frequency is low enough, the Z_a^2 dependence of the collision frequency reported in Eq.(2.28) does not allow moderate-Z ions to perform complete banana orbits without collisions.

As far as collisionality in TCV plasmas is concerned, an expression can be obtained by replacing Eq.(2.28) in Eq.(2.31) and substituting the TCV parameters ($R = 0.9$ m, $\varepsilon = 1/3.5$ at the plasma edge, less in the centre). The numerical coefficients have been calculated for silicon in a deuterium plasma containing carbon as an intrinsic impurity:

$$\nu_{Si}{}^* \; = \; 1.03 \cdot 10^{-16} \frac{Z_{Si}^2 q}{T^2} n_D \left(1 + 2.74 Z_{Si}^2 \frac{n_{Si}}{n_D} + 2.30 Z_C^2 \frac{n_C}{n_D} \right) \tag{2.32}$$

where the densities (in m^{-3}), the temperature (in eV) and the safety factor q vary along the minor radius of the plasma.

It can be remarked that a concentration of fully ionised carbon of 1.5%, which is found in clean TCV plasmas, provides a contribution to the overall collisionality equal to that of deuterium alone. The strong effect given by Z_{Si}^2 is balanced by the usually low concentration of injected silicon in the plasma, however in case of H-like silicon with $n_{Si}/n_D = 2 \cdot 10^{-4}$ the contribution to $\nu_{Si}{}^*$ is 10% of that of deuterium.

The collisionality has been calculated for many of the discharges in which silicon has been injected by means of laser ablation. The profile of $\nu_{Si}{}^*$ is always increasing towards the plasma edge because of the dominance of the increase of the q/T^2 factor over the decrease of n_D. In the centre the minimum value of $\nu_{Si}{}^* \sim 0.6$ was found for high temperature, low density plasmas ($T_{e0} \approx 1150$ eV, $n_{e0} \approx 2.5 \cdot 10^{19}$ m^{-3}) with about 2% of carbon, while at the opposite end of the TCV operating domain ($T_{e0} \approx 600$ eV, $n_{e0} \approx 9 \cdot 10^{19}$ m^{-3}) the central collisionality was $\nu_{Si}{}^* \sim 9$.

Depending on the collisionality ν^* of a given species, the transport can be in different regimes. At low collisionality, for which $\nu^* < \varepsilon^{3/2}$ (0.15 in TCV), the bounce frequency of the trapped particles is higher than the detrapping collision frequency and the trajectory of most particles of the species follow a trajectory determined by the toroidal geometry. The radial extent of the orbits is larger than the Larmor radius and consequently the diffusion coeffi-

2.3 Particle transport models

cient is larger than the classical one. In this regime, called banana regime after the shape of the collisionless trapped orbits, the diffusion coefficient can be approximated with[4]:

$$D \sim \frac{q^2}{\varepsilon^{3/2}} \nu \rho^2 \qquad (2.33)$$

which has been obtained in analogy of Eq.(2.29), using the width of the banana orbit and the fact that only a fraction $\sim \varepsilon^{1/2}$ of all particles is trapped. This coefficient exceeds the classical value by the large factor $q^2/\varepsilon^{3/2}$ which is of the order of 10 in the centre of TCV plasmas and up to 50 at the plasma edge. However, as shown above, the collisionality of the silicon impurities in TCV makes them very unlikely to be in this regime.

At high collisionality almost all particles are scattered before an orbit is completed. The lower limit of collisionality for this regime, called Pfirsch-Schlüter regime[57, 60], is found when the trapping of particles in the low field side becomes negligible[4] and it is given by $\nu^* > 1$. The particle fluxes can be obtained by means of fluid equations which are justified by the high collisionality, where the hoop force arising from the plasma pressure is taken into account.

The solution of the fluid equations leads to the fact that the radial fluxes of particles show two components, the diffusive term $D(r)$ depending on the impurity density gradient, and a velocity term $v(r)$ which locally implies the convective radial motion of particles. Without entering in the details of the calculations, the magnetic surface averaged radial flux of particles can be written as:

$$\langle \Gamma_r \rangle = \frac{dn}{dr} D_{CL} \left(1 + 2 \frac{\eta_{\parallel}}{\eta_{\perp}} q^2 \right) - n \left(\frac{E_{\varphi} B_{\vartheta}}{B_{\varphi 0}^2} \right) \qquad (2.34)$$

in which η is the electrical conductivity of the plasma (in parallel and perpendicular directions), E_{φ} the toroidal electric field corresponding to the loop voltage, D_{CL} the classical diffusivity given by Eqs.(2.29, 2.30). The term which multiplies the density gradient is the Pfirsch-Schlüter diffusion coefficient. A second contribution to the radial flux is given by the term proportional to the particle density, whose coefficient has the dimension of a velocity. This contribution, called Ware pinch[61], predicts an inward flux of particles originated by the interaction between the parallel electric field with the trapped particles.

For collisionality values given by $\varepsilon^{3/2} < \nu^* < 1$, the diffusion is said to be in the plateau regime, as the diffusion coefficient is independent on collisionality and its value is given by

$$D \sim \frac{v_{th} q}{R} \rho^2 \qquad (2.35)$$

43

which matches the Pfirsch-Schlüter coefficient for $\nu^* = 1$.

It has been shown that the collisionality of moderate-Z impurities is strongly dependent on plasma conditions. The calculated values for silicon in TCV show that ν^* spans over part of the plateau regime and can be well inside the Pfirsch-Schlüter regime for plasma regions with lower temperature.

Generally speaking, heavy impurities tend to lie in this regime because of their lower thermal velocity and higher charge compared to the plasma ions. The steady state solution of the fluid equations for the radial distribution of impurities gives[62] $n_Z(r) \propto [n_H(r)]^Z$ which would imply a strongly peaked impurity concentration in the plasma core, with dangerous implications for the confinement of the energy and fuel dilution. However, more realistic calculations of the neoclassical fluxes for ignited plasmas[63] show that the mean convective velocities are positive, i.e. always outwardly directed and may cause an effective screening for the high-Z elements. The neoclassical diffusion coefficients are typically found to be in the range of 10^{-2} m^2/s in the plasma centre for low-Z and moderate-Z impurities, which can be a problem for helium ash removal. If the positive convective velocities in ignited plasmas is measured in a future experimental ignited plasma, central accumulation of helium ashes and impurities would be prevented.

The calculated and measured diffusion coefficients for low-Z and high-Z impurities have been compared for many experimental data on a number of machines[37, 39, 40, 64]. While for lighter elements the agreement has been reported to be fairly good, strong deviations have been observed for heavier elements, whose transport can be an order of magnitude larger.

In TCV, the neoclassical coefficients D_0, D_{edge} and v_{edge} have been calculated for many shots in which silicon and aluminum have been injected as non recycling impurities. Their values have been compared to the experimental transport coefficients, and the results will be shown in Chapter 5. In particular, the comparison is needed to determine if the transport of the injected impurities in TCV has an anomalous component, and to which extent.

2.3.3 Anomalous transport

As stated above, in many experiments the observed radial transport occurring in tokamaks turns out to be significantly larger than the one which can be ascribed to collisional effects alone. The additional contribution to the neoclassical transport parameters is referred to as anomalous transport.

2.3 Particle transport models

Up to date, the development of a theory which accounts for the increased transport of particles in a tokamak plasma is in progress as far as electrons and main ions are concerned[65-70]. A theory which describes the behaviour of impurities in plasmas is still largely undeveloped. Some mechanisms which are taken into account for the formulation of a theory of the anomalous transport of electrons may prove to be valid also for impurities. Examples are plasma instabilities which can drive turbulence and MHD fluctuations in plasmas[71], or electrostatic fluctuations in or near the scrape-off layer. It has been reported[71] that the ratio of the electron and ion diffusivities χ_e / D_i at the plasma edge may be strongly dependent on the instability modes and consequently there may be no direct correlation with other plasma parameters.

A recent study on TCV[72] correlates the observed electron anomalous pinch to predictions of models based on the Ware pinch, the anomalous thermodiffusion and the curvature pinch. While the first is proportional to the loop voltage and it is predicted by the neoclassical theory, the others are consequences of the temperature gradient and the gradient of the safety factor respectively. The curvature pinch seems to provide a good description on the electron profile peaking if a turbulent transport is assumed, in which trapped and passing particles give the same contribution to overall transport.

2.3.4 General time dependent evolution

The neoclassical theory offers the possibility to describe the flux of impurities as the sum of two contributions, a diffusive part characterised by a coefficient D_Z and a convective part characterised by a convective velocity $\vec{v}_Z$, both of which depend on the local plasma parameters as well as on the charge of the ions. The convective velocity lumps together all contributions which are not proportional to the impurity density gradient, such as the gradients of T_e, $T_{i \neq Z}$, $n_{i \neq Z}$. The same mathematical form applies to the anomalous transport.

In order to take into account the anomalous transport in an empirical manner, the basic idea is to retain the same description in terms of radial profiles of diffusivity and convective velocity, without correlating their values to physical parameters like electron temperature and density, collisionality and magnetic fields. The profiles of the coefficients D_Z and $\vec{v}_Z$ are supposed to be quantitatively determined by comparison of simulated and measured signals from real plasmas.

For each ionised species an equation stating the conservation of the number of particles has

to be written, while it is not necessary to consider transients in the equilibrium between excited states, as the distribution of populations follow a much faster dynamics.

The equation for a single ion species is written as:

$$\frac{dn_Z}{dt} = -\nabla \cdot \vec{\Gamma}_Z + (n_{Z-1}S_{Z-1 \to Z} + n_{Z+1}S_{Z+1 \to Z}) - n_Z(S_{Z \to Z-1} + S_{Z \to Z+1}) \quad (2.36)$$

which states that the variation in the density of an ion species equals the net influx from the surrounding plasma plus the variations due to ionisation and recombinations to and from the neighbour states.

In analogy with the neoclassical formulation, the particle flux density is assumed to be of the form:

$$\vec{\Gamma}_Z = -D_Z \nabla n_Z + \vec{v}_Z n_Z. \quad (2.37)$$

All the values of density, transport coefficients and atomic physics coefficients depend on the position in the plasma. Eq.(2.36) is a system of equations in the number of $Z+1$, being Z the total charge of the element in consideration. The solution is in general obtained numerically by simulation codes, in which the external source of neutrals, the electron density and temperature are provided as external known parameters.

Once the set of Eqs.(2.36) has been solved, the populations of bound electrons in excited states can be evaluated with the corona -or any other- model and the impurity emission evaluated. On TCV, the above set of equations is solved by means of the STRAHL[51] code (presented in more detail in Chapter 5), which then calculates the total and SXR radiation from each ionised state of impurities.

### 2.3.5 Role of transport on impurity distribution in TCV

As it was discussed in Section 2.1.1, the distribution of populations of different ionised states is strongly affected by the rather long recombination time. A rough evaluation showed it to be of the order of tens of milliseconds, thus being comparable to the characteristic times of particle transport in TCV. This fact leads to a distribution of ionised states which is not in equilibrium with the electron temperature as it would be determined according to the corona model. A calculation performed with STRAHL using the measured electron temperature and density profiles (from shot #21164) is shown in Fig.2.7, where the different distributions are compared in the case of corona equilibrium and in a case where an Ansatz on the diffusivity

and convective velocity profiles has been done. These resulting calculated profiles include the effect of sawteeth, which are supposed for simplicity to flatten the distribution of each ion species inside the mixing radius.

The typical effect of transport can be described as a broadening of the peaks for each ionised species along the minor radius. This effect is more visible in the edge part of the plasma, where the temperature gradients are high and the radial spread of each species is very limited. Moreover, neoclassical and anomalous transport are stronger in the plasma edge and contribute more evidently to the peak broadening of low-Z ions concentrations.

These differences in the fractional abundances of the various ionised states of silicon may lead to discrepancies between the radiation parameters in the corona model and a general configuration in which transport is taken into account. In Fig.2.9 the radiation parameter is shown as a function of the normalised radius for shot #21164. The profile of $\varepsilon(r)$ in corona equilibrium has been calculated from the data in the STRAHL database, and depends only
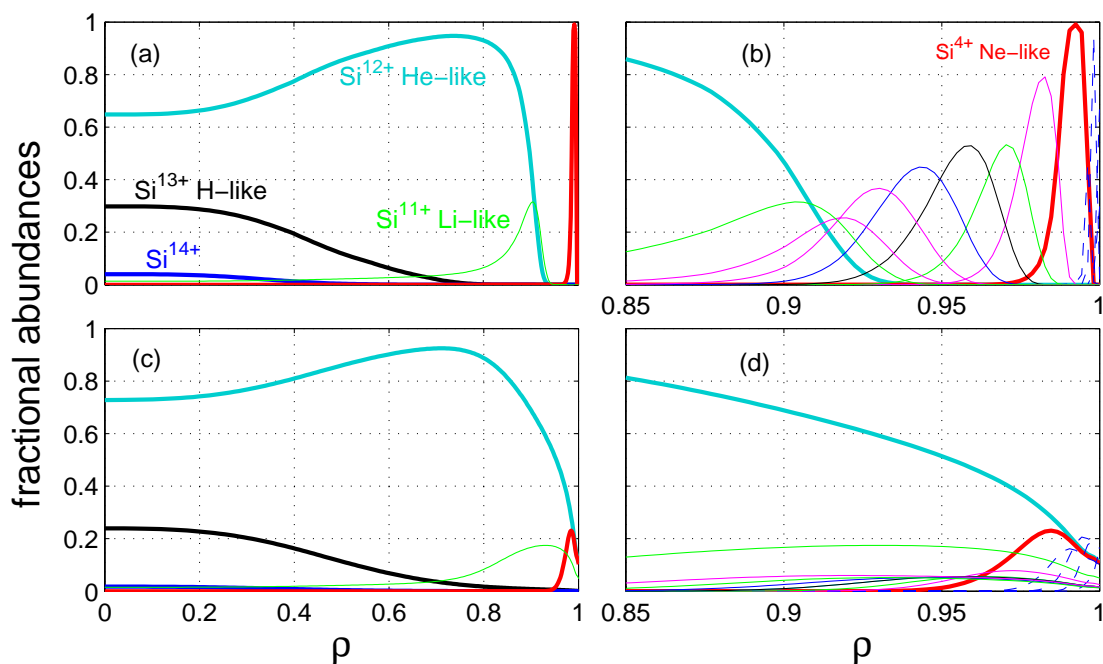
Fig.2.7 - Ionisation equilibria for silicon with experimental electron density and temperature from shot #21164. In (a) and (b) corona equilibrium is assumed, while in (c) and (d) the transport parameters were chosen to be $D = 0.05 + 0.35\rho_{pol}^2 \, m^2/s$ and $v = 4.5\rho_{pol} \, m/s$ outward. In this case the peaks of each ionised species are broader, lower and displaced towards the centre. The electron density and temperature profiles are shown in Fig.2.8. The profiles with transport have been evaluated during the depletion phase when all signals are decreasing exponentially, about 30ms after the end of the source.

on the electron temperature profile. The transport corrected $\varepsilon(r)$ have been obtained by means of a STRAHL simulation, using the bestfitting parameters which are found for the reproduction of the line integrated SXR signals (for details see Chapters 4 and 5). Following the simulation, which calculates the local emission of each ionised state separately, the corrected radiation parameter can be calculated using the definition of Eq.(2.27):

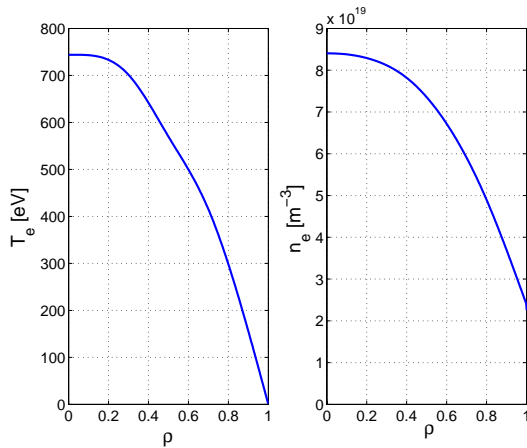$$\varepsilon(r) \cong \frac{E(r)}{n_e(r) n_Z(r)} . \tag{2.38}$$

Fig.2.8 - The electron density and temperature profiles of shot #21164.

In the example of Fig.2.9, the spectral sensitivity of the actual SXR photodiodes is included. The local SXR emissivity $E(r)$, the local total impurity density $n_Z(r)$ are the simulated values and all the radiation parameters shown take into account the photodiodes filtering.

A marked difference appears in the comparison of the corona and the source phase radiation parameters, while in the depletion phase $\varepsilon(r)$ is larger of a few percent only in the plasma centre. However, the generalisation of such behaviour to different plasma configurations can be only qualitative, as the transport corrected radiation parameter can depend significantly on the transport coefficients.
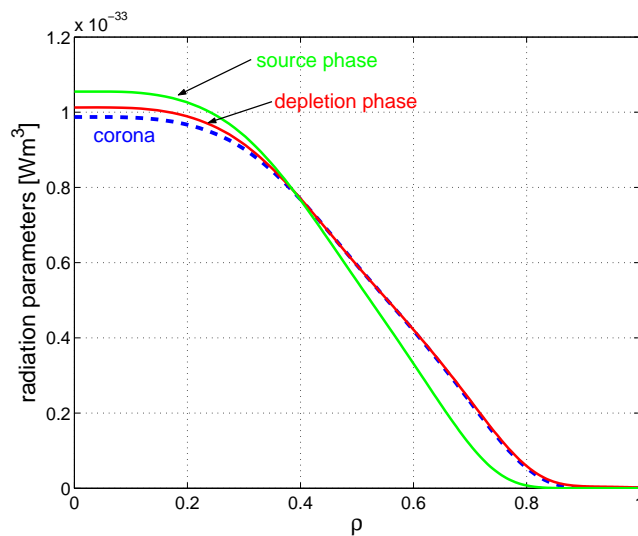

Fig.2.9 - The radiation parameter $\varepsilon(r)$ as a function of the normalised radius for shot #21164, where transport is taken into account and in corona equilibrium. The transport parameters are those reported in the caption of Fig.2.7. The transport corrected $\varepsilon(r)$ has been calculated with STRAHL at t=2ms (green) and t=30ms (red) after the beginning of the source phase.

2.4 Conclusion

In this Chapter, the theoretical determination of the impurity populations in plasmas, as well as the mechanisms of their electromagnetic emission have been described. With reference to typical TCV ohmic plasmas, moderate-Z impurities like silicon are found to be stripped to the He-like and H-like states (Fig.2.4) in the plasma core, where the electron temperature is of the order of several hundreds of eV. The electromagnetic emissions, which are composed mainly by line and recombination radiation, lie in the soft x-ray part of the spectrum in the plasma core, while VUV lines are emitted by partially stripped impurity ions in the plasma periphery.

According to these remarks, injected impurities in TCV plasmas will be observed with the array of SXR photodiodes, whose features will be described in Chapter 3. VUV lines from the peripheric parts are recorded by means of the SPRED spectrometer calibrated on the main lines of partially stripped ions, to complement the observations of the SXR photodiodes which are insensitive to the low temperature parts of plasmas.

A simulation code like STRAHL is required to calculate the simultaneous phenomena of radial transport of impurities and the ionisation processes which depend on plasma conditions. The electromagnetic emissions are evaluated with Eq.(2.27) and the line integrated signal compared to the experimental results in order to determine the bestfitting set of transport parameters.

3. INJECTION AND DIAGNOSTICS OF TRACE IMPURITIES IN TCV

The theory of electromagnetic emission from impurities in a plasma, presented in Chapter 2, shows that the radiation of moderate-Z impurities lies in the VUV and soft x-ray spectral range when the electron temperature in the plasma core is of the order of 1keV, which is typical of ohmically heated TCV plasmas. The laser blow-off injection of elements like Al or Si is well suited for the investigation of transient impurity transport in TCV. Various reasons lead to this choice of materials: their radiation matches the available diagnostics and, as non recycling impurities, they provide the direct measure of the impurity confinement time in the plasma. Moreover they were acceptable by the TCV community after some initial concern about impurities sticking on the carbon tiles which cover most of the vessel walls.

Silicon and aluminum are ionised to the He-like and H-like states in the plasma core, and their line radiation is detected by the soft x-ray photodiodes system. The spatial and temporal resolution of its detectors allows the precise localisation of the radiation source, but there is the inconvenience that all ionic species contribute to the detected signal. However, this method is advantageous as the impurity contribution is obtained by subtraction of the background. The detection of partially ionised species from the plasma edge, where the electron temperature is of the order of hundreds of eV, is performed with a spectrometer calibrated on selected lines in the VUV spectral range.

This chapter provides the description of the hardware systems which were used for this work. The blow-off of impurities has been performed with a ruby laser apparatus, which is described in the following, together with the optical system for the laser beam delivery to the ablation target. Section 3.3 provides a presentation of a number of diagnostics, which supplied the most relevant data for the analysis of impurity transport in TCV plasmas. These include basic plasma diagnostics, like the Thomson scattering system and the FIR interferometer for the determination of the electron temperature and density profiles, the magnetic probe system for the reconstruction of the plasma equilibrium and the determination of the geometry of flux surfaces and specific diagnostics for impurity monitoring, like the soft x-ray photodiode array, the spectrometers SPRED for VUV and the OMA for visible light from neutrals.

3.1 The ablation laser apparatus

The ruby laser used for the impurity injection experiment by laser blow-off is a device[73] which was commercially available (Apollo Laser, model 35) when first used for Thomson scattering on TCA in 1981. It is a two stage laser, consisting of a combined oscillator-amplifier unit emitting at the wavelength of λ=694.3nm. The very long charging time, of about 30s, allows no more than one single injection for each TCV discharge. The typical output in Q-switched operation is a pulse of the duration of about 20ns[73] with a maximum energy of 5J/shot, with the beam vertically polarised. Table 3.1 summarizes the current setup for standard operation in the experiment.

Before it was taken into service again in 1997, many parts of the laser system have been heavily refurbished in order to provide a more reliable operation and to ease possible modifications in the structure and locations. Inside the cavities, new flashlamps are fed via thicker electrical rods in order to improve the electrical conductivity. The area around the flashlamp-rod connection has been surrounded with a teflon protection to minimize the risk of an electric arc to the cavity main body. The coaxial wires leading to the flashlamps from the power supply have been fitted with fast connectors, allowing an easy separation of the different components.

The laser apparatus, including the power supply and the cooling water recirculator, have been placed in the TCV restricted area at level -1, in front of sector 3, as it is schematically shown in Fig.3.1. All components have been placed on wheeled chariots for easily moving the system in case a wide access to the torus at sector 3 is needed.

| Parameters	Value
Main flashlamp voltage	10.0kV
Amplification stage flashlamp voltage	10.0kV
Q-switch voltage	3.0kV
Q-switch timing after flashlamp trigger	600μs

Table 3.1: Current parameters of the electrical configuration of the ruby laser.

3.1.1 Accessories

The water recirculator (model LabPlus CFT75/PD2) provides a cooling water flow of about 5l/min., which is constantly checked by means of a flow rate threshold gauge. The pump

3.1 The ablation laser apparatus

works in a low pressure configuration, which was obtained by putting the two cavities in parallel. The actual flow and operating pressure can be regulated by means of a manual bypass.
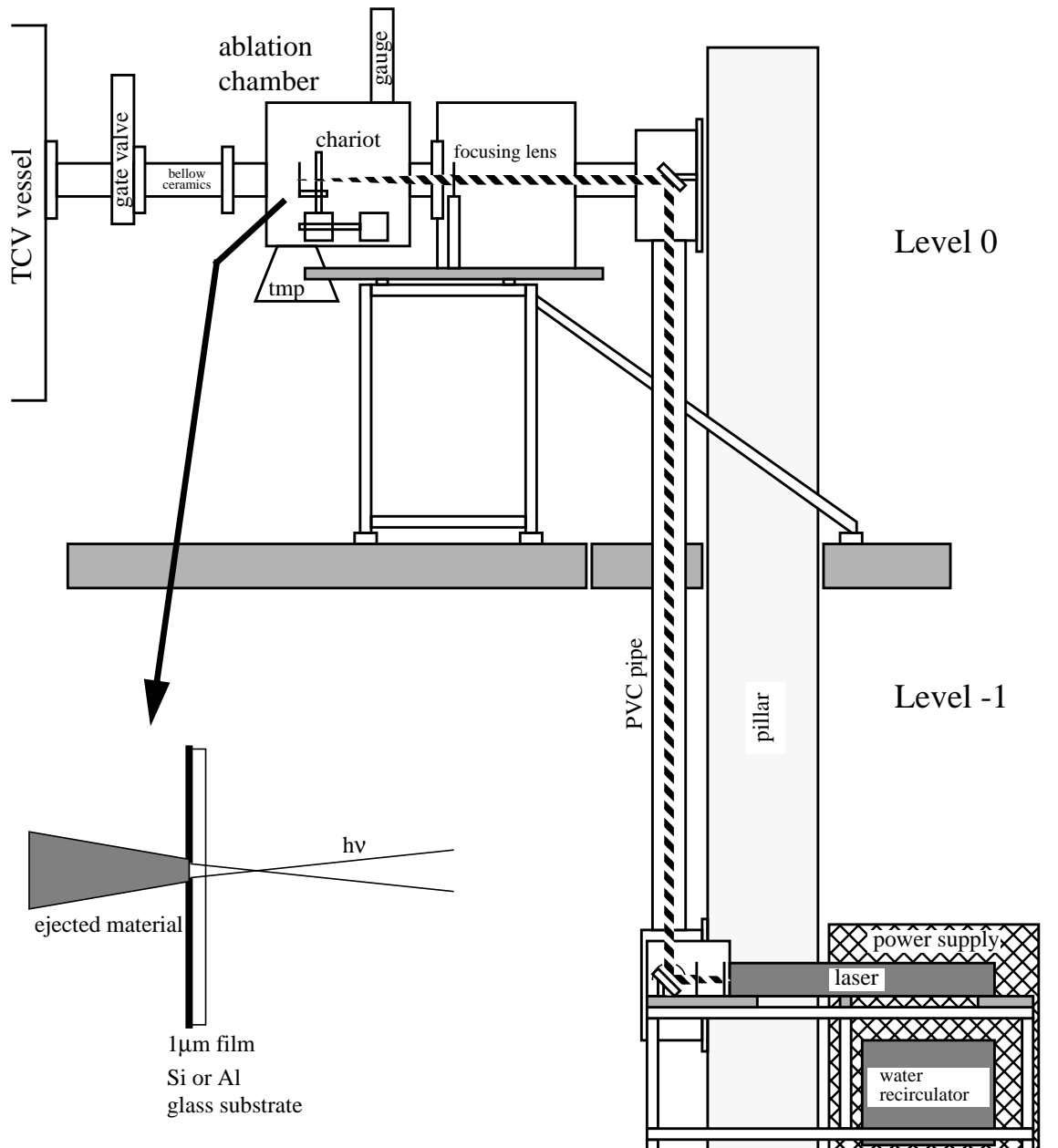
Fig.3.1 - Schematic view of the ablation system. At level -1 of the TCV hall inside the restricted area there are the laser body, the power supply and the cooling water recirculator. In front of the laser output an optical table, described in Sect.2.2, is placed. At level 0 the main component is the vacuum ablation chamber, containing the target and its motion system.

In order to minimise the electrical conductivity of the circulating water, a deionizer has been put in series with the main water circuit external to the pump. The schematic layout of the cooling circuit is shown in Fig.3.2.

The energy necessary to the flashlamps discharge is stored in 8 capacitors of 17.5µF each for high voltage operation up to 12kV, which are slowly charged via a transformer-rectifier system.
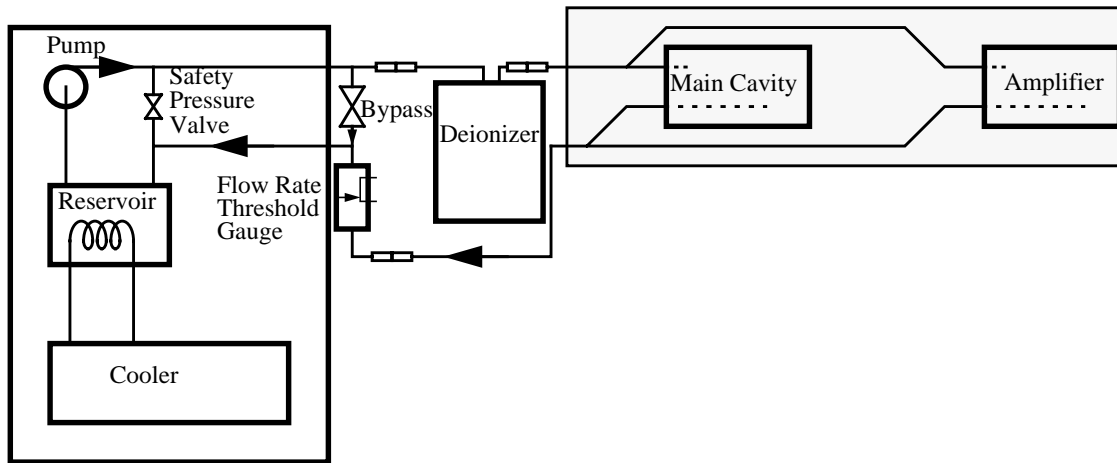

Fig.3.2 - Schematic view of the water recirculating system.

The dangers which are common to any high power laser system required a number of intrinsic features and automatised safety checks in order to be allowed to interface to the TCV tokamak. Security is provided not only via the built-in protections in normal operation, but also in view of possible abnormal events.

For screening against the laser beam, all the optical tables and the beam path were included in opaque PVC pipes and aluminum boxes. A remotely controlled beamstop with a gravitational shutter has been placed into the main optical cavity of the laser.

Protection from high voltage is provided by an interlock wire with microswitches on all access panels in the laser body and power supply, and by a grounding piston whose contact is open exclusively during the charging of the high voltage capacitors. Moreover, the piston is kept lifted for no more than 40s when the capacitors are charged and the laser is ready to fire. The high voltage supply of the laser can only be enabled when the entrance gates to the TCV experimental hall are locked.

3.2 Optical system for the laser beam

At the laser output, the beam has a diameter of 12mm and a divergence of about 1mrad when the laser is operated at full energy. The size of the beam and the divergence are corrected by means of a couple of borosilicate BK7 glass lenses in telescopic disposition. The resulting

Elements	Details	Distance from previous
Lens f=-200mm	Planoconcave, 2", first part of telescope	--
Lens f=+500mm	Planoconvex, 2", second part of telescope	306.5mm
Flat mirror	2", steering to pillar section	50mm
Beamsplitter	2", 10% of light to calorimeter	130mm
- Lens f=-200mm	2", beam size increase for calorimeter protection	~200mm
Mirror	2", steering up to level 0	~0.9m
Mirror	2", steering horizontally to target	~6m
Lens f=+300mm	2", focusing to target, at a distance of 260mm	~0.8m

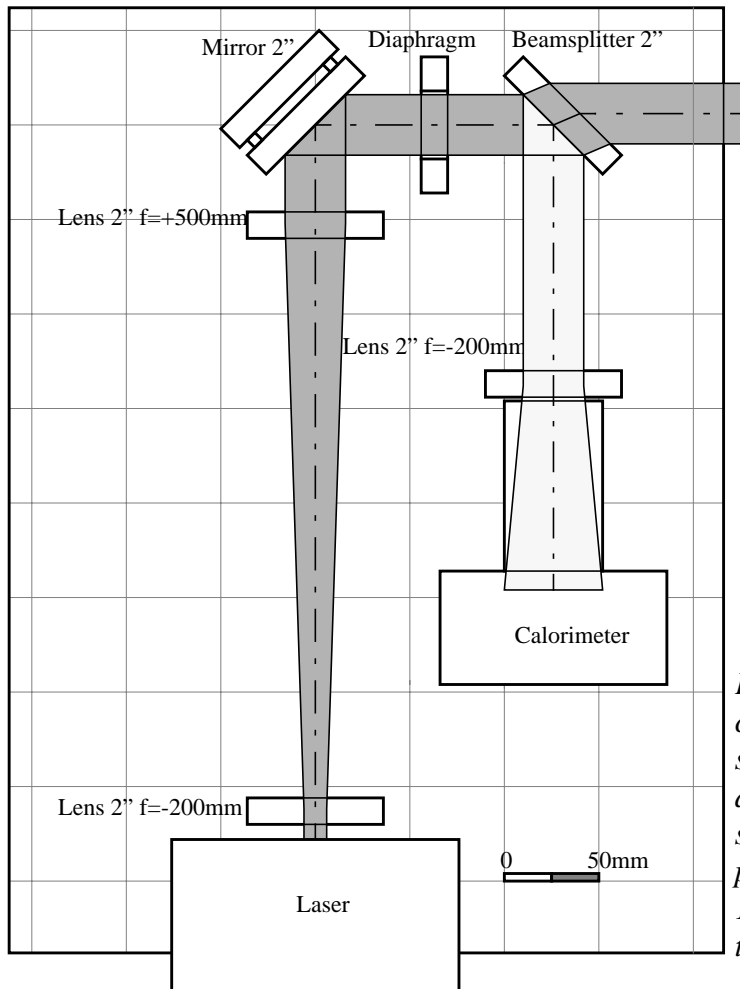*Table 3.2: Optics on the beam path from the laser to the target*

beam of 30mm in diameter is steered with 2 BK7 mirrors along the pillar to the TCV level 0, and with a third mirror to the vacuum chamber containing the target. The beam passes through a BK7 focusing lens just in front of the vacuum chamber window, and its diameter is reduced to the typical value of 4mm when hitting the target with an energy density of about 30J/cm^2. It is possible to vary the spot size and the beam energy density on the target, as the focusing lens is mounted on a chariot allowing an axial displacement of 25mm. The sequence of optics on the beamline is reported in Table 3.2.

After expanding the beam size, still inside the first optical table (Fig.3.3), a beamsplitter sends 10% of the light towards a volume calorimeter (Scientech AC5001) with the aim of checking the laser energy shot by shot. The calorimeter damage threshold is 30J/pulse, but for further protection from an excessive energy density, an additional diverging lens has been placed in front of the entrance. The time response of the calorimeter is 3s and the reading is done remotely via a RS232 connection to the TCV plant control system.

The alignement of the whole optical path is performed by means of a HeNe laser which is mounted on the back of the ruby laser in coaxial position. All mirrors have been coated such as to be highly reflective (>98%) at the ruby laser wavelength, while having adequate reflec-

tivity (>80%) for the HeNe laser (λ=632nm).

Mirror 2" Diaphragm Beamsplitter 2"

Lens 2" f=+500mm

Lens 2" f=-200mm

Calorimeter

Lens 2" f=-200mm

0   50mm

Laser

Fig.3.3 - Layout of the first optical table. The beam (in gray shade) is expanded of a factor 2.5 and its waist extended to keep its size roughly constant on all its path. It is then split in two parts, 10% to the calorimeter and 90% to the target.

3.2.1 Impurity blow-off chamber

The target onto which the laser beam is focused is placed inside a vacuum chamber which has been designed and manufactured at KFKI, Budapest, in the frame of a collaboration with CRPP. The target is placed at a distance of approximately 70cm from the TCV first wall. The connection to the TCV vessel includes a stainless steel bellow, which decouples small mechanical movements, mainly due to vibrations and thermally induced expansions. A ceramic ring provides electrical insulation and avoids undesirable ground loops between the torus to the vacuum chamber groundings. Finally, a gate valve, which is always kept closed, except during the blow-off phase, separates the vacuum of the chamber from the main TCV vacuum and allows independent access to the target chamber. The ablation chamber is pumped down to the 10^{-9}mbar range via a standard turbomolecular pump and does not require bakeout due

to its small dimensions (ϕ=250mm, height=200mm).

Inside the chamber there is a 2-axes moving mechanism for the target displacement (Fig.3.4). Two stepper motors (Phytron ZSS.32 for in-vacuum applications) move the target holder for a maximum run extension of 50mm in each direction, thus allowing the laser beam to reach the target in 144 spots of 4mm of diameter. The target spot is much larger than the focal spot, which has a diameter of less that 0.1mm, such as to provide a number of ablated atoms large enough for clear signals. The best ablation results, in terms of largest and most reproducible signals, were obtained when the focus were placed slightly in front of the target, rather than behind it.
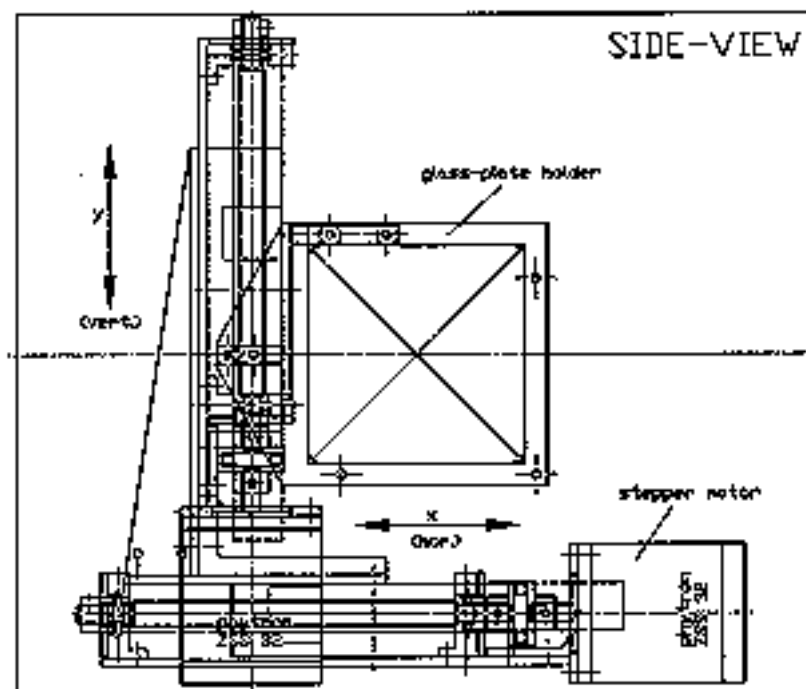
Fig.3.4 - View of the two-chariots moving mechanism for the ablation target. The holder contains a square glass of 50mm side. The stepper motors and the transmission system allow a precision in positioning of 1/160mm

The typical target consists of a thin film of a moderate-Z element deposited on a glass substrate. For the realization of this work, aluminum and silicon films have been used, with typical thicknesses of 200nm to 2μm. The number of ablated atoms is of the order of 10^{17}-10^{18} per pulse. Due to the fact that the laser beam reaches the target through the glass, the material is accelerated toward the plasma by means of pressure action, especially in the case of thicker films. Consequently, the ablated material enters the plasma edge in form of clusters or flakes,

rather than individual atoms.

A video camera has been used to visually monitor the movements and the ablated "holes" of the target directly from the control room during TCV operation.

3.3 Diagnostics

3.3.1 Magnetic measurements

Magnetic diagnostics allow the direct measure of some global parameters, like the plasma current, the stored energy, the loop voltage, the plasma position and geometry, magnetohydrodynamical (MHD) modes and instabilities, as well as of the equilibrium profiles of current density and plasma pressure. The measurements used for equilibrium reconstruction and
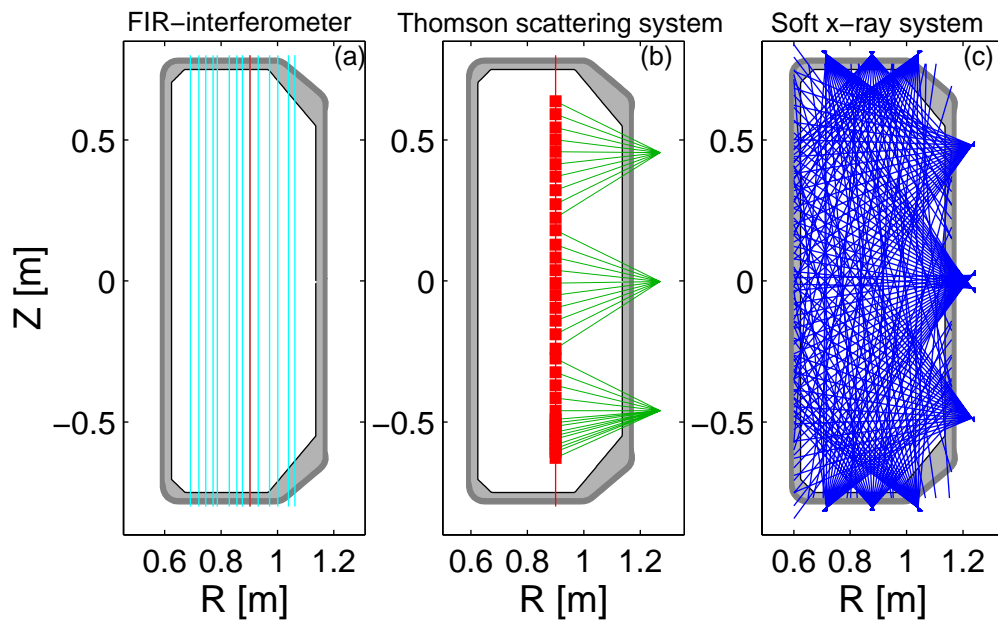
Fig.3.5 - Geometry of (a) the 14 diagnostic chords of the FIR interferometer (the central chord is highlighted), (b) the laser and the 35 viewing chords of the Thomson scattering diagnostic and (c) the 200 lines of sight of the soft x-ray photodiodes used for the detection of the plasma emissivity.

the monitoring of MHD activity on TCV are performed by Mirnov coils[74]. At four different toroidal locations, poloidal arrays of 38 probes are placed behind the graphite tiles inside the vacuum vessel. Two of them, together with flux loops placed outside the vessel, are used for the equilibrium reconstruction. The toroidal MHD activity is monitored by means of

three in-vessel toroidal arrays of 17 probes each which are placed at different heights in order to allow larger signals for shifted plasmas.

The TCV equilibria are reconstructed using the Grad-Shafranov solver LIUQE[75], which provides the geometrical description of the plasma flux surfaces. The standard reconstruction is calculated immediately after each discharge. The accuracy of the LIUQE reconstruction depends on the plasma size and current, which affect the number of useful magnetic measurements from the probe array. The reconstruction can be cross-checked with other measurements from the Thomson scattering and the soft x-ray photodiodes.

3.3.2 Thomson scattering and FIR systems

TCV is equipped with a multi-point Thomson scattering diagnostic for measurements of the electron temperature and density[76]. The measurement is based on the spectral analysis of light which is scattered by free electrons in the plasma. If the wave vector k_i of the input wave is sufficiently large, yielding $k_i \lambda_D \gg 1$, where λ_D is the plasma Debye length, particle correlations can be ignored and the scattered power can be obtained as an incoherent sum of powers from single electrons. The spectral broadening of the scattered radiation, which is due to Doppler effect, provides the electron temperature and its intensity the electron density. The TCV scattering system[77] is shown in Fig.3.5(b). Three almost colinear Q-switched Nd:YAG lasers operate at a pulse rate of 20Hz each with a wavelength of λ=1064nm. The laser beams are injected from the bottom of the TCV vessel at the radial position of R=0.9m. The light scattered from 35 points is collected resulting in a spatial resolution of 40mm in vertical direction along the beam and of 3mm in radial and toroidal directions. The lasers can operate at equidistant temporal separation, thus providing measurements with the rate of 60Hz, or they can be triggered independently.

The electron density measurement is complemented with the data from the FIR diagnostics, whose signals are acquired at a frequency of 100kHz by means of a Mach-Zehnder interferometer using the heterodyne double frequency detection[78]. The system uses the density dependence of the refraction index of an electromagnetic wave crossing the plasma. The refractive index is independent of the direction of propagation and its value is[52]:

$$N = \sqrt{1 - \omega_p^2 / \omega^2} \tag{3.1}$$

If the incident wave penetrates ($\omega_p < \omega$) and the plasma properties vary sufficiently slowly,

the phase of the wave crossing the plasma is shifted by:

$$(\Delta\phi)_i = \frac{\omega}{c}\int_{L_i}\left[\sqrt{\left(1-\frac{n_e}{n_c}\right)}-1\right]dl_i \tag{3.2}$$

in which the definition of *cutoff density*, $n_c = m_e\varepsilon_0\omega^2/e^2$ has been introduced.

For sufficiently low values of the plasma density with respect to the cutoff density, the following approximation holds:

$$(\Delta\phi)_i = \frac{\omega}{2cn_c}\int_{L_i}n_e dl_i \tag{3.3}$$

in which the integral represents the line integrated electron density $\bar{n}_e = \int n_e dl_i$.

On TCV, the phase difference between two laser beams is measured, one of which probes the plasma. The electrical field of the probing beam can be expressed as $E_{prob} = E_2 e^{i[\omega t + \Phi(t) + \Phi_{prob}]}$ in which $\Phi(t)$ is the density driven phase shift, and Φ_{prob} a constant. The reference beam, known as Local Oscillator (LO) is created by Doppler diffraction on a rotating grid[79] and has a frequency offset of $\Delta\omega = 100\,\text{kHz}$ from the probing beam. Its electric field can be represented by $E_{LO} = E_1 e^{i[(\Delta\omega)t + \omega t + \Phi_{LO}]}$.

The two beams are recombined and the resulting intensity is given by:

$$S_{prob} = \|E_{LO} + E_{prob}\| = E_1^2 + E_2^2 + 2\cdot E_1 E_2\cos[(\Delta\omega)t - \Phi(t) - \Phi_{plas}] \tag{3.4}$$

The phase shift $\Phi(t)$ can be determined by comparing the phase of the recombined wave and the phase of a reference signal. The reference signal is obtained by the recombination of the LO beam and a beam not probing the plasma.

The detection system consists of 15 InSb hot electron bolometers in a liquid helium cryostat. The density resolution limit is set by the accuracy of the phase shift measurement, which is around 20 degrees and leads to an approximate limit of $\Delta\bar{n}_e \approx 5\cdot 10^{17}\,\text{m}^{-2}$ on the line integrated density. The line density measurement is used to check and renormalise the density measurements by the Thomson scattering.

3.3.3 The 200-channel soft x-ray detection system

The soft x-ray emission from a plasma originates from electron-ion and electron-impurity bremsstrahlung, recombination radiation and line emission of moderate- and high-Z impurities. In TCV, soft x-ray emission from the plasma is measured with Si photodiodes, which are sensitive up to 10keV. Photons with energy below 1keV, which can originate from im-

Source ions	λ [A]	E_γ [keV]
Al XII	6.6	1.86
	7.7	1.60
Al XIII	6.1	2.05
	7.2	1.73
Si XIII	5.2	2.37
	6.6	1.86
Si XIV	4.7	2.64
	5.2	2.37
	6.2	2.00

Table 3.3: Main impurity SXR lines detected by the photodiode system.

purity line emission, are filtered by a beryllium foil of 47µm thickness, while the active substrate is too thin to absorb high energy photons from hard x-rays. Thus the overall efficiency of the photodiodes, which is shown in Fig.3.6, allows measurements of emission from the hot core of the plasma. In Fig.3.7 the filtering by the beryllium foil and the sensitivity of the photodiodes have been taken into account and the equivalent radiation parameter for silicon in corona equilibrium is shown as a function of the electron temperature. It is evident how photons of energy of
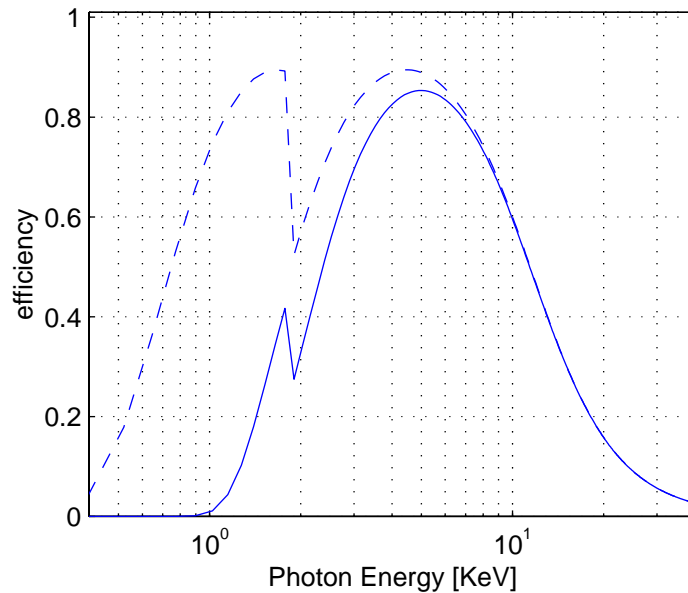

Fig.3.6 - The efficiency $\eta(\nu)$ as a function of the photon energy of a TCV SXR detector alone (dashed line) and filtered by 47µm Be filter (continuous line). The photodiode is passivated by 55nm Si_3N_4. A dead layer of 0.8µm and an effective thickness of 200 µm are assumed.

at least 1keV which contribute to the signal are emitted only by electrons whose temperature is above approximately 400eV.

Aluminum and silicon have been chosen to be the injected elements in TCV plasmas according to the central temperature in typical ohmic discharges, which is in the range of 600-900eV. At these temperatures the impurities are ionised to the He-like and H-like states and

provide a strong line emission in the soft x-ray spectrum, above the sensitivity threshold of the TCV photodiode array. As shown in Fig.2.4 for corona equilibrium, a fraction of fully stripped silicon is present in the plasma centre for the above temperatures, which contributes to the signal with bremsstrahlung radiation.

As far as Li-like ions are concerned, the most energetic photon energies in line emission have energies of 499eV and 421eV for Si XII and Al XI respectively; therefore the filtering properties of the system do not allow the detection of such contributions.

The TCV SXR photodiode system[80] consists of 10 pinhole cameras, each comprising one strip of 20 silicon pin diodes. The cameras are distributed in 9 ports of a single poloidal sector, fully covering the poloidal section of the TCV vessel, as shown in Fig.3.5(c). The resulting integrated signals from the 200 lines of sight can be used to perform a tomographic reconstruction of the local x-ray emissivity for all plasma configurations, with a spatial resolution of 30-40mm. The advantage of a high number of viewchords lies in the possibility to resolve any soft x-ray distribution regardless of asymmetries in the emission and of plasma geometry. In particular, hollow profiles in the SXR emission, caused by the increased emissivity of soft x-rays at the plasma edge during the influx phase of impurities, can be spatially
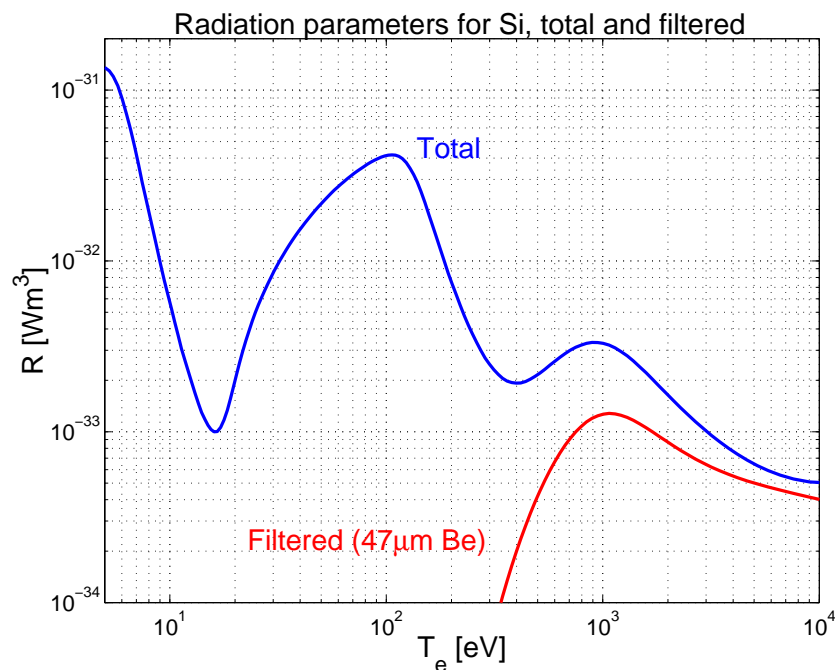

Fig.3.7 - Total and filtered radiation parameter of Si ions in corona equilibrium as function of the electron temperature. Filtering takes into account both the 47μm Be foil and the spectral sensitivity of the photodiodes.

detailed. A brief exposition of the inversion principles is given in Section 3.3.4.

The temporal resolution is limited by the acquisition system, allowing a maximum sampling rate of 80kHz, which is far faster than typical phenomena of particle transport and allows a detailed resolution of sawtoothing events. The spatial and temporal resolutions allow among other the precise determination of the sawtooth inversion radius and the role of sawteeth in the transport of impurities in the plasma core.

3.3.4 Tomographic inversion

The principle of tomography consists in the reconstruction of the local properties of an object by means of line integrated measurements. In plasma physics the spatial distribution of the radiation emitted by a plasma is collected along viewchords by means of photodiodes and it is reconstructed via mathematical methods. Usually the emissivity distribution is reconstructed on a 2-D poloidal plane by means of a number of detectors of the order of 100. In absence of MHD activity with very high toroidal mode number, in a tokamak plasma the radiation is assumed to be constant in toroidal direction on the size of collimated viewchords (about 1.5cm in TCV).

Provided the plasma is optically thin in the considered spectral range, it can be shown[19] that the total measured power P_i reaching the detector i through an aperture can be written as:

$$P_i = \frac{(A\Omega)_i}{4\pi} \int_{L_i} dl \int G(\bar{r}, \nu)\eta_i(\nu)d\nu \qquad (3.5)$$

where $(A\Omega)_i$ is the geometrical etendue of the system detector-aperture, $G(\bar{r}, \nu)$ is the local spectral emissivity of the plasma along the viewchord axis L_i (called also line of sight) and $\eta_i(\nu)$ is the efficiency of the detector-filter combination.

Eq.(3.5) is generally put in the form:

$$f_i \cong \frac{P_i}{(A\Omega)_i/(4\pi)} = \int_{L_i} c_i g(\bar{r})dl \qquad (3.6)$$

in which the term at left is measured by the acquisition system, $g(\bar{r}) \cong \int G(\bar{r}, \nu)d\nu$ is the total plasma emissivity and c_i is a calibration factor for each detector, which includes efficiency and filtering and provides a spectrum averaged photodiodes response to plasma emissivity[80]. The tomographic problem is thus reduced to the mathematical research of a solution of a system of integral equations of the form of Eq.(3.6), in which the distribution $g(\bar{r})$ has to be determined.

The resolution of the system for TCV plasmas is usually performed by means of a pixel method with a Minimum Fisher Information (MFI) constraint[19]. The plasma cross section is divided into arbitrary shaped pixels which have to be small enough so that in each one the emissivity can be considered constant. On the other hand, their number has to be limited in order to keep a reasonable tractability of the system of equations.

The measured power of each detector can be expressed as:

$$T_{i1}g_1 + T_{i2}g_2 + \dots + T_{iN}g_N = P_i \tag{3.7}$$

where g_j is the plasma emissivity inside the pixel j and the coefficients T_{ij} represent the fraction of the radiation emitted by the pixel j and measured by the detector i. The problem is usually posed in the matrix form:

$$\boldsymbol{f} = \boldsymbol{T} \cdot \boldsymbol{g} \tag{3.8}$$

In the simplest approximation the element T_{ij} equals the length of the line of sight L_i inside the pixel j. In the most common case, in which the number of pixels n_{pix} is bigger than the number of detectors n_{det}, the problem is underdetermined and an exact solution can always be found in the (n_{pix}-n_{det})-dimensional space of the kernel of Eq.(3.8). In order to get a unique and sensible solution it is necessary to minimise a functional ϕ which can be written as:

$$\phi = \frac{1}{2}\chi^2 + \alpha R \tag{3.9}$$

where R is a regularising functional, α is a definite positive weight parameter and χ^2 is the error functional defined as $\chi^2 = (\tilde{\boldsymbol{T}} \cdot \boldsymbol{g} - \tilde{\boldsymbol{f}})^T \cdot (\tilde{\boldsymbol{T}} \cdot \boldsymbol{g} - \tilde{\boldsymbol{f}})$. The abbreviations $\tilde{\boldsymbol{f}}_i = \tilde{f}_i / \sigma_i$ and $\tilde{\boldsymbol{T}}_{ij} = \boldsymbol{T}_{ij} / \sigma_i$ have been used, with σ_i being the error of the measurement of the chord brightness f_i.

As an example, R can be set as to be a functional like $R = \left\|\dfrac{d\boldsymbol{g}}{dx}\right\|^2 + \left\|\dfrac{d\boldsymbol{g}}{dy}\right\|^2$ which leads to smooth solutions $\boldsymbol{g}$. In this case we can discretise the problem and write

$$\boldsymbol{R} = (\nabla_x\boldsymbol{g})^T \cdot (\nabla_x\boldsymbol{g}) + (\nabla_y\boldsymbol{g})^T \cdot (\nabla_y\boldsymbol{g}) \equiv \boldsymbol{H} \cdot \boldsymbol{g} \tag{3.10}$$

in which the definition of $\boldsymbol{H}$ is included. The solution to the tomographic problem can be found by minimising the functional

$$\phi = \frac{1}{2}(\tilde{\boldsymbol{T}} \cdot \boldsymbol{g} - \tilde{\boldsymbol{f}})^T \cdot (\tilde{\boldsymbol{T}} \cdot \boldsymbol{g} - \tilde{\boldsymbol{f}}) + \alpha \boldsymbol{g}^T \cdot \boldsymbol{H} \cdot \boldsymbol{g} \tag{3.11}$$

Setting all partial derivatives $\partial\phi/\partial g_j$ to zero in Eq.(3.11), the set of n_{pix} equations can be obtained:

$$(\tilde{T}^T \cdot \tilde{T} + \alpha H) \cdot g = \tilde{T}^T \cdot \tilde{f} \qquad (3.12)$$

which has to be solved for g. The correct parameter α is iteratively found by means of an iteration in which guesses on its values are made until an interpolated value is obtained so to minimise the corresponding functional ϕ.

While this choice of the regularising functional tends to provide too flat emissivity profiles, a different definition can be introduced, which is empirically found to be more satisfactory than a simple first order regularisation[81]. This alternative choice is based on the Fisher information of a distribution $g(x)$, which is defined as:

$$I = \int \frac{g'(x)^2}{g(x)} dx \qquad (3.13)$$

where the prime ' denotes the derivative with respect to the variable x. The MFI technique is essentially a smoothing principle whose weight is stronger in zones where the distribution is low. This property is well suited for SXR tomographic inversion as it preferentially smooths the emissivity in regions of poor signal-to-noise ratios and allows more freedom where the signal is high. From the mathematical point of view, the MFI requirement is fulfilled[19] in an iterative way, by defining the regularising matrix H as:

$$H^{(n)} = \nabla_x^T W^{(n)} \nabla_x + \nabla_y^T W^{(n)} \nabla_y \qquad (3.14)$$

in which $W^{(0)}$ is the identity matrix. Then the system of equations

$$(T^T \cdot T + \alpha H^{(n)}) g^{(n+1)} = T^T \cdot f \qquad (3.15)$$

is solved and the solution $g^{(n)}$ is used to calculate the new weight matrix $W_{ij}^{(n+1)} = \delta_{ij}/g_i^{(n)}$.

The iteration continues until the difference between $g^{(n)}$ and $g^{(n+1)}$ becomes negligible and in practice $n=2$ is sufficient. The correct parameter α is iteratively found for each n by requiring that $\chi^2 \approx n_{det}$.

An example of the tomographic reconstruction of the plasma emissivity in the SXR part of the spectrum is shown in Fig.3.8. The poloidal cross section in Fig.3.8(a) has been taken at t=0.6s just before the impurity injection, while in Fig.3.8(b) the time evolution of the SXR

emissivity along a vertical cut through the plasma centre is reported.

It has to be remarked that the tomographic reconstruction of the soft x-ray emissivity requires further mathematical treatment in order to separate the bulk plasma and the injected impurity contributions. If the background intensity is constant on average and regular sawteeth are present, it is possible to take it into account by subtracting the plasma emissivity at a given time before injection, for which the time difference is an integer multiple of the sawtooth period.
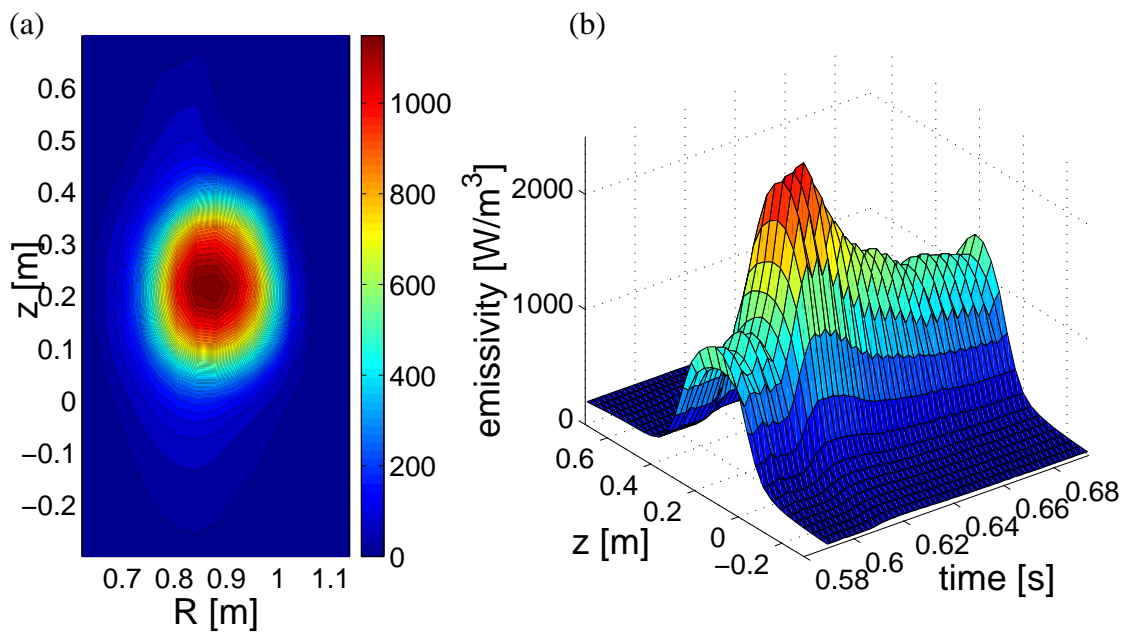
Fig.3.8 - (a) The tomographic reconstruction of the plasma emissivity in the soft x-ray spectral range at t=0.6s. (b) The time evolution of the plasma emissivity along a vertical cut during an impurity injection, shot #21022.

3.3.5 SPRED spectrometer

The electromagnetic emission in the VUV spectral region from TCV plasmas is detected using the SPRED spectrometer[82, 83], which is particularly useful to monitor moderate- and high-Z impurities in medium ionized states present in the plasma periphery.

The heart of the optical system is a diffraction grating whose grooves are holographically recorded in a curved pattern in order to correct for aberrations, astigmatism in particular, and to maximize the spectral sensitivity. In the basic configuration, the detection system is composed by a single microchannel plate (MCP) coupled via optical fibers to a photodiode array

(PDA). A VUV photon hitting the MCP is converted into a photoelectron which undergoes a cascade multiplication towards a phosphor screen normally held at a potential of +4keV; the electrons are thus converted on the screen to visible light. The fiber optic image conduit can allow the reduction of the image in the case the MCP and the PDA have different sizes. The MCP is in optical contact with the PDA, which contains 1024 pixels of 25μm of size.

In TCV the SPRED (focal length 0.3m) is equipped with two gratings which allow detection of ultraviolet radiation in the range 180-1500A (with 450g/mm) and in the range 140-440A (with 2105g/mm). The detection system has been modified with respect to the basic configuration as the MCP has a size of 50mm and is coupled in a 1:1 scale with two standard PDAs covering the same size and holding together 2048 pixels.

On TCV the SPRED is mounted to the bottom part of the vessel and its line of sight is oriented vertically. As the acquisition system allows one spectrum to be read out every 5ms, the time resolution does not allow the detailed observation of the impurity influx phase. However, the observation of the depletion phase of low ionised stages of injected impurities can be done in the case their confinement time is comparable to that of the impurities in the plasma core.

3.3.6   OMA spectrometer

The spectrometer contains an ACTON monochromator of Czerny-Turner type (1m of focal length) equipped with a holographic diffraction grating of 1200, 1800 or 2400 g/mm. The Optical Multichannel Analyser detector works on the same principle as of the SPRED spectrometer, which has been described above, and allows the observation along a single viewline. The light, which is brought to the detector by means of an objective and an optical fiber, is collected through a window which is placed at the side of the injection system.

The signal acquisition has been performed with a maximum temporal resolution of 1.3ms, which has been sufficient to obtain a number of points during the injection phase. The spectral window has been centred on the neutral silicon line at λ=5708.4A and the acquisition has been limited to a narrow range of wavelengths in order to improve the temporal resolution. The time evolution of the signal is very similar for all the analysed injections, and one example is reported in Fig.3.9. The recorded signal being biased by the relatively long decay time of the phosphor screen, a deconvolution is necessary in order to determine the actual evolution of the source.

In the first order case, the response of the system can be described by a differential equation of the type

$$\frac{df}{dt} = -\frac{1}{\tau}f + S \qquad (3.16)$$

in which f is the output signal, t is the constant decay time of the phosphor and S the source. The value of τ, which depends on the integration time during the spectra acquisition, is determined by means of an exponential fit performed on the tail of the OMA signal.
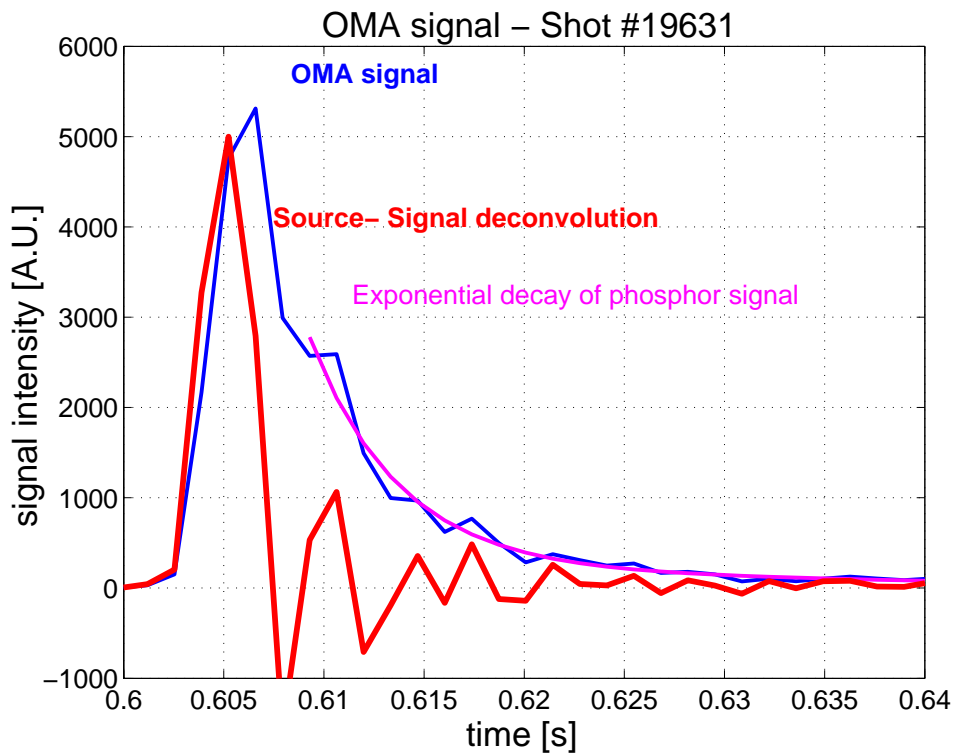

Fig.3.9 - Time evolution of the OMA signal (blue line) and of the deconvolution (red line), made according to Eq.(3.16) with a time constant τ=4.5ms, following silicon injection in shot #19631. This value of τ has been determined by means of a fit of the tail of the signal.

The results of the deconvolution are shown in Fig.3.9. Typically the decay of the signal has a time constant τ in the range of 4-5ms when the acquisition is performed at maximum rate. The deconvolution (red line), which suffers of a higher noise because of the differentiation, shows a peak of duration of about 4ms, and is our best indication for the time evolution of the source of neutrals following injection. An estimation of the characteristic time for the first ionisation of silicon at the plasma edge can be done with the following expression:

$$t_{ion} \approx \frac{1}{\langle \sigma v \rangle n_e} \qquad (3.17)$$

68

which at the plasma edge ($T_e \approx 10\,\text{eV}$ providing $\langle \sigma v \rangle \approx 10^{-13}\,\text{m}^3/\text{s}$[84], $n_e \approx 10^{18}\,\text{m}^{-3}$) gives $t_{ion} \approx 10\,\mu\text{s}$. We can thus conclude that the ionisation is far faster than the characteristic time of relaxation of the phosphor and can be neglected in the deconvolution. Moreover, the ionisation time is much shorter than the source duration which has been presented above. This difference can be justified by the spread in the time-of-flight of impurity clusters as well as by the time necessary for their complete corrosion by the plasma.

3.4 Concluding remarks

The study of transient phenomena of transport of moderate-Z impurity particles in TCV plasmas requires diagnostics capable of detecting ultraviolet and soft x-ray line radiation from partially stripped ions in order to cover all plasma regions. The repetition rate of the acquisition provided by the SXR photodiodes system allows the observation of fast transport phenomena like sawtooth activity, which can affect the confinement of impurities. As it will be shown in Section 4.1, in the case of silicon only the radiation from the He-like and H-like ions contributes to the enhanced x-ray emission, while all other line emission from lower ionised states is filtered out.

In addition to the characterisation of the impurity behaviour, relevant plasma parameters have to be measured. The main parameters are the electron temperature and density, as well as the plasma geometry which is fundamental for the study of its effects on the impurity transport.

4. EXPERIMENTAL RESULTS ON IMPURITY CONFINEMENT IN TCV

Unwanted moderate-Z impurities are common constituents of many tokamak plasmas, as metallic atoms are easily produced at the plasma edge by sputtering, arcing on internal structures like walls, limiters, antennas, diagnostics. As these impurities may radiate enough power to affect the energy confinement time, it is very important to understand their behaviour and to look for possible plasma configurations that may provide high energy confinement times and as low as possible impurity confinement times. The possible accumulation of impurities in the plasma core has been presented in Section 2.3 in the frame of the neoclassical theory of transport, and it has been observed in several investigations[64, 85, 86].

Impurity control techniques can range from the wall conditioning, ergodization of the boundary magnetic surfaces in order to distribute the heat flux to the walls, build-up of transport barriers with additional heating in order to possibly keep the heat in the plasma core and the impurities outside[62]. Other mechanisms include MHD events like sawtooth activity to prevent central accumulation and ELMs for fast impurity expulsion from the plasma edge.

The TCV tokamak offers the unique possibility to investigate the effects of plasma geometrical shaping on the confinement times of energy and impurities. In this Chapter, the main results of several impurity injection campaigns are presented, in which the plasma geometry was explored together with the variation of different plasma parameters, like toroidal current, electron density and toroidal magnetic field. The global impurity confinement time, whose definition will be given in the following, has been evaluated from the exponential decay of the line integrated soft x-ray signals, and different configurations of parameters are identified for which the ratio τ_{imp}/τ_{Ee} shows favourable trends.

For the realisation of this work, almost all the injections have been performed in deuterium plasmas, except in a few cases in which a variable mixture of deuterium and helium were used.

4.1 Impurity signals in TCV

In this Section the raw signals which have been detected from TCV plasmas following impurity injection by means of the laser blow-off technique are presented. As it was described in Chapter 3, the ablation apparatus produces a short burst of metal atoms entering the vacuum vessel in radial direction at the height of $z = 40\,cm$ above the mid-plane. At the typical temperatures of an ohmic TCV discharge, aluminum or silicon are ionised to the He-like and H-like states and provide a strong line emission in the soft x-ray spectrum, which can be easily detected by the SXR photodiode array[49]. The ion state distribution of silicon as a function of plasma temperature in the corona model approximation is shown in Fig.2.4. It is clear that the He-like state is largely dominant in all the central part of TCV plasmas where the temperatures lie over the 400eV. The fully stripped state which would contribute only with the bremsstrahlung radiation appears in very low concentrations.
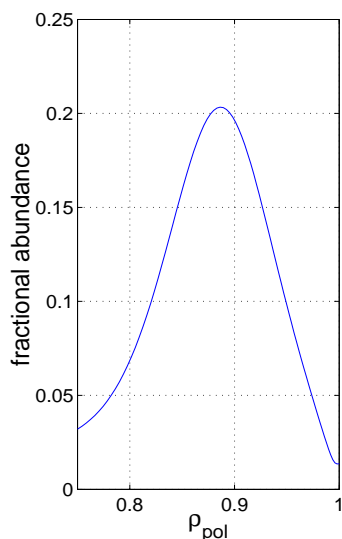
Fig.4.1 - STRAHL simulation of the fractional abundance of Si^{11+} ions as a function of the normalised radius for shot #19785, in which transport has been taken into account. The transport parameters were chosen to be $D = 0.05 + 0.25\rho_{pol}^2\,m^2/s$ and $v = 4.3\rho_{pol}\,m/s$ outward.

In similar experiments performed in JET[39], Tore Supra[40] and ASDEX Upgrade[37] heavier elements were injected, like Fe, Ni, Ag, Mn, Ti. The higher temperatures reached in such experiments allow the measurement of line emissions over a wider span of different ionised states.

Electromagnetic emission from the plasma periphery is best detected by VUV spectrometers, like the SPRED, which for injections in TCV has been used to measure the Si^{11+} line at 499.4A. We note that line emission from a single moderately ionised species mostly come from very narrow areas at the plasma edge[31], where the temperature gradients are high. In Fig.4.1, the localisation of the Si^{11+} ions is shown for a typical plasma in which transport is taken into account.

The signals considered in the following are in general line integrated measurements, whose temporal evolution will be heuristically described taking as example a real signal from the SXR system. A correlation with the transport parameters, i.e. radial diffusivity, convective velocity, sawtooth radius and frequency will be made

in Chapter 5, in which the measured signals will be reproduced by means of the code STRAHL.

4.1.1   Line integrated SXR signals

Broadband electromagnetic radiation, as produced by injected impurities, is measured by the 200 channel soft x-ray photodiode system. Basically three components contribute to the time evolution of raw signals during the impurity residence time in a plasma. The first contribution is a mostly constant background coming from the main plasma particles and light intrinsic impurities like carbon. As described in Section 2.2, the radiation from the plasma centre is produced mainly by bremsstrahlung from electrons colliding with fully stripped hydrogen and carbon ions, and by recombination radiation from carbon. The second contribution to the signal shape is given by the sawtooth activity, whose typical temporal signature is shown in Fig.1.8. The third one is provided by the moderate-Z injected impurities, whose signal has to be clearly distinguished from the previous ones in order to obtain a quantitative analysis of impurity transport in the plasma.

The sawtooth amplitude is often of the same order of magnitude as the typical pulse shaped signal due to impurities, and the removal by means of mathematical techniques is necessary. Provided that the background signal and the sawtooth activity are regular, they can easily be separated from the impurity contribution by means of the Generalised Singular Value De-
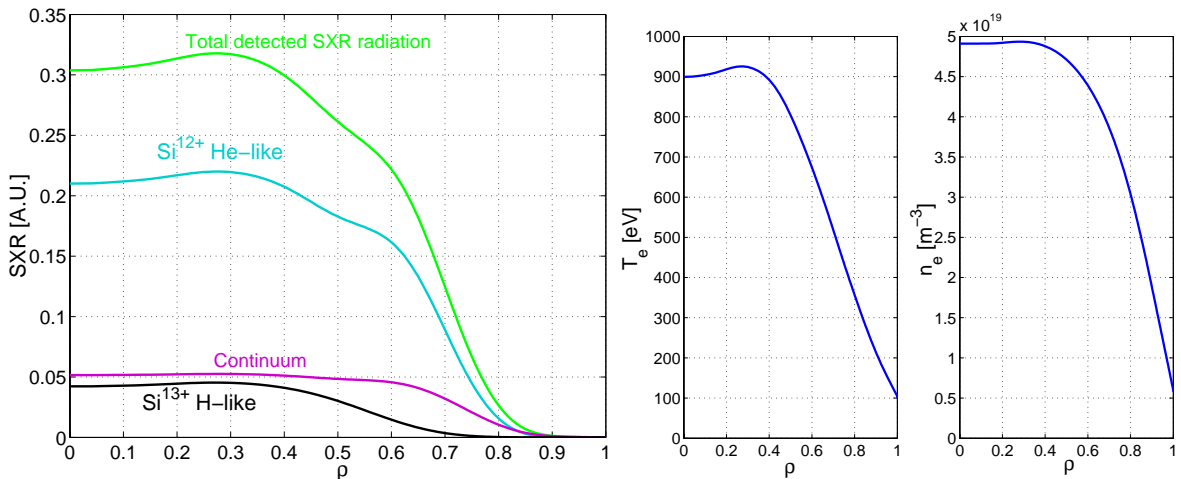

Fig.4.2 - Plot of the ionic species contribution to the radiation power in the soft x-ray spectrum after filtering as a function of the poloidal flux label. Data are based on a STRAHL simulation on shot #21022 ($D = 0.05 + 0.61\rho_{pol}^2$, $v = 3.8\rho_{pol}$), for which the plasma parameters are plotted aside. The hollow distribution in the power density reflects the hollow profiles of the electron density and temperature.

composition method (GSVD)[87], which is described in Appendix A. The clearest line integrated signals are obtained when the background is constant or linearly changing and when the period of sawteeth is constant.

As far as signals from the TCV soft x-ray photodiodes are concerned, the spectral sensitivity of the system has to be taken into account in order to determine what part of the silicon population in a plasma really contributes to the recorded signal. This is achieved by means of STRAHL calculations which consider the filtering properties of the beryllium foil and the passivation layer on the photodiodes surface, together with the effective thickness of the diodes. As described in Section 3.3.3, only line radiation coming from hydrogen-like and helium-like contribute to the soft-x ray recorded signals, together with part of the bremsstrahlung and recombination radiation (Fig.4.2). Calculations with STRAHL, not detailed here, show that almost the totality of the latter contribution comes from lithium-like or more highly ionised species. The major consequence is that the analysis of the soft x-ray signals produces information mainly from the plasma centre, while there is little contribution from the edge. The analysis of many injections in TCV shows that line integrated signals can
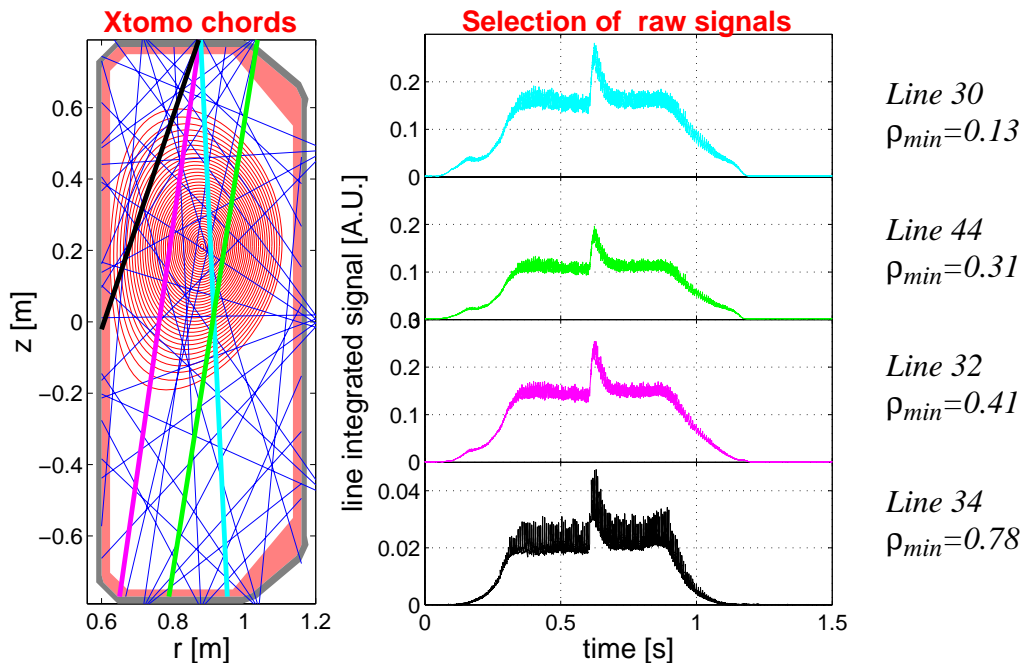

Fig.4.3 - Raw line integrated signals from TCV ohmic discharge #19785 following silicon injection at t=0.8s. Signals from various selected chords show the impurity peak superposed to a constant background and sawtooth activity. In the case of peripheric viewchords the increase of emissivity is of the same intensity as sawteeth.

be considered useful if the closest point of the viewchord lies inside $\rho_{pol} = 0.75$, and only in the case GSVD provides clean filtered data. Otherwise, the typical peak-shaped signal due to impurities can still be found, but the uncertainty on its intensity becomes very high as the noise and the sawteeth are almost of the same size.

Typical raw signals from a silicon injection in TCV are shown in Fig.4.3, where the peak intensity against the background is shown to be varying with the position of the chords. It can be qualitatively observed that the line integrated signal from chord 34 does not allow an easy separation of the impurity and the sawteeth contributions.

An example of a line integrated signal following GSVD is shown in Fig.4.4. In this case the laser ablation of the silicon thin film has been performed at $t = 0.6\,$s, while the signal starts deviating from the background about 2ms later, due to the time of flight of impurities and to the diffusion toward hotter parts of the plasma. The parameters of the target plasma are $\bar{n}_e = 3.5 \cdot 10^{19}\,\mathrm{m}^{-3}$ line averaged, $T_{e0} \approx 900\,$eV, $\kappa = 1.60$, $\delta = 0.25$, $I_P = 355\,$kA. The first part of the signal presents sudden increases in the emissivity at the times corresponding
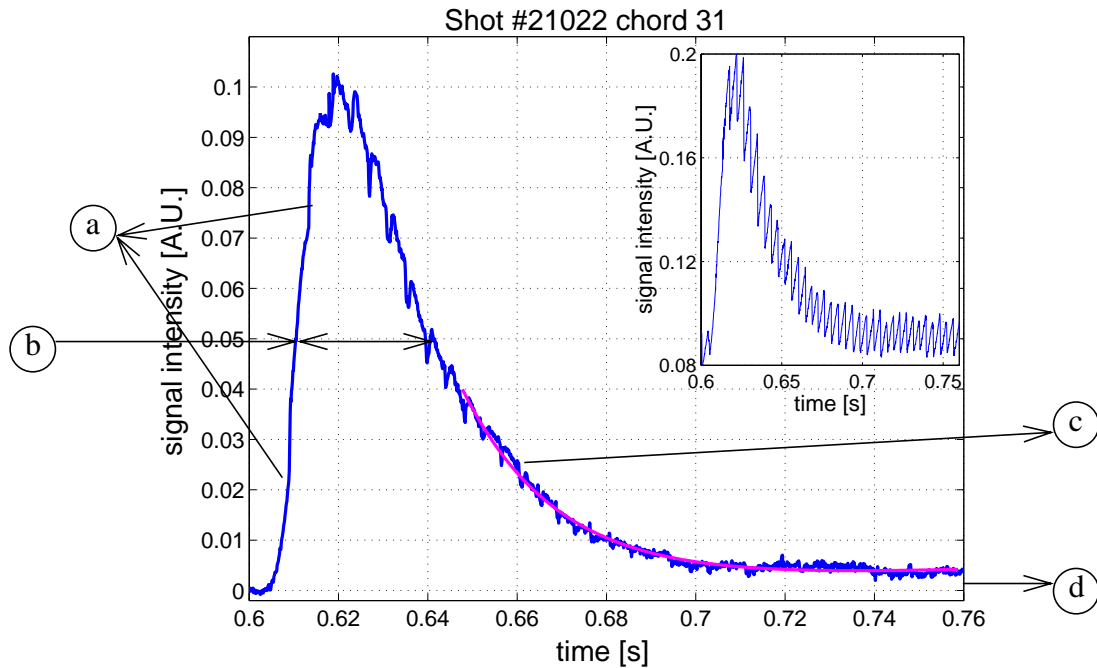
Fig.4.4 - Temporal evolution of a line integrated signal from impurities after background and sawteeth removal. (a) Sudden increases in the signals corresponding to sawtooth crashes; (b) full width half maximum (fwhm) of the signal; (c) exponential decay of the signal, with the fitted exponential function superposed; (d) asymptotic residual signal due to a weak recycling from walls. In the inset, the raw signal before GSVD treatment.

to sawtooth crashes. This phenomenon can be observed also in the raw signals provided the contribution of sawtooth activity in the background does not dominate the signal shape, so that the increased emissivity due to the injected impurities overtakes the reduction of emissivity deriving from the main plasma and the intrinsic impurities. The so-called inverted sawtooth, which has been observed in many similar experiments[32, 37], is a consequence of the hollow impurity radial profile just after injection, and of the sawtooth dynamics (Fig.4.5). The central part of the density profile of silicon is flattened during the sawtooth crash through an abrupt inward movement of particles, while peaked profiles of particle densities, including electrons and intrinsic ions, are flattened by an outward movement. This phenomenon of redistribution takes place inside the sawtooth mixing radius.
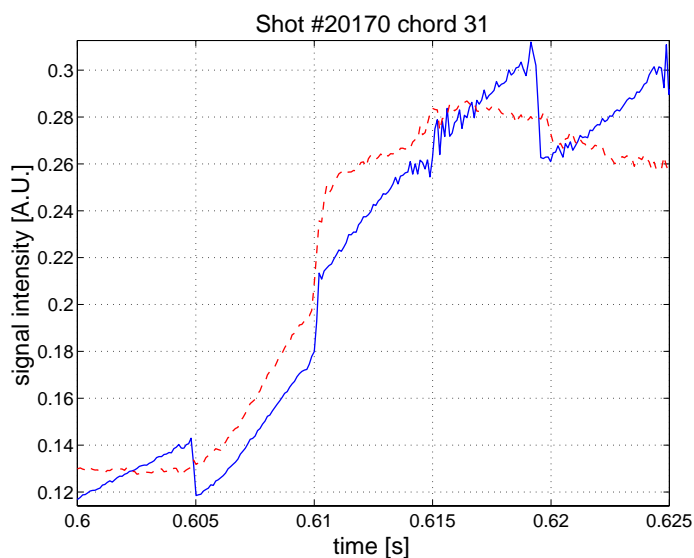
Fig.4.5 - Detail of the impurity peak during the influx phase of particles. The sawtooth crash at t=0.61s corresponds to a sudden increase of the signal. The effect is visible on the raw signal (full line) as well as on the GSVD filtered one (dashed).

The distribution of the SXR emissivity from impurities during the influx phase is shown in Fig.4.6 along a vertical cut passing through the centre of the plasma. It is clear how the profile is transiently hollow except at the end of the first sawtooth crash, which suddenly increases the impurity concentration in the plasma centre. In the following, the transport of impurities from the plasma periphery makes the SXR profile hollow again, up to the second crash.

During the outflux phase when the signals are decreasing, the sawtooth activity contributes with an intensity of the same magnitude as before the injection, as shown in Fig.A.3(b). In this phase the central profile is mainly flat due to sawtooth activity despite the low value of the central diffusivity, except around the mixing radius of sawteeth, where a net flow of particles is exchanged with the peripheral part of the plasma.

4.1 Impurity signals in TCV

An evidence of the hollow profile in TCV discharge #20165 can be highlighted by means of the tomographic reconstruction[19] of the soft x-ray emissivity during the impurity transport in the plasma. The reconstructed profiles have been filtered with the Singular Value Decomposition technique[88] or SVD, which identifies a set of spatial eigenfuctions whose first elements (topos) contain most of the information of the profile. Their relative temporally
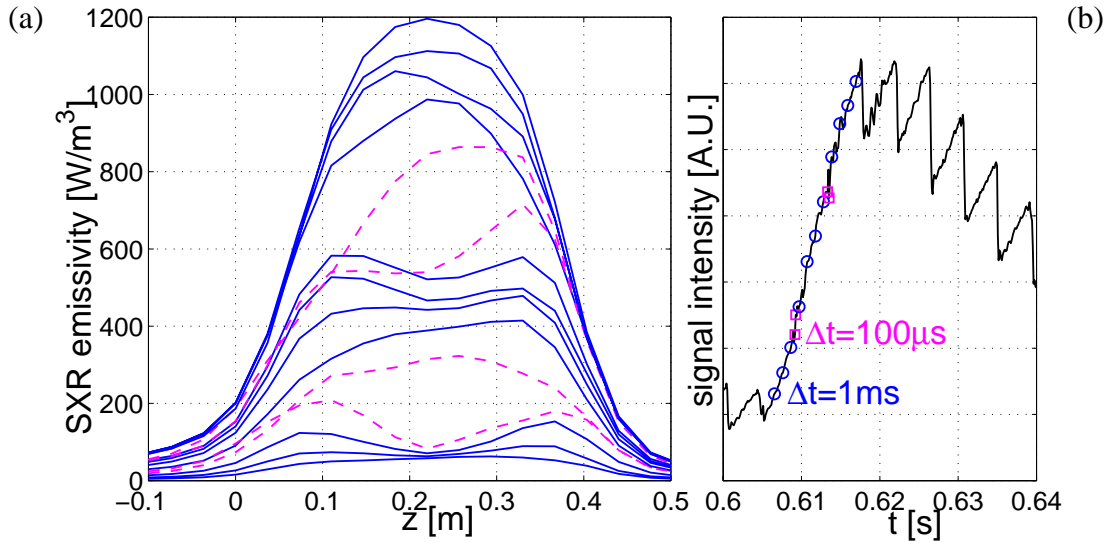

Fig.4.6 - (a) Vertical cuts of the SXR emissivity distribution during impurity influx in shot #21022. The full lines are taken at intervals of 1ms, while the dashed lines, separated by 100μs, are taken just before and after the sawtooth crashes as shown in (b). The background has been removed by assuming a constant sawtooth activity in frequency and intensity from the bulk plasma, as stated in Section 3.3.4.

varying eigenvalues are called chronos. As the eigenmodes are sorted as to concentrate the dominant features in the first elements of the set, often all the subsequent can be discarded, as their relative weights, called singular values, are much smaller. For clarity, in Fig.4.7 only the two first topos-chronos couples are shown. The first one (Fig.4.7(a,b)) includes most of the background plus the information of the soft x-ray emission by the impurities during and after the influx phase towards the plasma centre. Many of the features on the emissivity distribution during the influx phase anyway are included in the second topos-chronos couple (Fig.4.7(c,d)) in which a significant increase of the eigenmode weight can be observed in the first milliseconds after impurity injection. The evolution of chronos #2 shows how the importance of the hollow component is reduced by two consecutive sawtooth crashes at $t = 0.611\,\text{s}$ and $t = 0.616\,\text{s}$ during which the impurity concentration profile tends to be flattened and consequently the hollow topos tends to lose its relative weight.

During the depletion phase almost all line integrated signals show a common decay time which is obtained by an exponential fit of the form:

$$S = (at + b) + c \cdot \exp\left(-\frac{t - t_{max}}{\tau}\right) \tag{4.1}$$

where the linear part $(at + b)$ accounts for the residual asymptotic signal and a linear background, while the exponential part contains the impurity contribution. The time constant τ is defined as the *global impurity confinement time*, or *impurity lifetime*, and it is a measurement of how long impurities stay inside a plasma before leaving through the edge. This definition
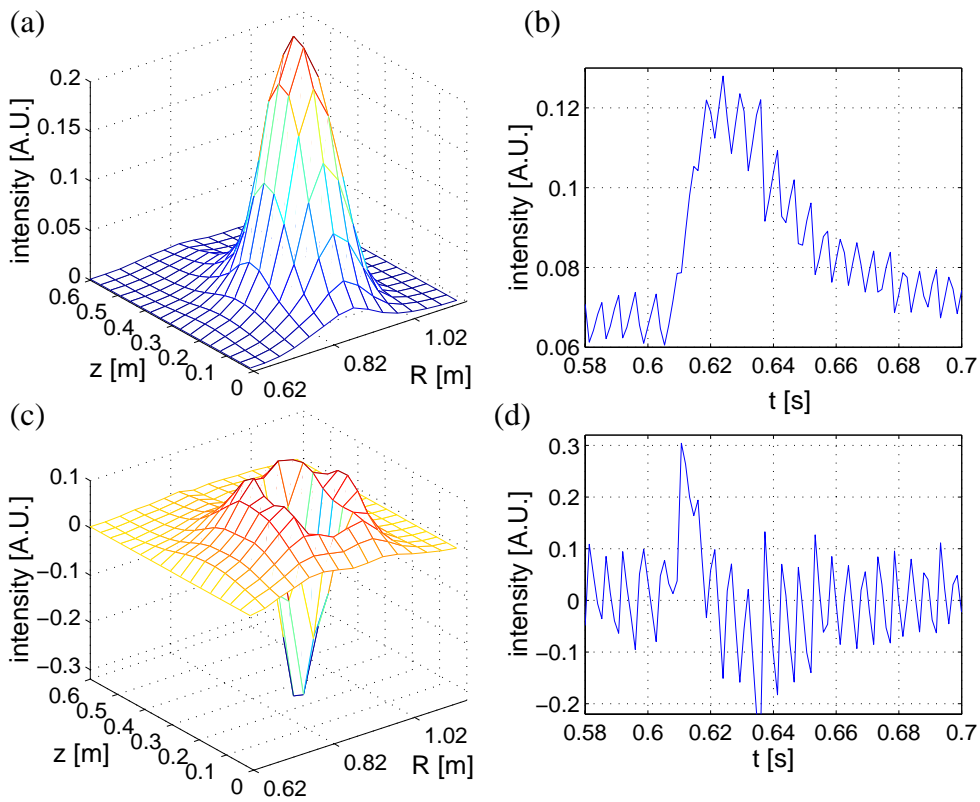
Fig.4.7 - SVD decomposition of the reconstructed soft x-ray profile for shot #20165 in the time interval t=0.58s to t=0.7s during a silicon injection. In (a,b) the first topos/chronos pair is shown. In (c,d) the second pair, which contains essentially information on the impurity influx phase is displayed. It can be observed that this mode is has a significant weight in the first 10ms following injection.

applies for those particles which are almost non-recycling and for which the depletion phase does not overlap with the influx phase. It becomes useless in those cases when recycling prevents impurities from disappearing after an inflow phase, and for which a longer apparent confinement time τ_{app} is observed. The decay time for the impurity content is given by the

relation $\tau_{app} = \tau_{(R=0)}\dfrac{1}{1-R}$ where R is the recycling factor at the plasma edge and $\tau_{(R=0)}$ is the lifetime which would be observed if the recycling were negligible. In the example of Fig.4.4 the fit was obtained with a time constant equal to $\tau = 21.8\,\text{ms}$.

The common exponential decay time which is observed on many line integrated signals can be explained by means of an analytical model which is common to all transport phenomena of diffusive and convective origin[89]. In the case of sawtooth activity this formulation is restricted to the time interval between consecutive crashes. If for simplicity unidimensional dynamics in cylindrical geometry are considered, equations of the form:

$$\frac{\partial n}{\partial t} = \frac{1}{r}\frac{\partial}{\partial r}\left[r\left(D(r)\frac{\partial n}{\partial r} - v(r)n\right)\right] \tag{4.2}$$

with $n(a, t) = 0$ as boundary condition, have discrete solutions and any evolution can be described through a sum of the form:

$$n(r, t) = \sum_k A_k n_k(r)\exp\left(-\frac{t}{\tau_k}\right) \tag{4.3}$$

in which all the eigenvalues τ_k are positive and the fundamental eigenfunction $n_0(r)$ is non-negative along the whole radius r[89]. The slowest eigenvalue τ_0 can be identified with the impurity confinement time, while the second value τ_1 is a timescale for the relaxation of an arbitrary initial distribution toward the fundamental profile given by $A_0 n_0(r)$. Once this
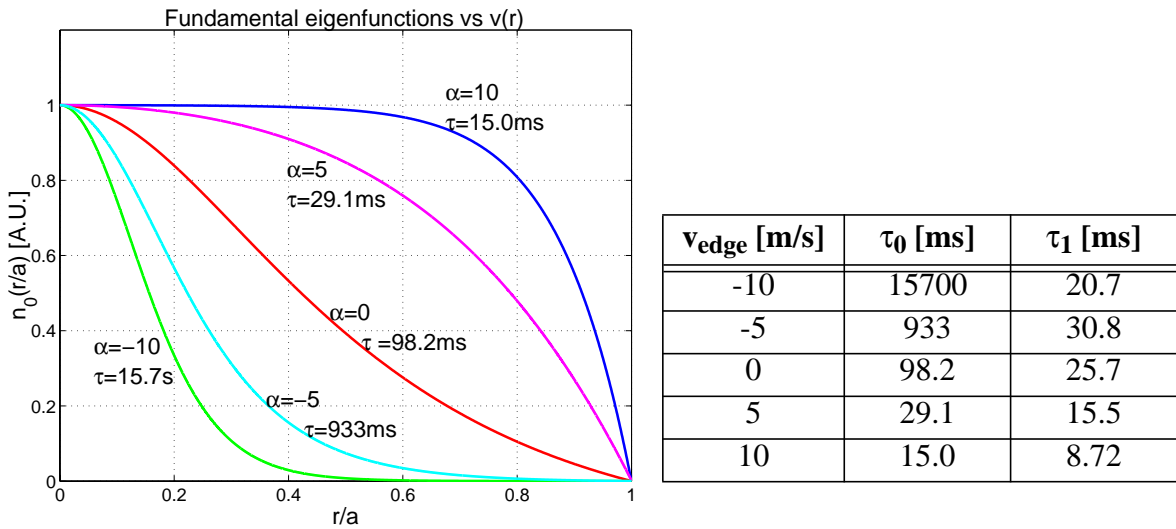

v_{edge} [m/s]	τ_0 [ms]	τ_1 [ms]
-10	15700	20.7
-5	933	30.8
0	98.2	25.7
5	29.1	15.5
10	15.0	8.72

Fig.4.8 - Fundamental eigenfunctions $n_0(r)$ solutions of Eq.(4.2) for a cylindrical plasma, with radius a=0.3m, diffusivity D=0.05+0.25(r/a)^{2}m^2/s, convective velocity v=α(r/a) for different values of α in m/s. The corresponding time constants decrease with increasing outward velocity. In the Table, a comparison between the time constants of the fundamental and the second eigenfunction is reported.

state is reached, the profile keeps its geometrical proportions and consequently the local and the line integrated emissivities decay with the same time constant τ_0 regardless of the position of the measurement. As an example, some fundamental eigenstates of Eq.(4.2), obtained in cylindrical geometry with the same diffusivity profile and different convective velocities are shown in Fig.4.8, together with the corresponding time constants.

The second eigenvalue τ_1 is reported for comparison with the fundamental time constant τ_0 in order to estimate how faster the higher modes decay with respect to the main impurity distribution. While the difference between τ_0 and τ_1 becomes smaller for higher outward edge velocities, there is always at least a factor-of-two between them.

The transient phase after injection, when the line integrated signals reach their maxima, can be characterised by the full width half maximum (*fwhm*, Fig.4.4(b)) which is a timescale related to the formation of the fundamental distribution. Observations from different chords show that the fwhm is almost the same for central and peripheric raw signals, while after GSVD filtering the signals from central chords appear to be broader. This effect is probably produced by the mathematical procedure of GSVD, which produces regularly an anticipation of the rising part, as shown in Fig.4.5.

Many injection signals end with a residual plateau whose height is typically around 4-6% of the peak intensity above the background measured before injection. Even if such impurities are considered to be non recycling, this asymptotic value could prove that a minimum outflux of impurities comes from the vessel walls together with intrinsic impurities like carbon. STRAHL simulations show that the level of recycling usually found in these experiments does not affect the measured impurity confinement times. For example, in shot #21022 it is possible to produce a residual signal in the simulated central lines from 0.5% up to 30% (the measured level is 4.5%) without affecting the confinement time, $\tau_{imp} = 22.1\,\text{ms}$ by more than 0.1ms.

4.1.2 VUV signals and method consistency

The radiation from the plasma edge of injected impurities has been observed in selected shots by means of the SPRED spectrometer, which was used to monitor Si IX to XII spectral lines. Among these ion species, the most internal is the Si^{11+} ion which, as shown in Fig.4.1, is found close to the plasma edge around $\rho=0.9$. Consequently, this measurement is complementary to the SXR detection. In Fig.4.9(a) some spectra are reported from discharge

#21272, two of them recorded at $t = 0.601$ s just before the impurity injection and at $t = 0.726$ s and used as backgrounds for the other, which was obtained at $t = 0.621$ s when the signals from silicon reach their peak value. The spectrometer does not allow the resolution of the Si XI line at $\lambda = 303.3$ A and He II line at $\lambda = 303.8$ A, however the contribution of the latter is constant or varies very slowly with time and thus does not disturb the transient signal from Si^{10+}. In Fig.4.9(b) the time evolution of the integrated signal of Si^{11+} in the interval 497.5-502.9A shows the typical pulse-shaped signal from impurities. The time resolution of the measurement does not allow the detailed reconstruction of the influx phase, as one spectrum has been recorded every 5ms, and SXR measurements show that the signals reach their maximum in a time of the same order. However, the decay of the Si XI line intensity can be accurately resolved, and shows a very good agreement with the soft x-ray signals. The bestfitting value of the time constant of the exponential decaying part of the signal
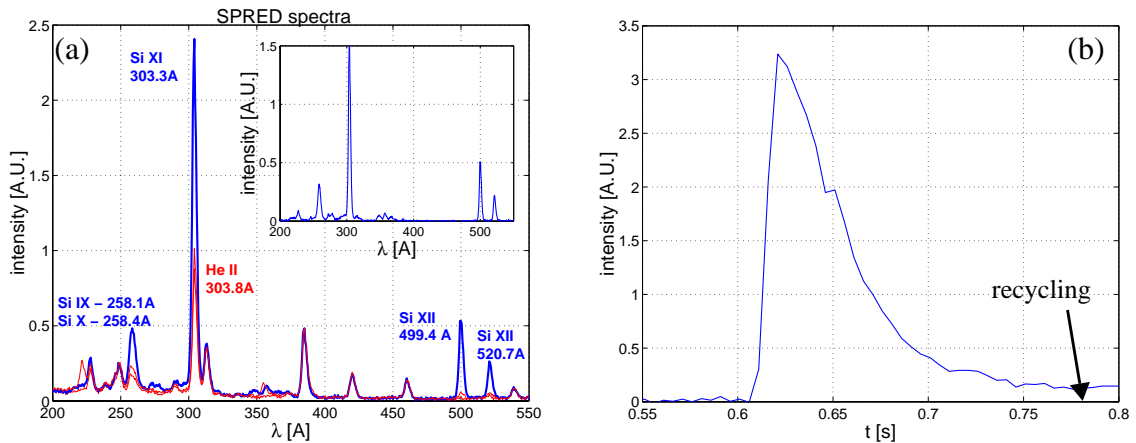
Fig.4.9 - (a) Spectra obtained with the SPRED spectrometer during discharge #21272. The measurements in red have been recorded at t=0.601s, just before the silicon injection and at t=0.726s when the signal of impurities has disappeared. In blue, the spectrum recorded at t=0.621s when the silicon lines are at their maximum. In the inset, the contribution of silicon at t=0.621s is shown. The line at $\lambda = 499.4$ A comes from the Si XII ions which are found around $\rho=0.9$, as shown in Fig.4.1. (b) The time evolution of the intensity of this Si XII line, which shows very similar features and timescales as the soft x-ray signals.

is found to be $\tau_{VUV} = 25.4$ ms which is within the incertitude range of the impurity confinement time, estimated to be, for the shot #21272, $\tau_{imp} = 25 \pm 1$ ms. The time evolution and the exponential decays of all other lines of the spectrum reported in Fig.4.9(a) is very similar, the decay time being close to 25ms.

The line integrated signals from soft x-ray measurements, both from central and mid-radius chords, have shown that the time constant of the exponential decay of the impurity radiation

was fairly independent on the position of the chords. Following these spectroscopic measurements, this result now can be extended to the plasma edge, giving reasonable support to the idea that a fundamental distribution of impurities is reached after a transient phase following injection, and this distribution decays all over the plasma volume with a single time constant. As a consequence, this time constant can be considered a global confinement time for impurities and can be measured via local or line integrated signals, via line spectroscopic systems or broadband detectors.

4.1.3 Impurity effects on TCV plasmas

In the previous Section the radiation from impurities in TCV plasmas has been described, with particular attention to the SXR and VUV contributions of partially stripped ions, coming from all the plasma volume. The introduction of moderate-Z atoms and consequently the additional emission of radiated power can however play a non negligible role in the power balance of the plasma and affect the electron density. Consequently, it is necessary to investigate whether the injected impurities produce perturbations in the target plasmas or simply are tracing particles which do not affect the plasma parameters.

Experimental observations of effects of non-recycling impurity injections on tokamak plasmas have been reported for many experiments. In some cases even small quantities of laser ablated particles have given origin to cold pulses in the electron temperature profiles and to edge localised increases of the electron density[90, 91]. The cold pulse has been observed to propagate towards the centre of plasmas with the same dynamics as the impurities[87] but the reduction in temperature cannot always be accounted for by the increased electromagnetic emission alone. In JET, measurements[48] concerning sudden drops in the electron temperature over a large fraction of the plasmas have been explained with non local changes of the heat transport parameters. In some cases even an increase of the central electron temperature was observed[92, 93] in coincidence with a cooling of the plasma edge.

In TCV the Thomson system (see Section 3.3.2) has spatial and temporal resolutions which do not allow to follow in detail possible cold pulses during the influx of the injected impurities, as no more than one measurement is possible during this phase. However, by means of the data from the soft x-ray system, it is possible to give a quite precise estimation of the concentration of impurity ions in the plasma centre[49] and of the additional emitted power. The basic hypotheses for such estimation are the constancy of the concentration of any in-

trinsic impurity, of the electron temperature and density in the central region of the plasma. This implies as a priori assumption that the injected amount of impurities does not affect the electron density, which can be verified once the absolute amount has been calculated.

In order to evaluate the excess of SXR emissivity in any instant following injection due to the impurities, a tomographic inversion is performed and its distribution before injection subtracted. The impurity concentration can be calculated by means of a simulation with STRAHL, in which the simulated concentration is renormalised in order to match the measured excess of SXR emissivity.

As an example, the injection in shot #21164 has been tomographically inverted and the radial profile of the SXR coming from silicon is compared with the simulation. In Fig.4.10 the two profiles are shown, after renormalisation of the simulated one in correspondence to the maximum value of the line integrated signal on the central chord #30 of the photodiode array, at $t = 0.625$ s. The absolute silicon density and the concentration $f_{Si} = n_{Si}/n_e$ are reported in Fig.4.11. From this example it is evident that in the plasma centre the maximum silicon density is around $n_{Si} = 1.6 \cdot 10^{16}\,\mathrm{m}^{-3}$. The corresponding concentration lies around 0.02-0.03% and hence the perturbation on the electron density is negligible, as the increase in n_e is of the order of 0.3-0.4% which is well below the experimental errors.

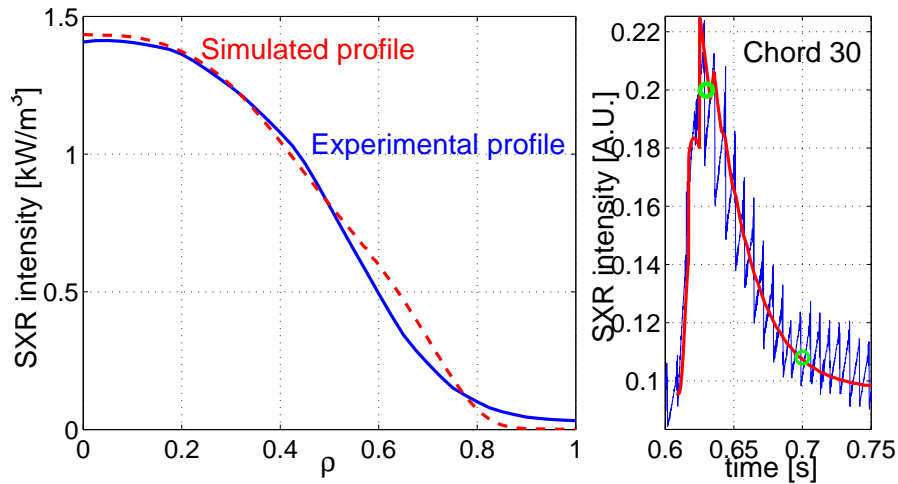The analysis of many injections leads to the observation that the global impurity density is

Fig.4.10 - Comparison between the simulated (dashed line) and experimental (full line) profiles of the SXR emissivity in shot #21164 at $t = 0.63$ s, marked by the upper green circle in the trace of chord 30. For the simulation the transport parameters were $D = 0.05 + 0.35\rho_{pol}^2$ and $v = 4.5\rho_{pol}$. The lower green circle refers to the depleted profile shown in Fig.4.11.

lower in larger plasmas, typically in highly elongated ones. In discharge #19739, for which $\kappa = 2.19$, the central impurity density is found to be 5 times less than the above values.

As far as the total spectrum integrated power is concerned, Fig.4.12 shows that when the SXR signals are at their maxima, the total radiated power from impurities is about the 1% of the total ohmic power, but this fraction is much higher during the impurity source phase, as a large fraction of the injected impurities is concentrated at the plasma edge in a low ionised state. In this example the total emitted power by impurities reaches the 25% of the total ohmic power, and such emission comes almost completely from the region $\rho > 0.9$ and from the ionic species Si II to Si IV. In those cases in which the emissivity from impurities constitutes a non negligible fraction of the total ohmic power, the plasma properties at the edge may be changed by a sudden cooling. However, the edge perturbation is present only during the impurity source phase and may last at most for a time equivalent to the electron energy confinement time, which is of the order of 13-15ms in the analysed discharges. Hence, the exponential decay of the SXR signals and the measured confinement times are unlikely to be affected by an initial perturbation of the plasma edge.

Possible alterations in the plasma properties and in the edge transport dynamics can be in-
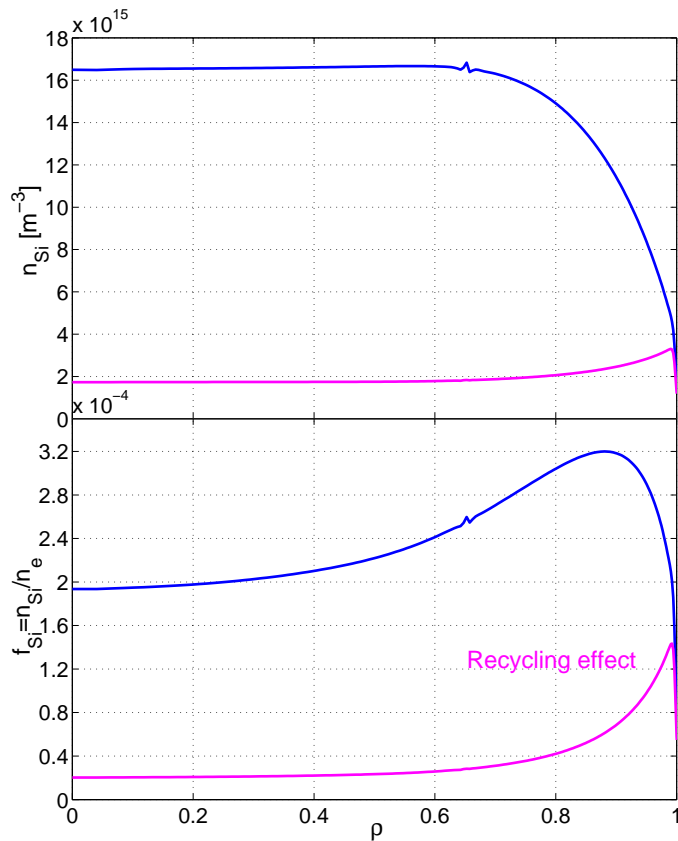

Fig.4.11 - (Top) In blue, the impurity density profile which corresponds to the SXR emissivity profile shown in Fig.4.10, provided by the STRAHL simulation. In magenta, the impurity density during the last phase of the depletion. The central part appears flattened by the sawtooth activity. (Bottom) The corresponding silicon concentrations f_{Si}, when the signal on chord 30 of the tomography system is around its maximum, at $t = 0.63\,s$ and at $t = 0.70\,s$.

spected considering differences in the signal risetimes of peripheric and central chords in cases with different peak ratios of edge radiated to ohmic power. In Table 4.1 some selected shots are reported, in which the above ratio is either around its maximum or minimum value in all performed injections. While there can be differences of a few ms among the different risetimes (the time necessary for the line integrated signal to go from 20% to 80% of the peak value), there appears to be no correlation with the power ratios. Only in one case (shot #19782), which is part of the triangularity scan with $\delta_{LCFS} = 0.05$, shown in Section 4.2.1, the risetime of the central chord is abnormally high. Evidence of a cold pulse preceding the impurity influx has never been observed. Such a pulse would manifest itself by a drop of the SXR emissivity before the rise due to the injected silicon.

In conclusion, no perturbation of the plasma by the impurity electromagnetic emission from impurities has been found.
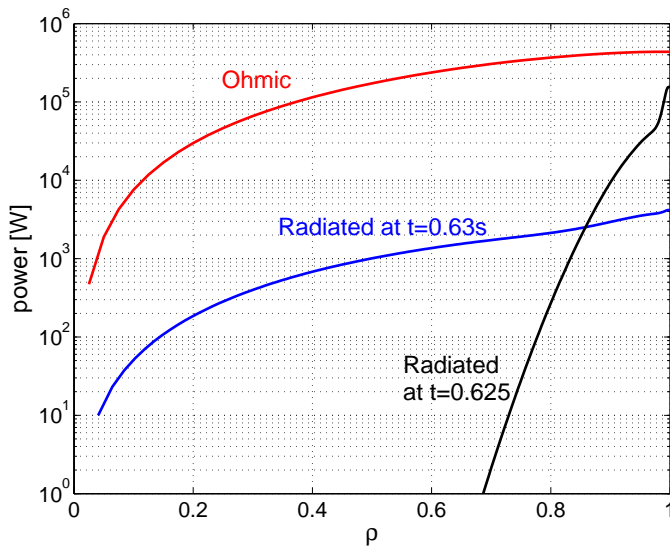

Fig.4.12 - The ohmic power (red), the power emitted by impurities at the SXR signal maxima at t=0.63s (blue) and during the source phase (black) integrated on the plasma volume (shot #21164) inside a given ρ. Data have been obtained by STRAHL simulation.

Shot #	Peak P_{rad}/P_{ohm}	Peripheric chord risetime	Central chord risetime
19785	5%	6.8ms	6.9ms
19739	5%	4.5ms	4.8ms
17788	5%	4.5ms	3.7ms
19631	5%	3.3ms	3.3ms
17799	22%	3.1ms	3.1ms
21022	25%	4.5ms	4.5ms
19782	35%	5.3ms	11.6ms

Table 4.1: SXR signal risetime behaviour versus the peak value in the impurity emission. The particularly long central chord risetime in shot #19782 (δ scan at δ=0.05, Fig.4.14) is correlated to the long impurity confinement time and the low edge convective velocity.

4.2 Experimental observations on the effects of plasma shape

A dataset of about 150 successful impurity injections has been created for the realisation of this work. The number of dedicated discharges in which the impurity signals and the background were clear enough to evaluate the temporal evolution of the SXR emissivity however does not exceed 100. Nearly all the discharges which are taken into account in the following are ohmically heated, limiter plasmas in L-mode confinement. Exceptions are two series in diverted configurations: a density scan which was compared to an equivalent sequence in limiter plasmas, and a scan in which the plasma was a varying mixture of deuterium and helium. For each discharge, the confinement time of the injected impurities was evaluated by means of the expression given in Eq.(4.1). The fit was performed in all cases on the line integrated signals both from central chords and on peripheric chords of the SXR tomography system, and no correlation was found between the time constants of the exponential decays of the signals and the position of the viewchords relative to the plasma centre. The bestfitting
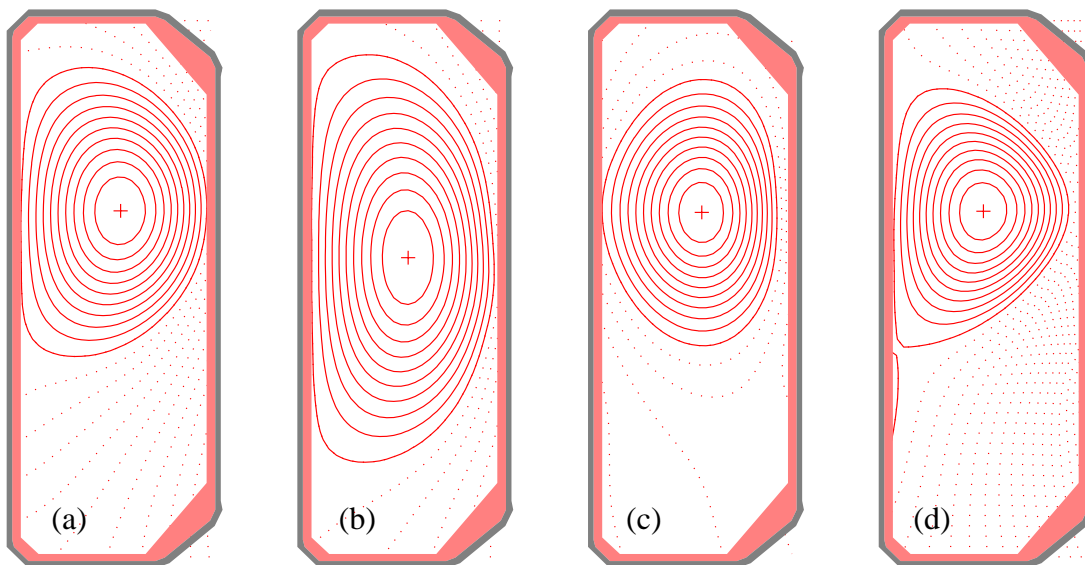
Fig.4.13 - Examples of plasma cross sections in which impurity injections were performed. (a) Minimum elongation, $\kappa = 1.59$ (b) Maximum elongation, $\kappa = 2.28$. (c) Minimum triangularity, $\delta = -0.16$ (d) Maximum triangularity, $\delta = 0.64$

parameters, including the decay time, are determined by means of a fit on a time interval which is not defined a priori, and an uncertainty on the decay time of the order of 1ms can originate from different extensions of the fit interval. Another source of uncertainty is the residual noise of the signals which cannot be removed by means of the GSVD, as this tech-

nique only takes into account regular events like sawteeth. The error bars on the confinement times, shown in the following, have been determined from the set of different bestfitting values coming from the fit of the signals -both raw and filtered from sawtoothing background- from various chords and with different fitting intervals.

The materials chosen for these experiments were non recycling impurities. Most of the injections were made with silicon, while a scan of elongation was performed with aluminum. The dataset, while being quite small and susceptible of completion, is representative of the variety of plasmas which can be produced in TCV and explores ranges of geometrical parameters which can only be obtained in this machine. In Fig.4.13 some examples of plasma cross sections which have been produced in dedicated shots are presented. The elongation scan covers the range $\kappa = 1.59$ to $\kappa = 2.28$, the triangularity goes from $\delta = -0.16$ to $\delta = 0.64$. Besides the forementioned series, in Section 4.2.1 the results of a scan of toroidal magnetic field are presented, while scans of plasma current and line integrated electron density are shown in Section 4.2.2. Other injections were performed parasitically in many discharges, including ECRH and ECCD plasmas, and the results of spare shots are presented in Section 4.2.4.

4.2.1 Triangularity, elongation, magnetic field

It has been presented in Chapter 1 that the triangularity has a strong effect on the electron energy confinement time τ_{Ee}, the reduction of δ to negative values leading to improved confinement of the energy[12, 13]. The distortion of the peripheric magnetic surfaces, deriving from the particular plasma geometry has been invoked as a possible explanation for the improved confinement, and the shape enhancement factor has been introduced as a correction factor (see Section 1.4.2). As a consequence of this geometry, the injected impurities are expected to behave the same way, and increase their confinement time accordingly, when the triangularity of the plasma is lowered and eventually becomes negative.

The triangularity scan has been performed on 13 non consecutive discharges, and some configuration were repeated twice in order to control the repeatability of the results. In these cases, the observed impurity confinement time was reproducible within 1-2ms. The scan spans the triangularity in the interval $\delta = -0.16$ to $\delta = 0.64$, while the other plasma parameters are kept as constant as possible. The elongation was $\kappa = 1.52 \div 1.63$, the line averaged electron density along the Thomson chord $\bar{n}_e = 5.6 \div 6.9 \cdot 10^{19} \, \mathrm{m}^{-3}$, the plasma current

$I = 320 \div 380 \, \text{kA}$ and the toroidal magnetic field $B_T = 1.47 \, \text{T}$.

The effect of triangularity on the impurity confinement time is shown in Fig.4.14(a). For values larger than a threshold around $\delta = 0.2$, there is no effect of the plasma triangularity and the impurity confinement time is around $\tau_{imp} = 25 \, \text{ms}$. From this scan, as well as from scans of other parameters, shown in the following, the plateau at $\tau_{imp} = 22 \div 25 \, \text{ms}$ appears to be a kind of typical value for many different discharge configurations. For $\delta < 0.2$, the impurity confinement time increases to much higher values with a similar scaling to that of the elec-
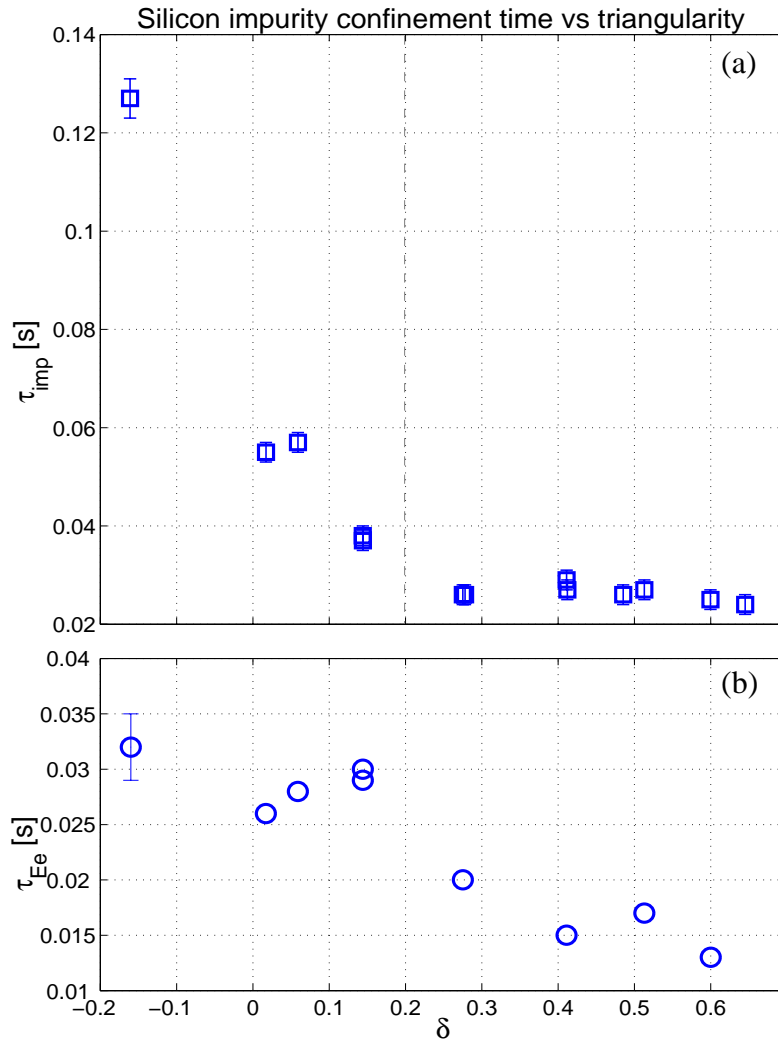

Fig.4.14 - (a) Confinement time of injected impurities for different plasma triangularities. A threshold appears in the triangularity around δ=0.2, below which the confinement time starts increasing. (b) For some of the discharges the electron energy confinement times were calculated according to Eq.(1.21). Their behaviour is in agreement with the results of Ref.[12, 13]. For the evaluation of the point at δ=-0.16 no direct measurement was available. The Neo-Alcator-TCV scaling law[14], Eq.(1.22) was used, with the H_S values which are presented in Ref.[13].

tron energy confinement time for the same discharges. Except for the lowest triangularity, the geometry of the magnetic surfaces alone, described by means of the shape enhancement factor, may account for this behaviour. A slightly higher recycling has been found in the triangularity scan for low values of δ, which could contribute to an increase of the apparent confinement time. The residual line integrated signals are 8% of the peak value at $\delta = 0.28$ and 14% at $\delta = 0.06$; the different recycling level will have to be taken into account in STRAHL simulations in order to rule out possible effects.

At the lower end of the scan, it is found that $\tau_{imp} = 127 \pm 3$ ms which corresponds to an increase of a factor of 5 with respect to the almost constant value found for $\delta > 0.2$. However, this observation at negative triangularity needs confirmation from further measurements in similar plasma conditions as it is based on a single point. The values of the electron energy confinement time, which have been calculated according to Eq.(1.21), are shown in Fig.4.14(b). In agreement with the observation reported in Ref.[12, 13], τ_{Ee} is increased while reducing the triangularity, and its values range from $\tau_{Ee} = 13$ ms for $\delta = 0.6$ to
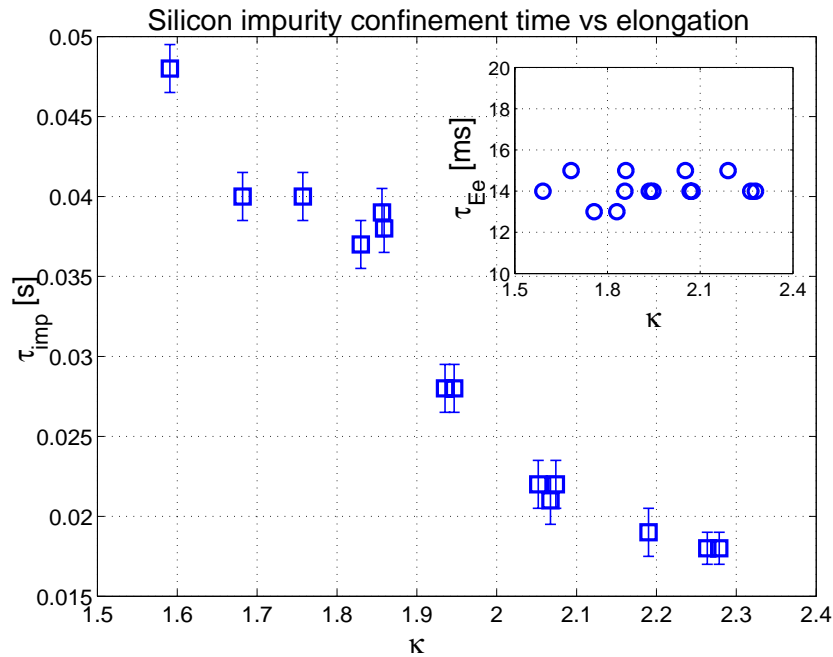

Fig.4.15 - Confinement times of the injected Si impurities for different plasma elongations. In this scan the current was varied accordingly in order to keep the sawtooth inversion radius constant at $\rho_{inv} = 0.55$. τ_{imp} is uniformly decreasing with elongation. In the inset, the electron energy confinement time for the same discharges is shown, and no correlation with elongation is observed, since τ_{Ee} is constant around 14ms.

$\tau_{Ee} = 26\,\text{ms}$ for $\delta = 0.01$. Although the behaviour is slightly different along the scan of triangularity, both the impurity and the electron energy confinement times are doubled at low triangularity and their ratio τ_{imp}/τ_{Ee} is almost constant around a factor of 2.

The investigation of the effects of the plasma shape on the transport of impurities was completed by means of a scan of elongation in the range $\kappa = 1.59 \div 2.28$. Parasitic injections have been performed at even higher elongations around $\kappa = 2.35$ and, while they have not been included in the scan due to a difference in the electron density, their confinement times are in agreement with the following results.

Previous observations in TCV on the confinement of the electron energy[12, 13, 15] show that the confinement is improved with elongation, and the increased values of τ_{Ee} can be related to the increased distance of the peripheric magnetic surfaces. These geometrical effects, which are taken into account in the shape enhancement factor, fully explained the effects of elongation on the confinement of the electron energy.
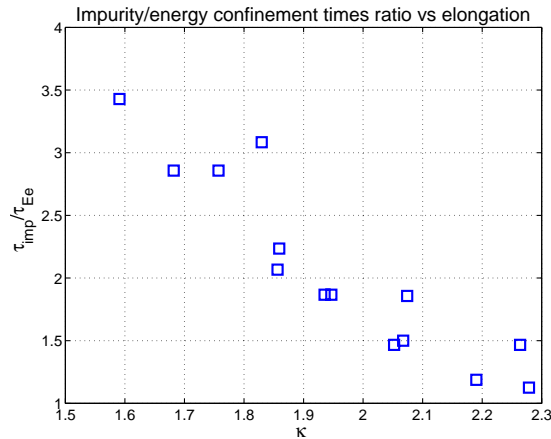

Fig.4.16 - The ratio τ_{imp}/τ_{Ee} for the elongation scan.

The elongation scan has been performed in 2 series of consecutive discharges, consisting of a total of 14 impurity injections. Among the other plasma parameters, some have been kept constant: the triangularity was $\delta = 0.3 \div 0.4$, the line averaged electron density $\bar{n}_e = 5.6 \div 6.9 \cdot 10^{19}\,\text{m}^{-3}$, the toroidal magnetic field was kept at the value of $B_T = 0.92\,\text{T}$. The low values of B_T and I_P reduce the risk of damage in case of disruption at high elongations. The plasma current has been varied proportionally to the elongation, such as to keep approximately constant the "engineering safety factor" $q_{eng}^{-1} \propto I_P/(B_T\kappa)$. This parameter being roughly inversely proportional to the normalised sawtooth inversion radius, the possible dependence of the impurity confinement on the extension of sawteeth were removed. The inversion radius was calculated to be, for all shots of the elongation scan, at $\rho_{inv} = 0.55$, following the scaling laws reported in Ref.[22].

The confinement times of impurities with different plasma elongations are shown in Fig. 4.15. The dependence of τ_{imp} on elongation is surprisingly different from the case of the

electron energy, decreasing with elongation from relatively high values around $\tau_{imp} = 48\,\text{ms}$ for $\kappa = 1.59$ to $\tau_{imp} = 18\,\text{ms}$ for $\kappa = 2.28$. If τ_{imp} followed the shape enhancement factor, it would be expected to moderately increase by about 20% along the scan. The plasma elongation appears to be the geometric parameter which provides the largest difference in the behaviour of impurities and electron energy. The electron energy confinement time was calculated for the shots of this scan, and the ratio τ_{imp}/τ_{Ee} represented in Fig.4.16. The value of τ_{Ee} is fairly constant along the scan, around $\tau_{Ee} = 13 \div 15\,\text{ms}$, and the lack of dependence on elongation is explained by the simultaneous variation of plasma current. As
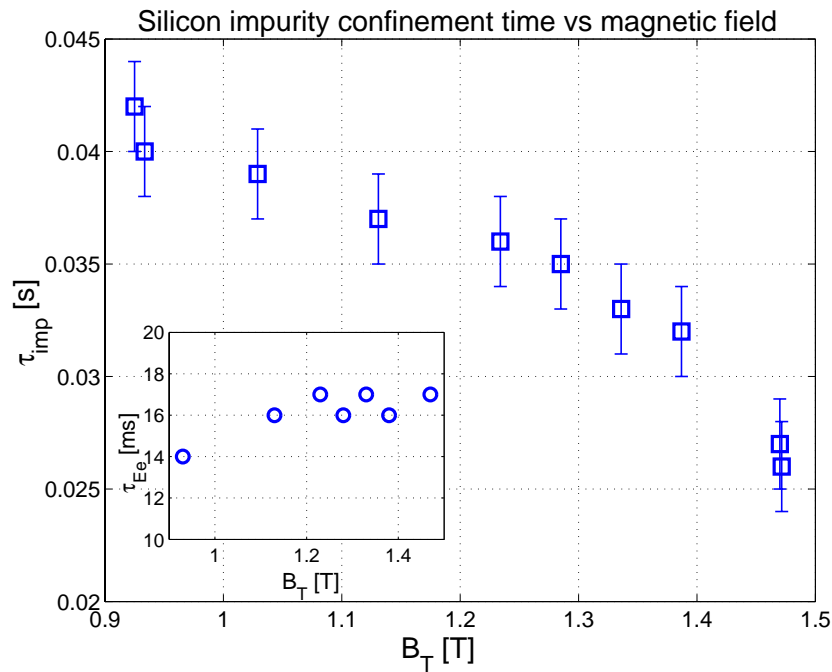

Fig.4.17 - Dependence of the impurity confinement time on the toroidal magnetic field. In the inset, the electron energy confinement time for selected shots in the same scan.

a consequence, the ratio of the confinement times follows the same behaviour as the impurity confinement time alone.

This effect of elongation can be important in the frame of a working reactor in which the impurity level has to be kept as low as possible. Higher plasma elongations could improve the confinement of heat against impurities and lead to a cleaner plasma and lower loss of power coming from impurity radiation.

It has to be remarked that the plasma geometry, density and current at lower elongations are very similar to those of some discharges included in the triangularity scan, but the confine-

ment times are different of a factor of 2. While the profiles of the electron density and temperature in similar shots are comparable within the approximation of 10%, the toroidal magnetic field is the only really different parameter in similar plasmas coming from the triangularity and the elongation scans. However, the influence of the magnetic field appears to favour the confinement of impurities at lower values of B_T, in apparent opposition to the common sense.

The confirmation of the surprising result for which τ_{imp} decreases with B_T has been obtained from a dedicated scan, which includes at its extremities two discharges already belonging to the triangularity scan (shot #19779, $B_T = 1.47\,\text{T}$) and to the elongation scan (shot #19743, $B_T = 0.92\,\text{T}$). The constant parameters were $\bar{n}_e = 5.4 \div 6.4 \cdot 10^{19}\,\text{m}^{-3}$, $\delta = 0.28 \div 0.32$, $\kappa = 1.62 \div 1.70$ and $I = 353 \div 356\,\text{kA}$ and as a consequence of the constancy of the plasma current the sawtooth inversion radius changed according to the toroidal magnetic field. The results of this scan, shown in Fig.4.17, lead to the observation that the increasing magnetic field at constant current produces a regular decrease of the impurity confinement time. In addition, the higher impurity confinement times at low field are associated with a possible higher transport in the plasma core, the sawteeth being more frequent ($\nu_{ST} = 190\,\text{Hz}$ vs ($\nu_{ST} = 140\,\text{Hz}$) and the inversion radius wider ($\rho_{vol} = 0.58$ vs $\rho_{vol} = 0.42$) at low field.

For the same series of discharges, the electron energy confinement time has been calculated and appears to be fairly independent on the toroidal magnetic field at least for the values investigated in this scan, as it ranges from $\tau_{Ee} = 14\,\text{ms}$ for $B_T = 0.92\,\text{T}$ to $\tau_{Ee} = 17\,\text{ms}$ for $B_T = 1.47\,\text{T}$. Similar results on the independence of the magnetic field on the energy confinement time were found in Alcator-A[94], where no clear connection was observed between τ_{Ee} and B_T in the range $6 \leq B_T \leq 9.5\,\text{T}$.

4.2.2 Electron density, plasma current

The effects of electron density and plasma current on the confinement of impurities and electron energy have been investigated in different tokamaks in the past[16, 45, 46, 94, 95]. As a general result, none of the two parameters shows a strong effect on the lifetime of impurities. While in the TEXT tokamak the dependence seems to be almost negligible[45], a slight increase of the impurity confinement time as a function of the plasma current was observed in Alcator-A[94] and a more pronounced effect was found in Alcator-C[95]. A scaling law

for these tokamaks has been proposed, including the dependence on the safety factor as $\tau_{imp} \propto 1/q_a$.

The scan of electron density has been performed both in limiter and in diverted configurations. The elongation $\kappa = 1.57 \div 1.65$ is the same for both series, while the triangularities and the plasma currents were different: $I_P = 355 \pm 1\,\text{kA}$ and $\delta = 0.24 \div 0.28$ in the case of limiter plasmas, $I_P = 274 \pm 1\,\text{kA}$ and $\delta = 0.50 \div 0.52$ for the diverted configuration. These differences however can be neglected if the validity of the results of the scan of plasma current, shown in the following, are assumed, and the impurity lifetime can be considered
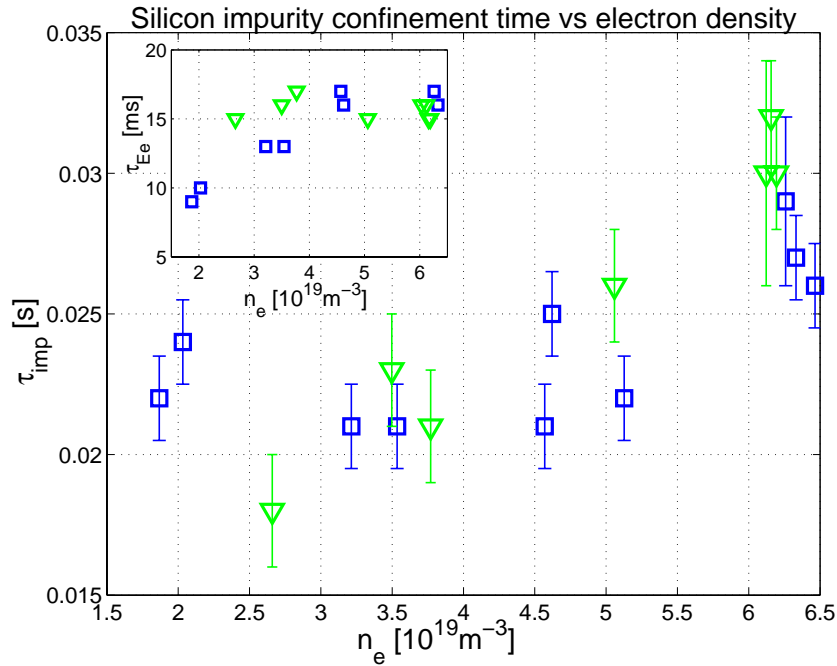
Fig.4.18 - Confinement time of the injected impurities as function of the line averaged electron density. In blue the results of a scan in limiter configuration are reported, while the green points refer to a scan in diverted configuration. In the inset the corresponding electron energy confinement times are shown.

unaffected by the triangularity and the plasma current above the observed thresholds.

In Fig4.18 the results of the scans in both configurations are presented. Injections in limiter plasmas in particular show that the impurity confinement time is little affected by the electron density, since its values are constant around $\tau_{imp} \approx 23\,\text{ms}$ and start increasing towards $\tau_{imp} \approx 27\,\text{ms}$ only when the line averaged density is higher than $\bar{n}_e = 5.5 \cdot 10^{19}\,\text{m}^{-3}$. In the scan in diverted configuration the impurity confinement time shows a possible higher dependence on $\bar{n}_e$, even if this observation has to be completed with additional points at low

density. In this case, the values of τ_{imp} are approximately the same as for the scan on limiter plasmas, but they are likely to fall below $\tau_{imp} = 20\,\text{ms}$ for $\bar{n}_e < 3 \cdot 10^{19}\,\text{m}^{-3}$ and show a linear dependence on the electron density. For the same discharges, the electron energy confinement times τ_{Ee} are fairly constant, around $\tau_{Ee} = 15 \pm 2\,\text{ms}$, without evidence of a correlation with the electron density.

The results of the scan of plasma current in TCV are shown in Fig.4.19. The scan was performed with elongation $\kappa = 1.54 \div 1.64$, triangularity $\delta = 0.26 \div 0.30$ and line averaged electron density $\bar{n}_e = 3.7 \div 4.3 \cdot 10^{19}\,\text{m}^{-3}$. Since this parameter is lower than that of the scans of elongation, triangularity and magnetic field, the possible dependence of the impurity
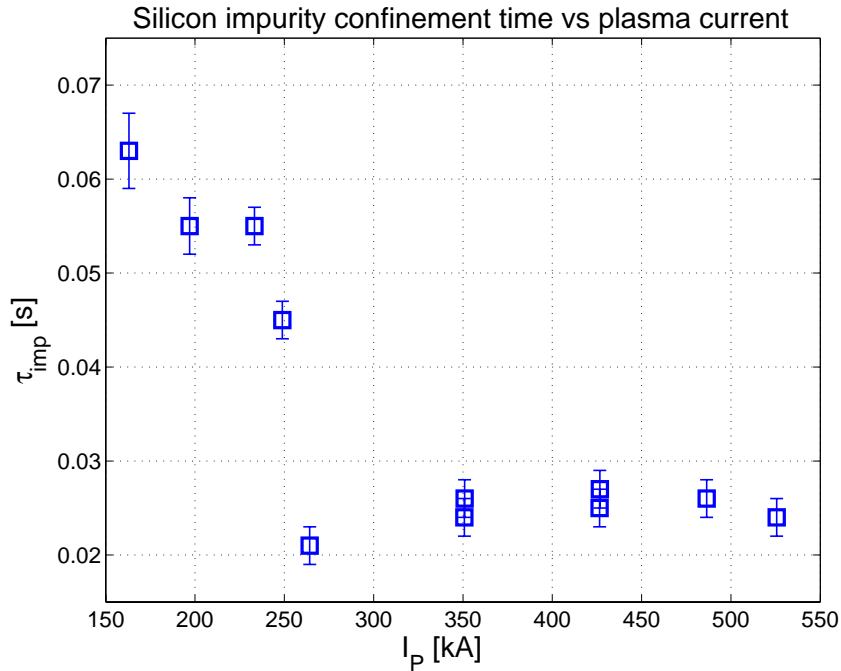

Fig.4.19 - *Confinement time of injected impurities for different plasma currents. A sharp threshold appears for $I_P \approx 250\,kA$, above which the impurity lifetime is little sensitive to the plasma current, and consequently to the values of q_{95} and ρ_{inv}.*

confinement time will have to be investigated with a dedicated scan.

The change of the plasma current in the range $I = 163 \div 525\,\text{kA}$ is associated to a variation of the safety factor from $q_{95} = 6.4$ to $q_{95} = 2.2$ and of the sawtooth inversion radius from $\rho_{inv} = 0.20$ to $\rho_{inv} = 0.55$, since the geometry and the toroidal magnetic field of all discharges are constant. Agreement with the observations on other tokamaks is seen between 250kA and 430kA where the impurity lifetime shows a slight increase with the current. The

experimental values of τ_{imp} are around the value of 25ms which is commonly found for a wide range of parameters. Below 250kA the impurity lifetime increases to rather high values above 50ms.

Unfortunately for the scan of plasma current it was not possible to evaluate the confinement time for the electron energy, because of the lack of Thomson measurements of the profiles of the electron temperature and density. However, it can be assumed again that the Neo-Alcator-TCV law[18] is applicable to this scan, although it refers to the total energy rather that to the electron energy only. As all other parameters which enter Eq.(1.22) are fairly constant all along the current scan, consequently the electron energy confinement time should decrease with increasing current.

Although there is a factor-of-two reduction in τ_{imp} with I_P over the range of the scan, the detailed behaviour, especially the threshold, cannot be related to the behaviour of τ_{Ee}.

4.2.3 Evidence of impurity accumulation

Injections performed in two plasmas whose currents, $I_P \cong 235\,\mathrm{kA}$, are close to the threshold, reveal impurity accumulation in the plasma centre. The line integrated SXR signals from central chords show no or little decrease of the intensity, while the signal from more peripheric chords decays almost linearly to the background. The long persistence of a peaked profile of impurities agrees with a fundamental eigenmode with a very high inward convec-
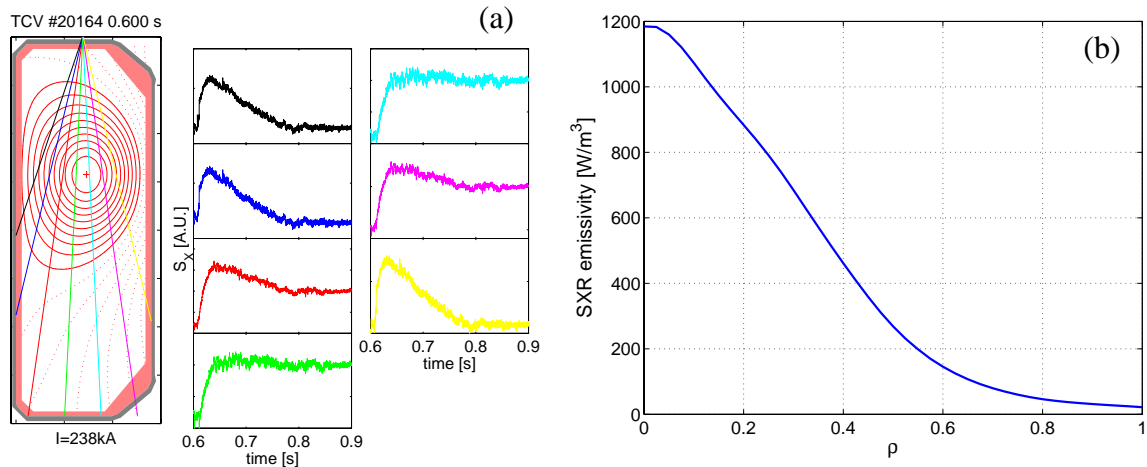

Fig.4.20 - (a) The time evolution of selected line integrated SXR signals in shot #20164. Impurity accumulation in the plasma core is revealed by central chords. (b) The asymptotic profile of the impurity SXR emissivity in shot #20164, measured 200ms after injection. It is taken during the sawtooth buildup phase.

tive velocity and a very high time constant. As shown in Fig.4.8, a possible v_{edge} of around $-5 \div -10\,\text{m/s}$ would lead to a lifetime larger than the duration of the plasma.

The behaviour of this accumulation phenomenon is reported in Fig.4.20(a) for the discharge #20164. The correlation between the position of the chord and the residual asymptotic signal is evident, and no calculation of the confinement time can be done. The plasma centre appears to indefinitely retain the impurities, while the shape of the signal from peripheric chords prevents the possibility of an exponential fit, however the signal *fwhm*, of the order of 80ms, suggests a possible peripheric lifetime in agreement with the low current part of the scan. The configuration was repeated in the discharge #20288 with similar results.

The residual asymptotic profile of the SXR emissivity from the injected impurities is reported in Fig.4.20(b). The profile peaking, together with the very long retention of impurities suggest that the convective velocity is inwardly directed and strong enough to overcome the diffusive flux due to the density gradient. Sawtooth activity is present in these discharges, although the inversion radius and the crash frequency are fairly low compared to other shots in the current scan. The measured values for shot #20164 are $\rho_{inv} = 0.28$, $f_{ST}^{-1} = 7.3\,\text{ms}$ and a reduction of the central SXR intensity of about 12%, which imply a limited transport effect even in the plasma core. It has to be remarked that these values are in no way particular, as they are close to those of the neighbouring discharges which show no impurity accumulation. The comparison of the values of diffusivity and convective velocity in these and the other shots will be made in Chapter 5.

4.2.4 Other observations

No systematic data could be collected in other confinement and heating regimes than the ohmic L-mode. A small number of injections were however performed in ohmic H-modes, in helium discharges, ECRH and ECCD plasmas, and a small scan of elongation was performed with injection of aluminum; these experiments deserve to be reported here for comparison with the above results.

In Table 4.2 the results from some injections in ohmic H-mode discharges with ELMy activity are shown. The values of both the impurity lifetime and the electron energy confinement time are higher than in similar L-mode discharges. Nonetheless, the ratio $\tau_{imp}/\tau_{Ee} \approx 2.8$ is increased as well with respect to the value of 2 or less which is found in the case of equivalent L-mode discharges. No changes in the behaviour of the ELMy activity were observed as a

4.2 Experimental observations on the effects of plasma shape

consequence of the impurity injection.

Shot #	τ_{imp} [ms]	τ_{Ee} [ms]	Common parameters
19592	66	24	$\kappa=1.75$, $\delta=0.58$, $I_P=405kA$, $\bar{n}_e=6.5*10^{19}m^{-3}$
19593	71	26	
19594	67	27	

Table 4.2: Summary of injections performed in ELMy ohmic H-mode discharges.

In Table 4.3 the results of some injections in discharges with additional heating are present-ed. In shots #19556 and #19557 an additional heating is provided by 2 or 3 gyrotrons at the nominal power of 450kW each, plus one more gyrotron in current drive (ECCD) configura-tion, while in shot #19485 there is no current drive. In all cases the impurity lifetime decreas-es to values around 8÷16ms, although not as dramatically as the electron energy confinement time. It has to be remarked that in these discharges the electron density is far lower than that of ohmic shots, so a direct comparison is not possible. These discharges have been performed in L-mode. Auxiliary heated plasmas in both L-mode and H-mode, as well as improved re-gimes with ITBs need further investigation as they are more relevant to reactor regimes.

Shot #	P_{ECRH} [MW]	τ_{imp}[ms]	τ_{Ee} [ms]	Common parameters
19485	1.35	16	3.5	$\kappa=1.60$, $\delta=0.28\div0.50$,
19556	1.35	8	2.5	$I_P=120kA$, $\bar{n}_e=0.9*10^{19}m^{-3}$
19557	1.8	10	1.8	

Table 4.3: Summary of injection in discharges with additional heating

The dependence of the confinement of impurities on the composition of the background plas-ma has been investigated in a series of injections in ohmic L-mode diverted plasma made of mixtures of helium and deuterium. The He-D composition was checked by means of a visible spectrometer which measured the line intensities of the He I at $\lambda = 728$ nm and the D_β at $\lambda = 486.8$ nm.

As shown in Table 4.4, the impurity confinement time correlates with the percentage of he-lium in the plasma. The value of τ_{imp} increases from 29ms in a pure deuterium plasma up to 40ms in a plasma in which the helium percentage is 80%. The impurity confinement time is in agreement with the scan of density, presented in Section 4.2.2, when no helium is present in the mixture. The triangularity in this scan is higher but it is supposed not to significantly affect the observations.

Apart from silicon injections in TCV plasmas, aluminum has been used as trace impurity in a scan of elongation. The other plasma parameters have been kept constant with the exception

Shot #	He%	τ_{imp} [ms]	τ_{Ee} [ms]	Common parameters
22634	0	29	15	
22643	~60	36	18	κ=1.60, δ=0.50, I_P=335kA,
22645	~70	37	19	
22646	~75	38	19	$\bar{n}_e$=7.0*10^{19}m^{-3}
22647	~80	40	-	

Table 4.4: Summary of injections in mixed He-D ohmic L-mode discharges

of the plasma current which varied proportionally to the elongation in the range $I = 330 \div 520\,\text{kA}$. The triangularity was $\delta = 0.4 \div 0.5$, the line averaged electron density $\bar{n}_e = 4.5 \div 5.6 \cdot 10^{19}\,\text{m}^{-3}$, the toroidal magnetic field was kept at the value of $B_T = 1.2\,\text{T}$. The observed confinement times, shown in Fig.4.21, follow the same behaviour as of the injection of silicon, as τ_{imp} decreases with elongation. It has to be remarked however that the absolute values of τ_{imp} are lower in the case of aluminum as they lie in the range $12 \div 17\,\text{ms}$. It is cause of concern that the measured confinement times of aluminum and silicon are different by about a factor of two. Part of the difference can be explained by the values of the toroidal magnetic field. As shown in Fig.4.17, the reduction of the toroidal magnetic field from $B_T = 1.2\,\text{T}$ (scan with aluminum) to $B_T = 0.9\,\text{T}$ (scan with silicon) can account for an increase of τ_{imp} of about 20%. A further effect can be due to the different line averaged electron densities in these scans, which was higher of a 25% in the silicon injections. According to the density scan reported in Fig.4.18, the further correction to the aluminum confinement time might amount to another 25%, bringing the total to at least 50%. Clearly, even after these corrections, the silicon confinement time would still be significantly higher compared to aluminum by a 40% at least.

This discrepancy has been observed in a group of non correlated aluminum injections, all of which show a confinement time whose values are seldom larger than 20ms. About 30 injection were made over a period of three months with $\kappa = 1.28 \div 2$, $\delta = 0.13 \div 0.6$, $I_P = 190 \div 550\,\text{kA}$, $\bar{n}_e = 1.4 \div 6.2 \cdot 10^{19}\,\text{m-3}$, and in all cases $12 < \tau_{imp} < 22\,\text{ms}$. As presented in the previous results, silicon confinement times are typically of the order of 25ms or more, thus clearly higher than those of aluminum.

Some effect, however limited by the fact that aluminum and silicon are close to each other in the Periodic Table, is probably due to the ion charge and mass. This discrepancy needs to be further investigated with simultaneous injections of both aluminum and silicon in order to remove any possible effect deriving from different target plasmas.

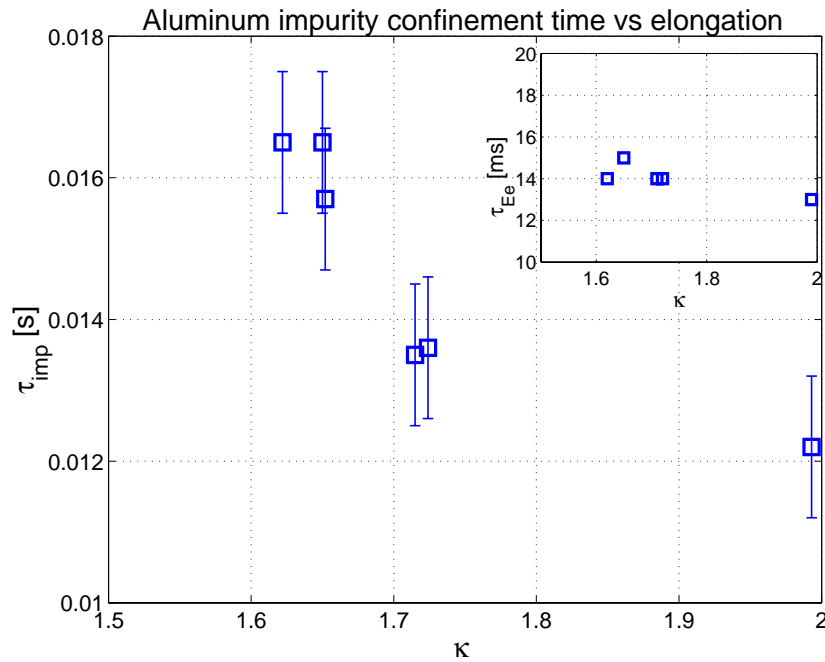All the results which have been presented in this Chapter most probably cannot be extended to elements which are far from silicon in the Periodic Table.

Fig.4.21 - Scan of elongation in which aluminum was injected. In the inset, the corresponding electron energy confinement time is shown.

4.2.5 Sawtooth activity and impurity lifetimes

In all the previous results the dependence of the impurity lifetimes on various plasma parameters has been determined in scans where just one parameter was changed, except in the scan of elongation where the current was varied in order to keep a constant inversion radius. Nevertheless, in each case the sawtooth activity varied accordingly, and the fast transport which is associated can have effects on the global impurity confinement time. Published results[13] show that sawtooth amplitudes decrease when the triangularity is decreased at fixed current and sawtooth inversion radii and amplitudes decrease at lower plasma current. In plasmas with increasing elongation, at fixed inversion radius, the sawtooth frequency increases and the amplitude is reduced and eventually for $\kappa > 2.3$ sawteeth can disappear[15, 22].

During the impurity depletion phase, it is possible that a higher core transport may be associated with a reduced impurity confinement time, and thus high sawtooth inversion radii, frequencies and amplitudes may imply lower values of τ_{imp}. The experimental observations made in the main parameter scans are reported in Table 4.5, in which the behaviour of the sawteeth is compared to that of the experimental τ_{imp}.

Parameter	Value	ρ_{inv}	T_{ST} [ms]	Amplitude	τ_{imp} [ms]
δ_{min}	-0.16	0.39	No ST	0	>100
δ_{max}	0.64	0.50	5.6	20%	23
κ_{min}	1.59	0.58	5.1	26%	48
κ_{max}	2.28	0.58	2.8	11%	18
B_{min} [T]	0.93	0.58	5.1	26%	42
B_{max} [T]	1.47	0.42	7.2	18%	26
I_{min} [kA]	197	0.25	7.4	12%	62
I_{max} [kA]	526	0.55	3.8	18%	24

Table 4.5: Sawtooth properties and impurity confinement times in selected shots

In this Table it is evident that at the low end of the scan of magnetic field large sawteeth, in radial extension and amplitude, are present. Compared to the opposite extreme, also the frequency is higher but nonetheless the impurity confinement time is higher. In the scans of triangularity and plasma current there seems to be a correlation between the sawtooth induced transport and the impurity confinement time. In the scan of elongation at constant inversion radius sawteeth are either small and fast or large and slow, and a remarkable difference in τ_{imp} is found between the extremes. In this case a correlation cannot be established a priori. It is possible that sawteeth do not play a relevant role in the determination of the impurity confinement time, or at least the other transport phenomena, based on the diffusivity and the convective velocity are dominating. The effects of sawteeth alone on the behaviour of impurities can be modelled and reproduced by means of simulation, and the results are presented in Chapter 5.

4.3 Summary and discussion

In this Chapter, the phenomenology of moderate-Z impurity transport in TCV plasmas for various configurations has been presented. The transport of impurities in plasmas has been

characterised by means of their global confinement time, as it is measured from the exponential decay time of the line integrated SXR signals. This procedure is supported by the fact that both the SXR system, which records broadband signals coming from central or more peripheric chords, and the SPRED spectrometer sensitive to VUV radiation from lower ionised states at the plasma edge, show very similar decay times.

Results from TCV plasmas have been obtained in the past on the effects of shape on the confinement of the electron energy. It has been found that both the triangularity and the elongation of plasmas influenced the energy confinement[12, 13], and that such changes could be almost completely explained in terms of the variation of the distance between magnetic surfaces at the plasma edge and its effects on the gradients of the electron temperature and density. The investigation of impurity behaviour in similar discharges has shown that the effect of triangularity, although not identical, is very close to that of energy. For both, the confinement time is increased of a factor of 2 while approaching zero or negative triangularity, the only difference being the presence of a threshold at $\delta = 0.2$ in the case of impurities.

The most surprising results come from the effect of elongation on the impurity confinement time, as a higher elongation leads to lower lifetimes. The behaviour is different from that of the electron energy, which in the scan of elongation was approximately constant. As reported from previous TCV results, the increase of elongation alone produced an increase in the energy confinement time which was very well correlated to the higher plasma size and lower gradients of electron density and temperature at the plasma edge. These measurements seem to indicate that the local transport is increased with elongation for impurities without effect on the energy. As far as the ratio τ_{imp}/τ_{Ee} is concerned, a reduction of a factor of 3 to 4 is determined by simply increasing the plasma elongation from $\kappa = 1.6$ to $\kappa = 2.3$ at constant sawtooth inversion radius.

These results are particularly interesting in view of a future thermonuclear reactor, whose performances are strongly determined by the impurity levels in the plasma. The marked decrease of the impurity confinement time with increasing elongation may help the reduction of impurity concentration and at the same time improve the confinement of the energy. Impurity transport in highly elongated plasmas needs to be further investigated in reactor relevant configurations.

Another unexpected observation comes from the scan of magnetic field, whose increase reduces the confinement time of impurities. The radial motion of impurities appears not to be

directly correlated to the fact that a higher magnetic field leads to smaller orbit sizes and hence to smaller steps in the collisional diffusion process, which is at the basis of the neo-classical theory of transport. On the contrary, the "inverted" effect of the magnetic field is a further suggestion that the contribution of anomalous radial transport or turbulence is dominating.

The scans of line integrated electron density and plasma current show that the impurity confinement time is little affected by this parameter, at least for limiter plasmas and above a sharp current threshold. In plasmas of same sizes and with similar profiles, the constancy of the impurity lifetime is typically a consequence of non varying transport parameters. These observations are in agreement with the results reported from transport investigations in TEXT plasmas[45], following scandium injections, where the diffusivity and the convective velocity show no strong correlation to the plasma current nor to the density. Similar results were obtained in Alcator C-Mod[95] where no scaling with density was found.

A radical change in the impurity confinement time is however observed when the plasma current is sufficiently low. The value of τ_{imp} is increased from the usual 25ms up to 50ms and beyond. Moreover, for plasma currents close to the threshold value, a couple of injections shows central accumulation, in which a peaked radial profile of impurities is formed and lives up to the end of the discharge without an edge source to fuel it. The central SXR intensity is almost constant and does not decrease from its maximum value.

The sawtooth activity has been shown to provide a large contribution to the transport of energy in the plasma core[19], as each crash is associated with fast flattening of the central density and temperature profiles in a time scale of the order of 100μs. The analysis of all the impurity injections in TCV shows however that these sawtooth effects are not dominant on the global lifetime of impurities. In the scans magnetic field, for instance, the longest impurity confinement times are found when the core transport associated to the sawtooth activity is higher if compared to the other discharges in the scan. A possible explanation can refer to the fact that the flat profiles of the impurity density consequent to crashes are little affected by central transport before the following sawtooth takes place, reducing the effectiveness of the sawtooth activity. As a consequence, the evolution of the outflux phase may be dominated by the transport outside the mixing radius. However, the quantitative evaluation has to be made with STRAHL, in which the sawtooth extension and frequency can be artificially changed.

4.3 Summary and discussion

In the frame of a description of the radial transport based on the profiles of diffusivity $D(r)$ and convective velocity $v(r)$, it is probably possible to provide a simple correlation of these values to the features of the experimental signals. By means of simulation codes, like STRAHL, the bestfitting transport parameters can be searched in order to match the observed impurity confinement times. In the lack of a clear physical explanation of the impurity behaviour when these plasma parameters are changed, the profiles of D and v may contribute to the understanding of the transport of impurities at the edge of plasmas. In particular, the bestfitting values of D and v may be compared to the expected neoclassical values.

5. TRANSPORT SIMULATIONS

In Chapter 4 the collection of many impurity injections have been presented for various plasma configurations. As a consequence of the variation of the geometry of the plasma, as well as of physical parameters like plasma current, electron density, different shapes of the soft x-rays line integrated signals were obtained and the impurity confinement time was put in relation with these parameters. However, in order to evaluate locally in the plasma the transport of impurities and give a quantitative estimate of the profiles of the diffusivity and of the convective velocity, it is necessary to extract such values from the experimental data.

A widely used technique consists in calculating the evolution of the concentration of the injected impurities in plasma and derive the electromagnetic emissions which would be measured on the basis of assumed transport parameters. The simulated signals are compared with the experimental ones in order to find the bestfitting set. As a common feature, the plasma background during simulation is assumed not to be perturbed by small amounts of injected impurities.

Examples of this procedure come from many machines and various codes are currently used. 2D and 3D Monte Carlo methods have been implemented for the impurity transport simulations on MT-1M tokamak[96], for ITER predictions[97] and for the edge transport on Alcator C-Mod[98]. The transport of aluminum impurities in TEXTOR[30] has been modelled by means of a code based on the kinetic theory and the results compared to low ionised states of the injected material.

Other codes, like MIST (from Tokamak de Varenne[99]), IONEQ[100] or STRAHL[51], treat the transport of impurities at a low level, in which the profiles of the diffusion coefficient and of the convective velocity are set as free parameters, without assuming their dependencies on plasma features. The STRAHL code has been widely used in simulating experiments on ASDEX Upgrade[37] and on JET, and also offers the possibility to use the neoclassical transport coefficients. The STRAHL code has been used on TCV for the realisation of this thesis, and its features are described in the following.

5.1 The STRAHL code

5.1.1 General features

STRAHL is a 1-D code to calculate in a shaped toroidal geometry the 1D radial transport of impurities and their electromagnetic emissions from the plasma core. Many input parameters are generally taken from real experiments, like the profiles of the electron density, the electron temperature, the geometry of plasma, the sawteeth characteristics like frequency, radial extension and instant of the first sawtooth after the beginning of the impurity influx. The plasma geometry is considered to be fixed during simulation, while the other profiles, like T_e, n_e, can vary and are normally set at given times, which in TCV are taken as the times of the Thomson scattering measurements. The ion temperature is normally set equal to the electron temperature, and it is needed only when neoclassical transport is simulated. The following description of the STRAHL code is extracted from the User Manual by R.Dux[59].

Atomic data are read from files in which all the necessary parameters are stored according to ADAS conventions. Many input files include the electromagnetic emission parameters separately for bremsstrahlung, charge exchange, spectral line emission in total for each ionised species and for selected lines. The spectral sensitivity of the real soft x-ray photodiodes on TCV (shown in Fig.3.6) has been taken into account to allow the calculation of the fraction of emitted power, which can be measured by the system, thus allowing the direct comparison with the real signals. Moreover, in order to take into account the evolution in space and time of each ionised species, the rate coefficients of ionisation, recombination and charge exchange are stored as function of the electron temperature.

The output data files contain all the time and space evolution of the concentration of impurities, in total and for each ionised species, as well as their local total emissivity and the part which can be measured by the soft x-ray system on TCV. The profiles are normally shown as a function of ρ_{pol} which is calculated by STRAHL on the basis of the real geometry of the magnetic field, and it is defined as:

$$\rho_{pol} = \sqrt{\frac{\Psi - \Psi_{axis}}{\Psi_{LCFS} - \Psi_{axis}}} \ . \tag{5.1}$$

If it is specified in the configuration file, the time evolution of selected spectral lines at given wavelength is calculated. Details about the calculations of all the different electromagnetic emissions can be found in Ref.[51] and references therein.

5.1 The STRAHL code

During the execution, STRAHL solves the transport equation (2.36) for each ionised state in a series of discrete time values. The numerical algorithm is based on modified formulas which take into account the geometry of the plasma, as follows.

The law of conservation of the number of particles for each ionised state can be written as:

$$\frac{\partial n_Z}{\partial t} = -\nabla \vec{\Gamma}_Z + Q_Z \tag{5.2}$$

where $\vec{\Gamma}_Z$ is the flux density of the impurities in the ionised state Z and Q_Z is the source/sink term due to ionisation, recombination and charge exchange which connects neighbouring states. Inside the last closed flux surface (LCFS) the impurity density n_Z can be integrated over the volume included in a flux surface of arbitrary label ρ:

$$\frac{\partial}{\partial t} \int n_Z dV = -\oint \vec{\Gamma}_Z d\vec{S} + \int Q_Z dV \tag{5.3}$$

and the surface integral can be transformed with a change of variable to:

$$\oint \vec{\Gamma}_Z d\vec{S} = \oint \vec{\Gamma}_Z \frac{\nabla \rho \, d\vec{S}}{|\nabla \rho|} \tag{5.4}$$

Using the flux surface average[101] defined as:

$$\langle A \rangle = \left(\frac{\partial V}{\partial \rho}\right)^{-1} \oint A \frac{d\vec{S}}{|\nabla \rho|} \tag{5.5}$$

and

$$\int A dV = \int_0^\rho d\rho \frac{\partial V}{\partial \rho} \langle A \rangle \tag{5.6}$$

and differentiating with respect to ρ after substituting into the differential equation, we obtain the continuity equation for the flux surface averages:

$$\frac{\partial \langle n_Z \rangle}{\partial t} = -\left(\frac{\partial V}{\partial \rho}\right)^{-1} \frac{\partial}{\partial \rho}\left(\frac{\partial V}{\partial \rho} \vec{\Gamma}_Z \nabla \rho\right) + \langle Q_Z \rangle \tag{5.7}$$

It is also assumed that the impurity density and the sink/source terms are constant on the flux surfaces. For the flux term the ansatz of a diffusive and a convective part is used:

$$\vec{\Gamma}_Z = -D\nabla n_Z + \vec{v} n_Z \tag{5.8}$$

In this case we have:

$$\vec{\Gamma}_Z \nabla \rho = -D|\nabla \rho|^2 \frac{\partial n_Z}{\partial \rho} + v|\nabla \rho| n_Z \tag{5.9}$$

in which for simplicity D and v refer only to the radial components of the diffusivity and the convective velocity. The final expression of the transport equation can be simplified with the introduction of the specific surface flux label:

$$\rho_{vol} = \sqrt{\frac{V}{2\pi^2 R_0}} \qquad (5.10)$$

which leads to the equation:

$$\frac{\partial n_Z}{\partial t} = \frac{1}{\rho_{vol}}\frac{\partial}{\partial \rho_{vol}}\rho_{vol}\left(D^*\frac{\partial n_Z}{\partial \rho_{vol}} - v^*n_Z\right) + Q_Z \qquad (5.11)$$

where $D^* = \langle D|\nabla\rho_{vol}|^2\rangle$ and $v^* = \langle v|\nabla\rho_{vol}|\rangle$. It is assumed in the code that these parameters are the same for all the ionised species of the considered element.

The numerical algorithm solves the spatial part of the equation by means of the time-centred Crank-Nicholson scheme. In each spatial point of the mesh the density at the following time point is calculated from the densities at the old time point in the surrounding space points, via the implicit equation:

$$\frac{n_s^{t+1} - n_s^t}{\Delta t} = \frac{D}{2}\left[\frac{(n_{s+1}^t - 2n_s^t + n_{s-1}^t) + (n_{s+1}^{t+1} - 2n_s^{t+1} + n_{s-1}^{t+1})}{(\Delta x)^2}\right] \qquad (5.12)$$

in which the index t refers to the time steps, and s refers to the spatial mesh point.

The code solves alternatively in ascending and descending order the contributions of the source/sink terms included in Q_Z which are evaluated in mid points of the time steps.

On the most external radial point the code takes into account the external source of neutral impurities, which has to be provided as an input parameter. The code calculates the number of neutrals per time step once the total number of particles and the time evolution of the source are known.

The code takes into account the effect of sawteeth, which are modelled as a sudden flattening of the concentrations all the ionised species inside the mixing radius, in which the total number of particles is kept constant. The times of the sawtooth crashes, defined in the input files, are included in the series of time points.

The edge of the plasma is modelled with a scrape off layer reservoir, which is external to the LCFS and which exchanges particles with the external source, the walls and a divertor reservoir. Fluxes are modelled with the wall with a recycling coefficient and with the divertor with typical time constants.

For a typical STRAHL run the following data are each time provided to the configuration

file of the code, in addition to the electron density, temperature and to the geometry of the magnetic surfaces which are read from the TCV database:

- the impurity element, typically C, Al or Si;

- the source time evolution. The total intensity is useful only in the case a comparison of the simulated and real signal intensities are to be considered. In the following, the source is assumed constant in time, while its duration, 4ms, is set in agreement with the experimental observations obtained with the OMA spectrometer and presented in Section 3.3.6. The code assumes that the neutrals are uniformly deposited in the scrape-off layer of the plasma;

- the recycling properties from the wall, which are correlated with the level of the residual asymptotic signal after impurity exhaustion from plasma. The code assumes that the impurity fluxes between the scrape-off layer and the wall are proportional to the impurity densities n_{SOL} and n_{Wall} respectively. The two time constants τ_{S-W} and τ_{W-S} relate these densities to the fluxes according to $\Phi_{S-W} = \dfrac{n_{SOL}}{\tau_{S-W}}$ and $\Phi_{W-S} = \dfrac{n_W}{\tau_{W-S}}$. The intensity of the residual signal depends on the ratio τ_{S-W}/τ_{W-S};

- the values of the diffusion coefficient D and convective velocity v, at an arbitrary number of normalised radii ρ_{pol}. These values are usually parametrised as functions of ρ_{pol}, then sampled on given radii and included in the STRAHL configuration files;

- the number of sawteeth and the mixing radius $\bar{r}_{mix} \equiv 1.4 \cdot \bar{r}_{inv}$, as well as all the times in which sawtooth crashes take place. The inversion radius $\bar{r}_{inv}$, when dealing with experimental non circular plasmas, is evaluated as the average geometrical value along the magnetic surface labelled with ρ_{inv}.

Once the code output is provided, it is possible to calculate the simulated line integrated signals along the chords of the soft x-ray signals, or along the VUV SPRED spectrometer chord.

5.1.2 Effect of the transport parameters on signals

One of the most useful properties in the utilisation of a simulation code is the possibility to freely make assumptions on the radial profiles of the diffusivity and convective velocity and calculate signals which are different from the ones measured in experimental plasmas. As a

consequence, it is possible to establish a correlation between the transport coefficients and the time evolution of the calculated signals and to easily converge to the bestfitting coefficients which simulate the experimental results.

In this Section, some examples are given of the effects of the central and edge diffusivity and radial velocity on the shape of the simulated line integrated SXR signals. In the frame of the proposed modelling[51], the role of the sawtooth frequency and radius will be presented and discussed, together with the possibility to use sawteeth to modify the impurity fluxes in the plasma core.

The features of a typical peaked, line integrated real or simulated SXR signal, have been presented in Section 4.1.1. The set of characteristic values which will be considered in the following, and define quantitatively the temporal evolution of the signals, can be varying according to the different viewlines. For simulations on TCV, the geometry of real plasmas and real chords of the SXR tomography system have always been used, with particular attention for the central chords. The following parameters are considered:

- the exponential decay time τ_{imp}, or lifetime, of the tail of the signal;

- the full width half maximum *fwhm*, in which the maximum of the signal is evaluated relatively to the pre-injection level, thus not taking in account the residual asymptotic value;

- the signal risetime *rt*, given here as the time necessary for the signal to rise from 20% to 80% of the peak value;

- the "central flow" *cf* of impurities during the influx phase, which is defined as the normalised increase of the signal between two consecutive sawtooth crashes, according to the expression:

$$cf = \frac{S_x(t_2) - S_x(t_1)}{t_2 - t_1} \frac{2}{S_x(t_2) + S_x(t_1)} \tag{5.13}$$

where S_x is the line integrated SXR signal along a given chord, t_1 is the time of the end of a sawtooth crash and t_2 the beginning of the following crash.

- the level of the asymptotic signal, given as the fraction of the peak value.

In Fig.5.1 the dependencies of the lifetime and the *fwhm* on the edge diffusivity and convective velocity are shown, taking as reference the shot #19785 and a central viewline of the

SXR tomography. The values of D_{edge} and v_{edge} (which is considered positive when outward) are separately scanned around the bestfitting values, which provide the measured values of τ_{imp} and *fwhm*. Both parameters show a similar effect on the global shape of the signal, as an increase of the edge diffusivity or of the edge velocity is reflected in a shorter duration of the signal and a faster exponential decay. On the contrary, the scan of the central diffusivity D_0 shows that its effects are very limited in the duration of the signal and during the depletion phase. This fact can be easily explained as in these simulations the real sawtooth activity has been included, and accounts for the predominant impurity fluxes in the plasma core. The flattening of the impurity distribution due to a sawtooth crash is little modified by particle diffusion, except in the region around the mixing radius. Once the source is switched off, the central impurity profile becomes flat at the first subsequent sawtooth crash and the particle depletion is dominated by the fluxes in the plasma periphery. According to the chosen radial profile of the transport parameters, the values of D and v at the last closed
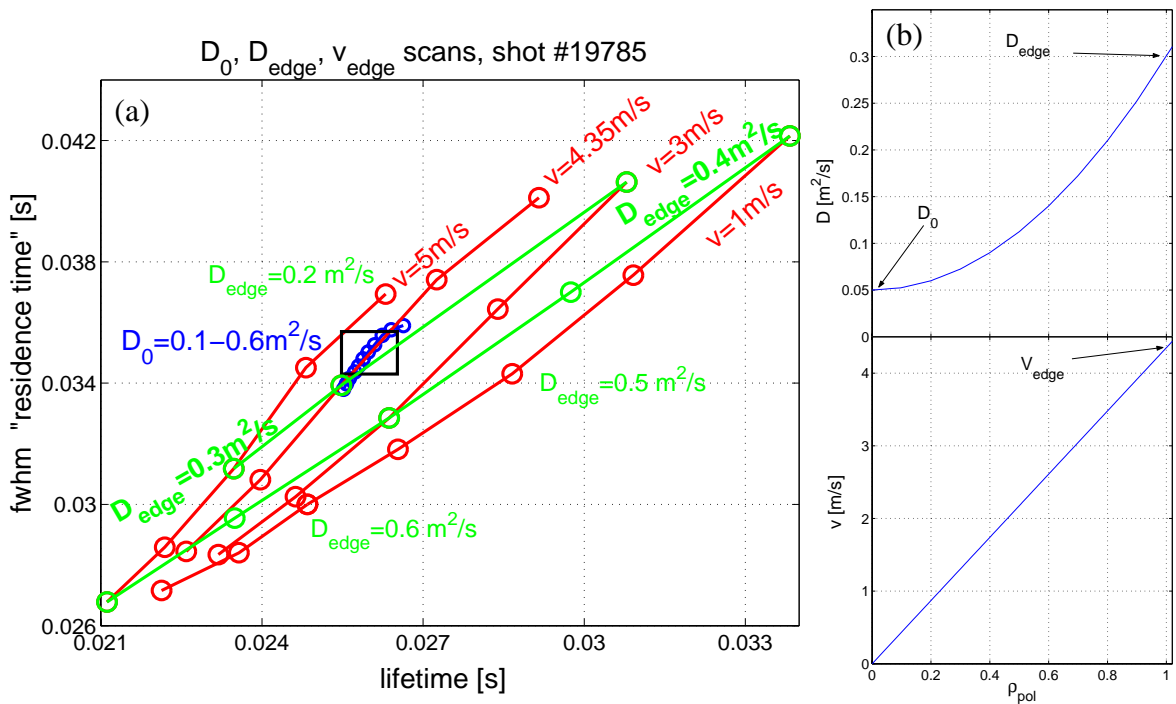
Fig.5.1 - (a) Simulations of the SXR line integrated signal #30, on the plasma discharge #19785. Scans of D_{edge}, v_{edge} and D_0 have been performed and the resulting temporal evolution of the signal, determined by τ_{imp} and fwhm, has been obtained. The black rectangle represents the measured values, fwhm=35ms and τ_{imp}=26ms, with an incertitude of ±2%. The scans of f D_{edge} and v_{edge} have been performed for $D_0 = 0.05\,m^2/s$. (b) The bestfitting values in the assumption of a parabolic profile of $D(\rho)$ and a linear one for $v(\rho)$.

flux surface ($\rho = 1$) may be determined with an uncertainty of up to 10%. However the average values in the region for which $\rho > 0.9$ is fairly well determined. Constant, parabolic and exponential radial profiles have been used for the diffusivity, while linear and parabolic profiles have been considered for the convective velocity, with different central positive and negative slopes.

The values of the transport parameters D_0 and $v'_0 \equiv \dfrac{dv}{d\rho}\Big|_{\rho = 0}$ relative to the plasma core have an important effect on the rising part of the signal, when profiles are hollow. Due to the high inward gradient of the impurity profiles, the central fluxes of impurities can be relevant. The particle transport in this phase is affected by the exact times of sawtooth crashes, which produce sharp steps in the signals from central chords whose height depends on the concentration of impurities entering the mixing radius. According to the radial profile of the impurity density just after injection, early sawteeth are less effective than late ones, as they move a smaller quantity of particles to the plasma centre. In Fig.5.2 the dependencies of the risetime
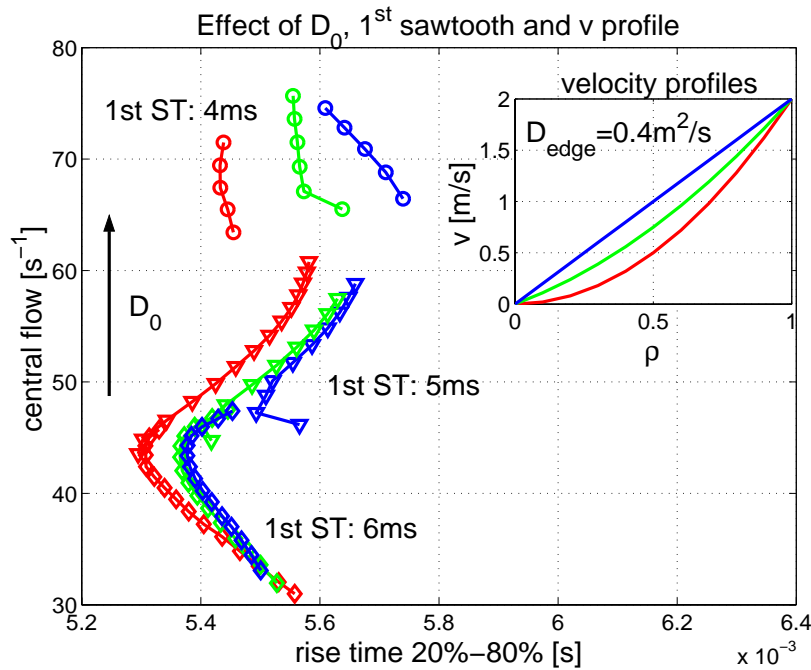
Fig.5.2 - Simulation of the rising part of the central chord #32 in discharge #19743 as a function of the central diffusivity, radial convective velocity and timing of the first sawtooth. For each set of these parameters, the rise time and the central flow after a given sawtooth, defined in Eq.(5.13), have been calculated. The irregular shape of the 20%-80% rise time can be explained by the possibility that such fractions of the peak intensity often lie inside a sawtooth step. The first sawtooth marked at t=6ms is the first relevant one, after a sawtooth crash at t=1ms during which almost no impurity particles were involved. For each line the central diffusivity was scanned in the range $D_0=0.05\div0.6m^2/s$.

and central flow of simulated signals are shown as functions of the values of the central diffusivity D_0 and velocity profiles for different instants of the first sawtooth. The edge values for the transport parameters have been kept constant for all points, which caused only a slight change in the values of τ_{imp} and *fwhm*. The risetime appears to be affected by few tenths of a millisecond only by the variation of the radial profile of the velocity, while the central flow is more sensitive to both D_0 and the delay of the first relevant sawtooth. In the case of shot #19743, reported in Fig.5.2, the sawtooth period is equal to 5.0 ms and no significant influx is found from the simulation if the first relevant sawtooth takes place before 4ms from the impurity injection. However different sawtooth times lead to the selection of different time intervals for the evaluation of the central flow.

The effect of the sawtooth activity alone on the central line integrated signals is shown in Fig.5.3 for the discharge #19785. In the simulation, the mixing radius and the sawtooth frequency have been changed with respect to the experimental values, $\bar{r}_{mix} = 17.3$ cm and $1/f_{ST} = 6$ ms, while the radial profiles of the transport parameters have been kept constant, and the shapes of the signals have been compared. Although the timing of the sawteeth may
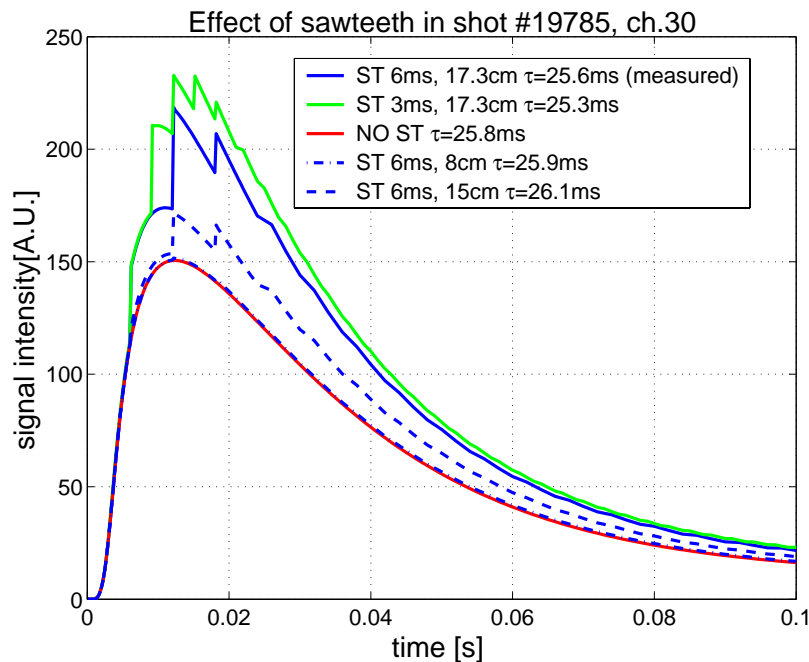
Fig.5.3 - Simulation of the effect of the sawtooth activity, characterised by the period and the mixing radius, on the global shape of line integrated SXR signals, in shot #19785, chord #30. The profiles of the transport parameters are parametrised as $D(\rho) = 0.05 + 0.24\rho^2 \, m^2/s$ and $v(\rho) = 4.35\rho \, m/s$ (outward) which allow the correct reproduction of the experimental signal, as shown in Fig.5.1.

slightly vary the influx phase, all signals are characterised by very similar lifetimes for different frequencies or mixing radii. In the depletion phase, the impurity outflux depends almost completely on the transport coefficients in the plasma periphery and sawteeth contribute only to little transport from the plasma core to the mixing radius, as previous crashes already flattened the impurity profile.

Sawteeth affect the accumulation of impurities to the centre until profiles are hollow, with a larger contribution in the case of higher frequencies and larger mixing radii. The main differences between simulated signals are observed around their maxima, as sawtooth activity increases the total amount of impurities reaching the plasma core. It can be remarked that very small mixing radii are ineffective for the global transport of particles, as the signal obtained with $\bar{r}_{mix} = 8\,cm$ (Fig.5.3) is almost identical to the case in which sawtooth activity was turned off.

5.1.3 Search for the bestfitting parameters

All the considerations reported above, while being useful for the understanding of the roles of different phenomena in the transients of impurity transport in plasmas, can be applied in
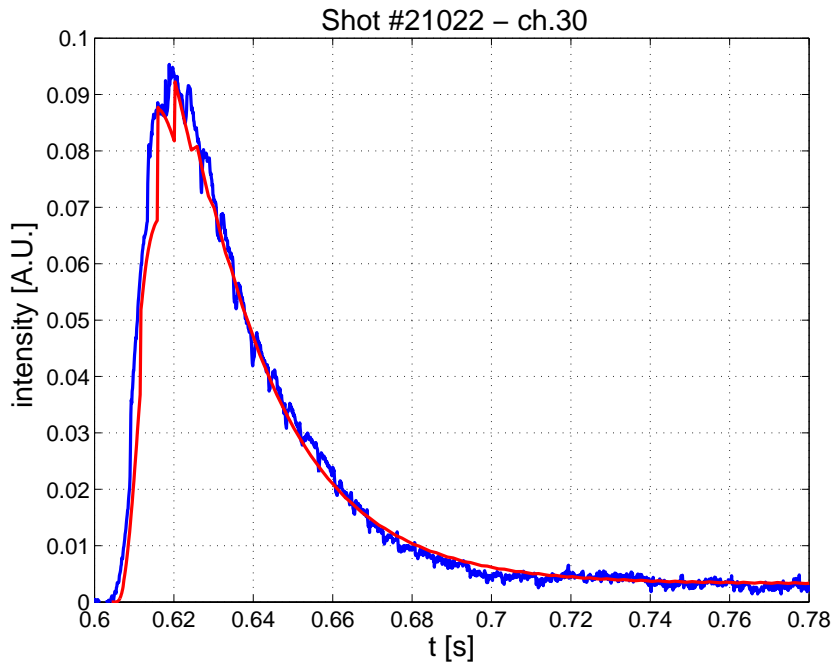
Fig.5.4 - Experimental (blue) and reconstructed (red) line integrated signal from shot #21022, channel 30. The real shape values are $\tau_{imp} = 22.0\,ms$, $fwhm = 30.6\,ms$, $T_{ST} = 4.3\,ms$, $r_{mix} = 14.2\,cm$. The bestfitting parameters are $D = 0.05 + 0.61\rho^2\,m^2/s$, $v = 3.8\rho\,m/s$.

the research of the bestfitting parameters which allow the matching between experimental and simulated signals. The routines which are used for the reproduction of the measured SXR signals from TCV plasmas are based on the almost independent effects of the transport parameters at the edge and in the centre of the plasma, and all known features like the profiles of the electron density and temperature, the sawtooth frequency and radius are set as non-varying input parameters.

In a given run, the recycling factor is kept constant to a value for which the asymptotic signal is fairly correct, as this is almost independent of other transport parameters. The mathematical form of the profiles is not varied for each run either.
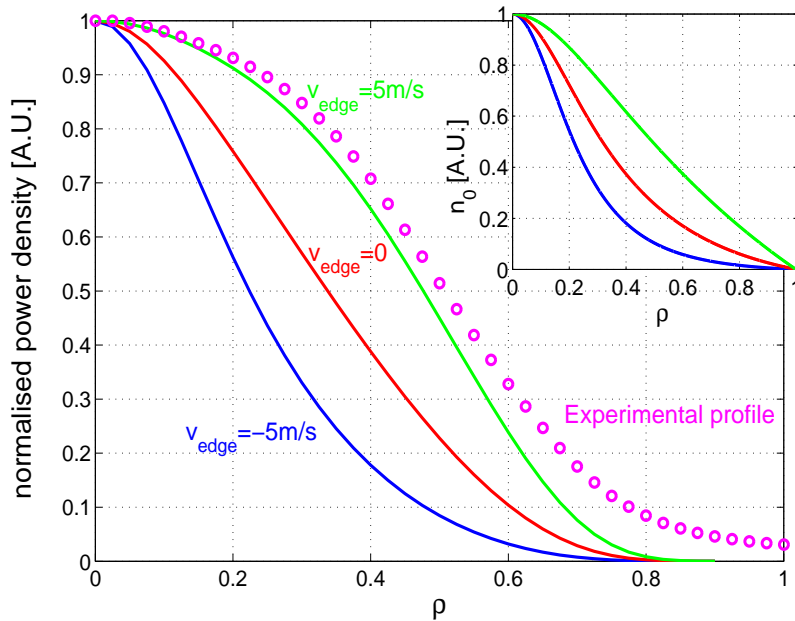
Fig.5.5 - SXR profiles corresponding to the solution of Eq.(4.2) for different assumption on the edge velocity, compared to the tomographically inverted profile of the impurity SXR emission of shot #21022 at t=0.664s. In the inset, the fundamental impurity distributions are shown. The excessively high experimental profile at the edge may result from the regularisation procedure in the tomographic inversion.

The core routine of each run is the variation of the edge diffusivity for the correction of the impurity lifetime and of the edge convective velocity in order to set the experimental *fwhm*. All other parameters, like the central diffusion coefficient D_0 and the velocity profile $v'_0 \equiv \frac{dv}{d\rho}\Big|_{\rho = 0}$ are subsequently modified in order to reproduce the signals during the influx phase. This operation induces small changes in the values of τ_{imp} and *fwhm* which require an easy correction of D_{edge}, and v_{edge}.

It is possible to change other parameters which have important effects on the signal shape

but are normally not precisely known, like the source duration or the delay of the first saw-tooth after the start of the injection. Additional experimental data which allow to determine the whole set of transport related parameters are the relative intensity of different line integrated signals or their different risetimes. As it is found from the experimental observations and from simulations with any kind of transport parameters, the exponential decay times of the signals from different chords is almost the same. While this fact allows the determination of the edge parameters from the shape of any chord, it cannot be used to find the bestfitting values of other parameters.

A consistency check on the bestfitting values D and v can be made with a direct comparison of the experimental impurity profiles and the theoretical eigenfunctions which were presented in Section 4.1.1 as solutions of Eq.(4.2). The peaking of the impurity density and hence of the SXR emission are sensitively dependent on the convective velocity for a given diffusivity profile. As an example, Eq.(4.2) has been solved with the bestfitting diffusivity of shot #21022 (Fig.5.4) and three different edge velocities. The corresponding fundamental eigenfunctions, described in Section 4.1.1 and shown in the inset of Fig.5.5, have been used to calculate the profile of emissivity in the SXR spectral range. The experimental profiles of the electron density and temperature have been used while the radiation parameter has been obtained with STRAHL in the corona approximation. The comparison has been made with a tomographically inverted profile of the impurity density at $t = 0.664\,\text{s}$ when the higher modes have disappeared and only the fundamental distribution is left. As shown in Fig.5.5, the profile obtained with $v_{edge} = 5\,\text{m/s}$ is very close to the experimental one, which is consistent with the bestfitting value $v_{edge} = 3.8\,\text{m/s}$.

It has to be remarked that the tomographic inversion with regularisation methods such as MFI provides excessively high values close to the plasma edge, hence the profile comparison is meaningful only for the central part of the plasma. Moreover, it is possible that the calculated profiles are underestimated at the edge by the use of the coronal radiation parameter, as the transport of highly ionised impurities from the centre is neglected.

5.2 Comparison with measured TCV data

In this Section the results of STRAHL simulations on impurity injections in real TCV discharges are presented, together with the comparison with the neoclassical predictions for the

same plasmas. Selected shots from the elongation, triangularity and toroidal magnetic fields are included, for which the impurity confinement time showed a dependence on the plasma geometry. As it was described in Section 5.1.2, the determination of the edge diffusivity and convective velocity is easily obtained from the time evolution of the line integrated SXR signals, while the evaluation of the central values is strongly affected by the sawtooth activity (see Fig.5.2). The neoclassical parameters have been evaluated by means of the NEOART
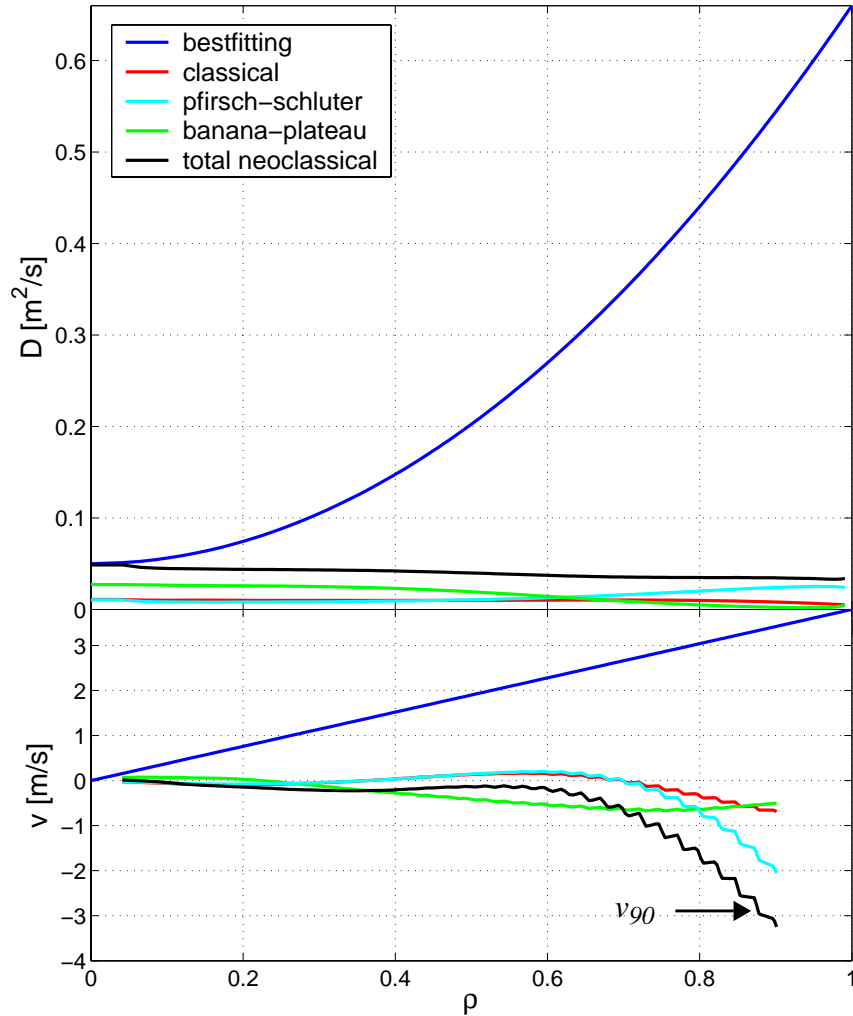
Fig.5.6 - Profiles of the neoclassical D and v transport coefficients. The classical, banana-plateau, Pfirsch-Schlüter contributions as well as the total are compared with the bestfitting value for shot #21022. The values of the convective velocity at the plasma edge cannot be determined with sufficient accuracy, so their profiles are shown up to ρ=0.9.

package included in STRAHL, which calculates separately the classical, banana-plateau and Pfirsch-Schlüter contributions of D and v. As these contributions are present for any value of the collisionality, the total coefficients are actually the sum of all three contributions. In

Fig.5.6 the bestfitting profiles together with the neoclassical predictions are shown for shot #21022. As for all other analysed discharges, the edge transport is evidently driven by anomalous phenomena as the bestfitting diffusivity is an order of magnitude higher and the direction of the convective velocity is reversed. On the contrary, the central diffusivity appears to be close to the neoclassical prediction, even if there exist a large incertitude on the bestfitting value. Such a comparison will be presented for those cases in which D_0 has been determined with precision.

In the following, the bestfitting parameters D_{edge} and v_{edge} are presented, from simulations in which the radial profile of diffusivity was parametrised with a parabola and fixed central value $D_0 = 0.05 \, \text{m}^2/\text{s}$, $D(\rho) = D_0 + (D_{edge} - D_0)\rho^2$ while the profile of the convective velocity was linear, $v(\rho) = v_{edge}\rho$. Different profiles have been attempted, like an exponential dependence of the diffusivity on the normalised radius (following results in Ref.[35]), leading to the ansatz $D(\rho) = D_0 \left(\dfrac{D_{edge}}{D_0} \right)^{\rho}$, or a parabolic profile for the convective velocity, like in the example of Fig.5.2. In the simulation of a single injection, the edge values of the transport coefficient however were little affected by the different profiles. The small variations which were found for $\rho = 1$ have been observed to be correlated to steeper profiles of the bestfitting transport coefficients around the edge, while the mean values of $D(\rho)$ and $v(\rho)$ in the peripheric area outside the sawtooth radius were fairly independent of the attempted parametrisation.

The impurity source at the edge was set constant for a duration of 4ms, in agreement with the duration of the spectroscopic signals of the neutral Si. Shorter durations have been attempted and did not affect the time evolution of the line integrated signals. Moreover, this value provides the best agreement of the relative peak intensity of the SXR signals from different chords.

5.2.1 Bestfitting and neoclassical values for *D* and *v*

The experimental results presented in Chapter 4 show that in the scans of elongation, toroidal magnetic field and triangularity the confinement time of the injected impurities varied according to the different configurations. In order to obtain the bestfitting parameters D_{edge} and v_{edge} for selected shots from the scans, the fwhm of the line integrated SXR signals has been taken into account as well as the sawtooth frequency, the mixing radius and the intensity of the residual signal after the depletion phase.

5.2 Comparison with measured TCV data

With increasing elongation the sawtooth frequency changed from $f_{ST} \approx 200\,\text{Hz}$ at $\kappa = 1.68$ to $f_{ST} \approx 360\,\text{Hz}$ at $\kappa = 2.28$, the average mixing radius from 20cm to 26cm, since the normalised inversion radius was fixed at the value $\rho_{inv} = 0.55$. No correlation was found between the elongation and the residual signal, which was typically 7÷12% of the peak value on chord #30 of the soft x-ray system.

The results of the simulations are shown in Fig.5.7. The whole dependence of the impurity confinement time on the elongation is due to a change in the diffusivity, while the convective velocity is fairly constant around the value $v_{edge} \approx 2\,\text{m/s}$ and always outwardly directed. The increase of diffusivity with increasing elongation accounts for the reduction of lifetime, shown in Fig.4.15, and for the increase in the size of the plasma. Simulations of the sawtooth effects on the impurity confinement time, described in Section 5.1.2, can lead to the conclusion that the increase in the sawtooth frequency at high elongation has a marginal effect on the observed lifetimes.

The calculated value of diffusivity at low elongation, $D_{edge} \approx 0.36\,\text{m}^2\text{/s}$ for κ=1.68, is a typ-
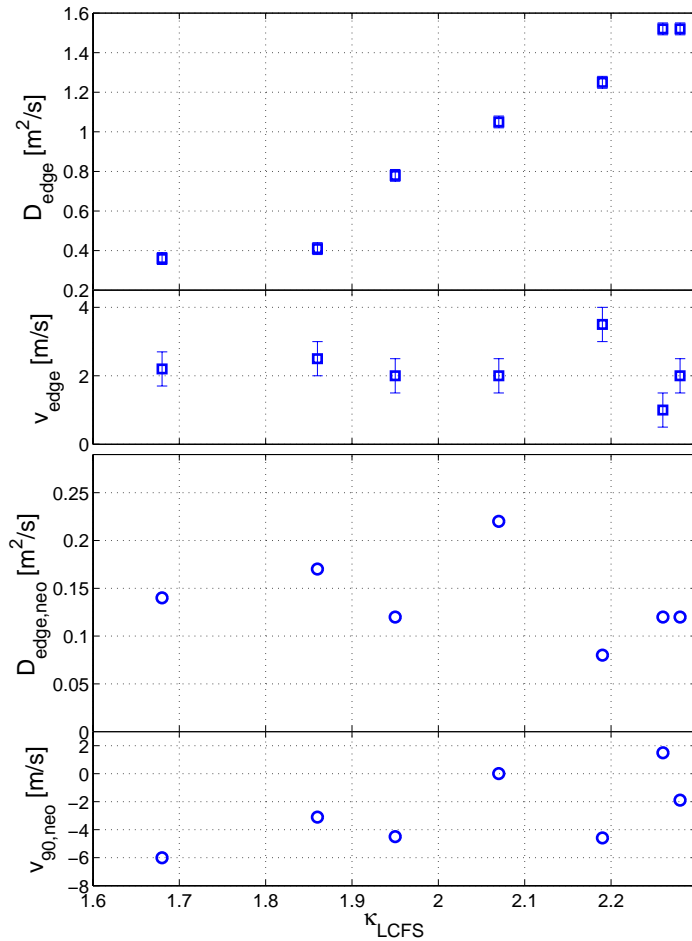
Fig.5.7 - (Top) Bestfitting parameter couples (D_{edge}, v_{edge}) used to reproduce the SXR signals of selected shots in the scan of elongation. (Bottom) The neoclassical values of the edge diffusivity and convective velocity as calculated by NEOART for the same discharges. There appears to be a trend in the neoclassical convective velocity versus the elongation.

ical constant value which is found in the scans of toroidal magnetic field and triangularity. The neoclassical edge values of the diffusivity and convective velocity, reported in Fig.5.7 (bottom) are lower than the bestfitting ones of a factor of 2.5 at low elongation up to a factor of 10 at the top end of the scan. The neoclassical diffusivity appears not correlated to elongation, while the inward edge velocity is reduced with increasing κ. In a case at $\kappa = 2.26$ the neoclassical velocity is found to be outwardly directed. In this scan, like in all other cases, the convective velocity -indicated as $v_{90,neo}$- has been evaluated at $\rho = 0.9$, as the edge value appears to be strongly affected by the incertitude in the experimental determination of the edge values of a number of plasma parameters.
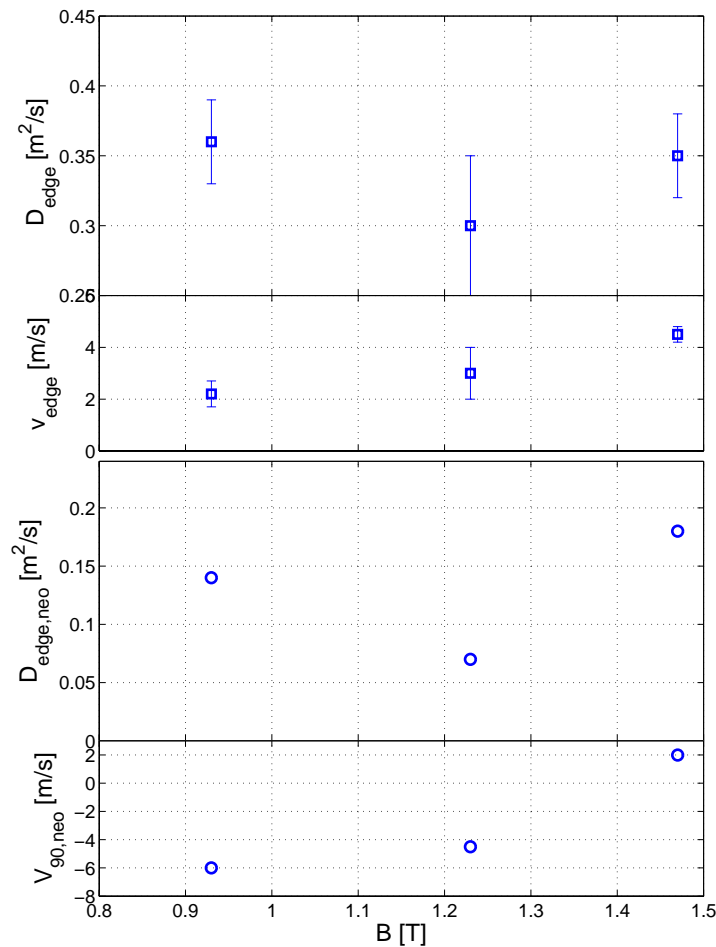
Fig.5.8 - (Top) Bestfitting parameters as function of the toroidal magnetic field. The point at B_T=0.93T belongs also to the elongation scan, at κ=1.68, while the point at B_T=1.47T is part of the triangularity scan at δ=0.28. (Bottom) The neoclassical values of the edge diffusivity and convective velocity as calculated by NEOART for the same discharges.

The reduction of τ_{imp} with increasing toroidal magnetic field is fully due to an increase in the radial convective velocity whose value goes from $v_{edge} \approx 2$ m/s to $v_{edge} \approx 4.5$ m/s and is directed outward. In Fig.5.8 the results of the simulation on selected injections are shown. Like in the elongation scan, the neoclassical edge diffusivity lies below the value of $0.2 \text{m}^2/\text{s}$ and it is lower than the bestfitting values of at least a factor of 2. The neoclassical velocity

changes with the magnetic field and again in one case at $B_T = 1.47\,\text{T}$ it is positive.
The dependence of the convective velocity on the triangularity is evident in Fig.5.9. In this
scan, performed in the range $\delta = -0.16 \div 0.6$ the impurity confinement time was fairly con-
stant around 25ms for $\delta > 0.2$ and increasing for lower values to negative triangularities. The
bestfitting transport parameters show that the edge diffusivity is constant or just slightly de-
creasing, while the lifetime behaviour represented in Fig.4.14 is correlated to a change in the
edge convective velocity. Its values lie around $v_{edge} \approx 4.5\,\text{m/s}$ until the threshold at $\delta = 0.2$
then a decrease is observed in correspondence of the increase of the impurity lifetime. At
$\delta = 0.06$ the edge velocity has fallen to around 0.
The neoclassical values in the scan of triangularity are similar to those found previously.
Both the diffusivity and the convective velocity are not clearly correlated to the triangularity;
the values of D_{edge} lie around $0.1 \div 0.15\,\text{m}^2/\text{s}$, a factor of 2 at least below the bestfitting val-
ues, and the velocity at $\rho = 0.9$ is slightly negative, except in one case.
The simulation of the signals obtained in the electron density scan (Fig.4.18) show that the
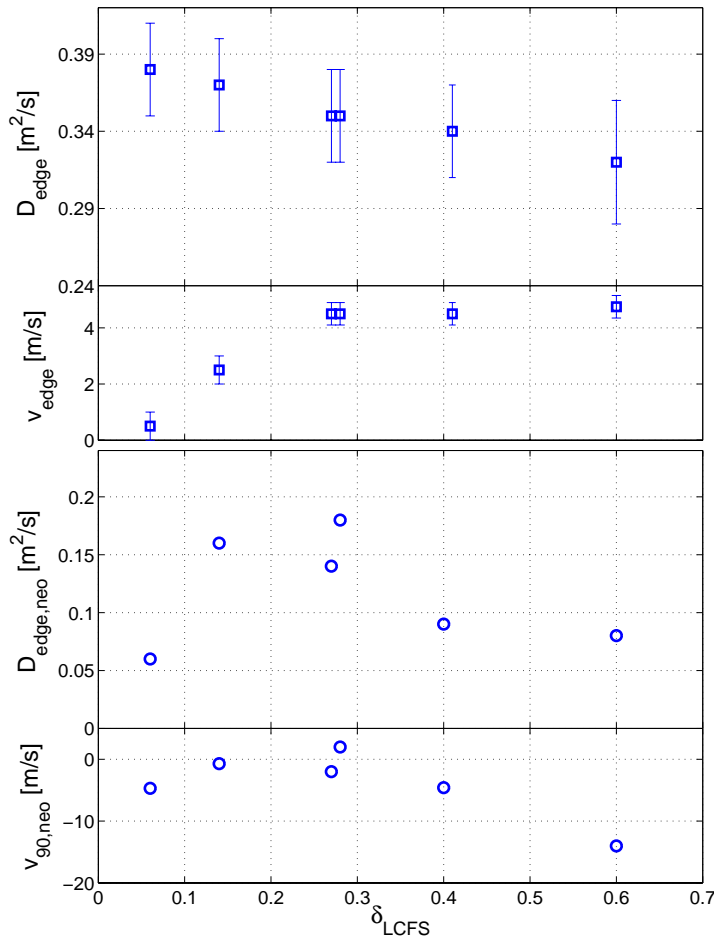
Fig.5.9 - (Top) Dependence of the diffusivity and the convective velocity on the plasma triangularity. (Bottom) The neoclassical values of the edge diffusivity and convective velocity as calculated by NEOART for the same discharges.

limiter and divertor configurations of plasmas with the same geometry and electron density sensitively differ in the values of the edge convective velocity. This parameter lies around 0 in the diverted plasmas and, in this configuration, the edge diffusivities are higher. In both cases they correlate inversely with the impurity confinement time, and their dependence is very strong, since D_{edge} can vary of about $0.15 m^2/s$ per 1ms of difference in τ_{imp}. The results of these simulations are shown in Fig.5.10.

The differences between limited and diverted discharges appear also in the neoclassical calculations. The edge diffusivity is higher in diverted configurations both for the bestfitting and in theoretical values, although their ratio is no lower than a factor of 3. Moreover, while the bestfitting edge velocity in diverted shots was around 0, the neoclassical results give clearly positive values around +5m/s. The same tendency to positive velocity is found in the neoclassical values for limiter shots at higher electron density.

The lack of data on the magnetic reconstruction and on the profiles of electron temperature and density for the shots included in the current scan (Fig.4.19) prevented the analysis of im-
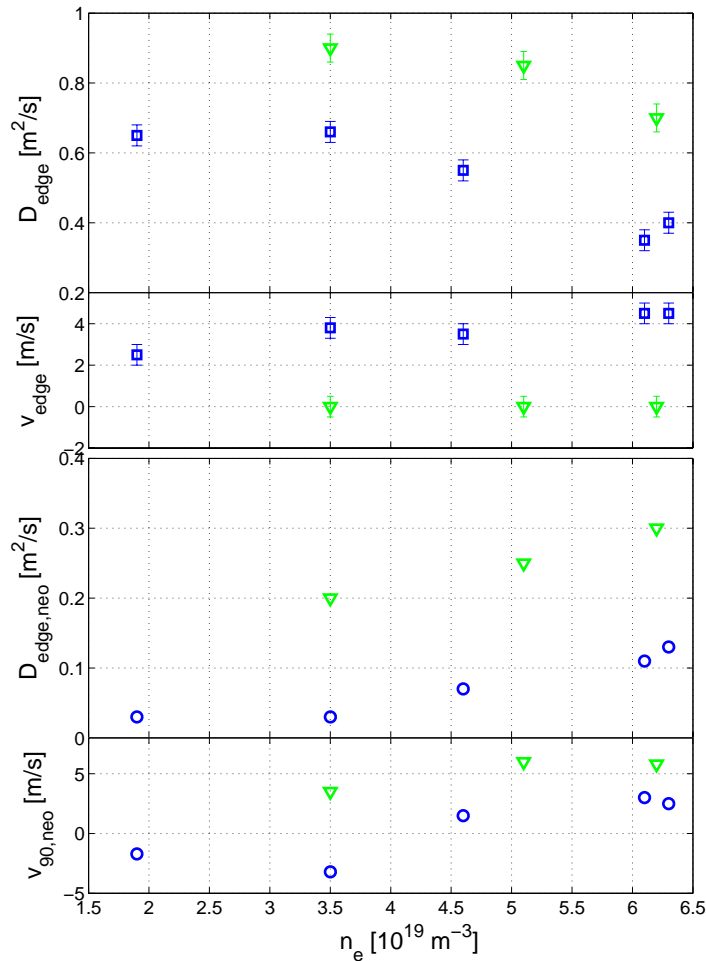
Fig.5.10 - (Top) Bestfitting parameters for the simulation of selected injections in the electron line averaged density scan. In blue squares the results of the limiter configuration are shown, while green triangular points refer to divertor plasmas. (Bottom) The neoclassical values of the edge diffusivity and convective velocity as calculated by NEOART for the same discharges.

purity transport in these discharges. However, the simulation of two injections for currents below and above the threshold at $I_P \approx 250\,\text{kA}$, where the jump in the confinement times is observed, has been attempted using the reconstruction and the profiles of shot #19785, whose parameters are comparable. This way, it is possible to give at least an estimate of the difference in the transport parameters D and v which are responsible of the sudden increase in the confinement time for $I_P < 250\,\text{kA}$ in the current scan. The results of the simulation, reported in Table 5.1, indicate that while the edge diffusivity changes slightly across the current threshold, the edge convective velocity has opposite direction, being inwardly directed at lower current. The values of the edge diffusivity are in agreement with those obtained in the scan of electron density, reported in Fig.5.10.

Shot #	I_P [kA]	τ_{imp} [ms]	D_{edge} [m²/s]	v_{edge} [m/s]
20161	233	55	$0.64 \div 0.68$	$-4 \div -3.5$
20167	351	25.5	$0.84 \div 0.88$	$3 \div 3.3$

Table 5.1: Transport parameters of two selected shots in the plasma current scan.

The transition to a negative convective velocity for lower plasma currents is in principle in agreement with the observation of impurity accumulation which follows injection in a two shots at low current, as described in Chapter 4. An estimate of the radial profile of the convective velocity can be obtained by means of simulation, using again shot #19785 as a reference plasma for n_e and T_e profiles. The setting of a stationary state in the impurity distribution requires the condition of zero radial flux which can be written according to the transport equation, Eq.(4.2), as:

$$D(r)\frac{\partial \bar{n}}{\partial r} - v(r)\bar{n} = 0 \tag{5.14}$$

where $\bar{n}$ is the asymptotic time independent impurity distribution. Once an ansatz on the diffusivity profile has been done and a distribution $\bar{n}$ has been obtained by the inversion of the line integrated signals, the velocity profile is calculated from Eq.(5.15):

$$v(r) = D(r)\frac{1}{\bar{n}}\frac{\partial \bar{n}}{\partial r} \tag{5.15}$$

For simplicity, $\bar{n}$ has been chosen to be represented as a gaussian, $\bar{n} = \bar{n}_0 \exp(-a\rho^2)$ and the diffusivity to have the usual parabolic profile $D(\rho) = D_0 + (D_{edge} - D_0)\rho^2$. The resulting

velocity profile is:

$$v(\rho) = -2a\rho[D_0 + (D_{edge} - D_0)\rho^2]\frac{1}{|\nabla\rho|} \qquad (5.16)$$

in which $|\nabla\rho|$ is given by the plasma magnetic reconstruction. In the simulation, a has been used as a free parameter together with D_{edge}, in order to reproduce the central and the peripheric line integrated signals. Although the time evolution is not well reproduced, the best agreement with the signals shown in Fig.4.20 has been obtained with $a = 22$ and $D_{edge} = 0.5\,\mathrm{m^2/s}$, and the corresponding velocity profile is shown in Fig.5.11. It has to be observed that the edge value is not well determined by the fact that $\bar{n}$ and $\frac{\partial\bar{n}}{\partial r}$ can be known only with high uncertainty. Consequently, different choices of $\bar{n}$ are likely to provide different values of v_{edge}, while the central value is quite well determined. For comparison, the profile of the neoclassical convective velocity relative to shot #19785 is also reported. In the inner region, the two profiles appear to be fairly in agreement, even if the neoclassical velocity is slightly positive for $\rho < 0.3$.
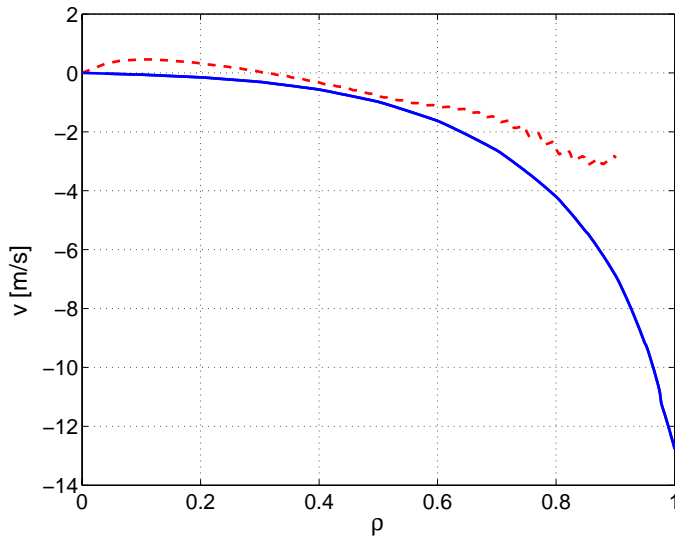
Fig.5.11 - The radial profile of the convective velocity which is required to reproduce the central impurity accumulation of shot #20164. The diffusion coefficient is $D(\rho) = 0.05 + 0.45\rho^2\,m^2\!/s$. In red, the profile of the neoclassical convective velocity calculated by NEOART.

It was not possible to simulate with STRAHL the observed temporal evolution of the signals from the ELMy ohmic H-mode presented in Table 4.2. For any couple of values (D_{edge}, v_{edge}) which provided the measured confinement time, the experimental signals showed a smaller *fwhm* than the simulated ones of no less than 5ms. This significant discrepancy may be explained by the role of the ELMs, which is not taken into account in the code, as the fast expulsion of particles at the plasma edge can account for the reduction of the impurity residence time in ELM plasmas.

The simulation of selected shots from the scan of elongation with injection of aluminum is presented in Fig.5.12. The shorter confinement time with respect to silicon injection in

equivalent plasmas is reflected in higher edge diffusion coefficients. The convective velocity, which is still positive and slowly varying along the scan, has a small effect on the time evolution of the line integrated signals and the uncertainty on its values is therefore higher. The diffusion coefficient in the plasma core is largely undetermined for most of the cases which have been analysed in this work. From Fig.5.2 it is evident how an uncertainty of 1ms in the timing of the first sawtooth crash after injection can lead to an indetermination of the central diffusivity in the range $D_0 < 0.6 \, \text{m}^2/\text{s}$. In some cases, however, the SXR line integrated signals were clear enough to determine the timing of the first sawtooth and an indication of the central diffusivity could be obtained. The values of D_0 reported in Table 5.2 have been determined to a precision of $\pm 0.01 \, \text{m}^2/\text{s}$ by means of the simulation of the correct central flow following the definition given in Eq.(5.13). It can be remarked that there exists a correlation between the edge diffusivity and the impurity confinement time, while the edge diffusivity is fairly constant for the considered shots. The comparison with the neoclassical
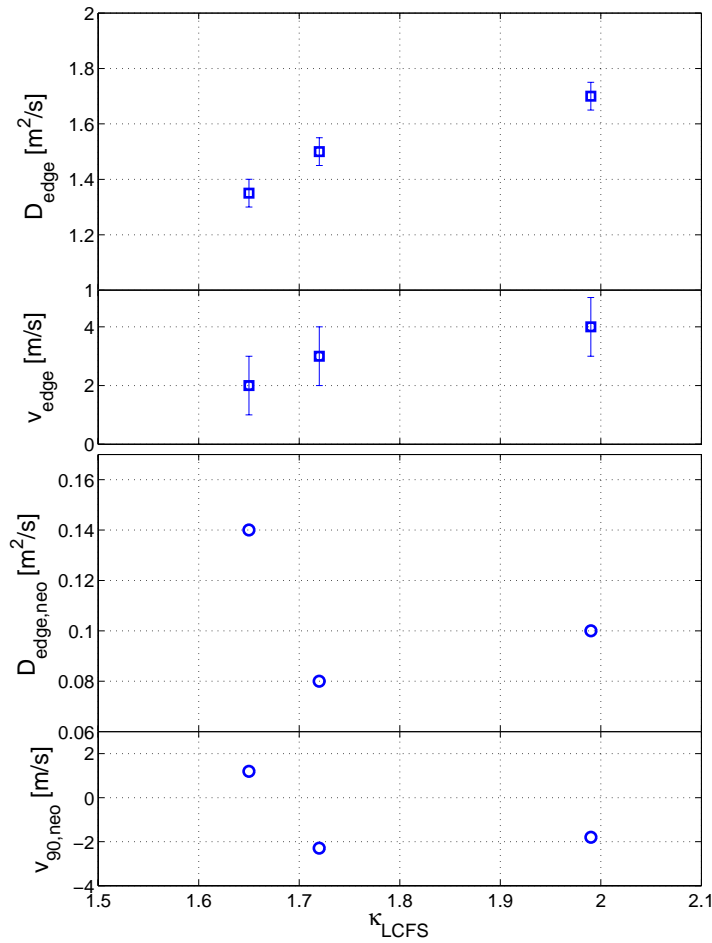
Fig.5.12 - (Top) Bestfitting parameters for selected shots of the elongation scan with injection of aluminum. (Bottom) The neoclassical values of the edge diffusivity and convective velocity as calculated by NEOART for the same discharges.

predictions shows that the bestfitting central value of the diffusivity is in agreement, within the incertitude of the measurement, with the neoclassical values.

Shot #	τ_{imp} [ms]	D_0 [m^2/s]	$D_{0,neo}$ [m^2/s]	Remarks
21164	27	0.03	0.04	Top end in B_T scan at B_T=1.47T; δ scan δ=0.28
19742	38	0.07	0.08	κ scan at κ=1.86
19782	57	0.08	0.07	δ scan at δ=0.06

Table 5.2: Central impurity diffusivity for some selected discharges.

5.3 Summary and discussion

In Section 5.2 the edge transport parameters, which allowed the best matching between experimental and simulated SXR signals, were presented for different plasma geometries and toroidal magnetic field values. Most of the bestfitting data were obtained by means of the reproduction of a small number of central chords of the soft x-ray system, however the results were checked on the experimental and simulated relative peak intensities of different line integrated signals viewing the plasma at many radial positions.

Despite the complexity of the quantitative description of the transport of moderate-Z impurities in plasma, fairly good simulations have been obtained with the variation of a small number of parameters. Apart from the experimental errors in the determination of the time evolution of the signals, some approximations of the STRAHL code could be correlated to the deviations between the observed and simulated data. The unicity of the transport profiles for all the ionised states and a simplified model for sawtooth crashes could be the most important, however the simulation of transport of impurities in which too many parameters have to be fitted would become an intractable task.

In the simplified frame in which the impurity transport coefficients have been parametrised with simple profiles along the plasma minor radius, a series of correlations has been found which allowed an easier search for the bestfitting parameters. In particular, the global confinement properties of impurities in TCV plasmas are principally driven by the transport at the plasma periphery, outside the mixing radius, more than in the core. This fact allows the search of the core transport parameters separately as function of the influx phase of impurities, once the edge values have been determined by the confinement time and the *fwhm* of

the line integrated signals. Finally, the recycling of impurities from the wall is almost completely determined by a single coefficient which is set according to the asymptotic intensity of the residual SXR signal after the depletion phase.

In this Chapter, the fact that the central values of the transport coefficients are largely undetermined has already been stressed. The effects of the convective and diffusive contributions to the transport of impurities in the plasma core can be observed and simulated during the buildup phase between two consecutive sawteeth, however the rather flat profiles due to previous sawtooth crashes limit the observation of the particle diffusion. The influx phase, since it provides sufficiently high gradients of the impurity density in the plasma core, can be investigated in order to obtain an estimate of the central diffusivity. In those few cases in which a fairly good estimation of D_0 has been obtained, its values are in agreement with the neoclassical predictions.

The sawtooth activity plays an important role in the transport of impurities in the plasma core only in the case in which the profiles are far from being flat. The model of sawtooth crash included in STRAHL, which consists in the flattening of the profiles of all the ion species inside the mixing radius, reproduces the inverted sawtooth in the line integrated SXR signals. The delay in time of the first sawtooth after the impurity injection has a large effect on the initial transport towards the plasma core and its indetermination affects the calculation of the central values of the transport parameters. During the depletion phase, however, the sawtooth frequency and the value of the mixing radii do not play a role in determining the impurity confinement time in the simulations.

The diffusion coefficient for impurities has been found to be dependent on the plasma configuration only in the scan of elongation, while a variation of triangularity or magnetic field did not change the edge diffusivity whose value lies around $D_{edge} = 0.35 \, \mathrm{m}^2/\mathrm{s}$. However, the increase in the plasma elongation and volume, together with the decrease of the impurity confinement time at higher elongation, led to higher values of the diffusivity, reaching $D_{edge} = 1.5 \, \mathrm{m}^2/\mathrm{s}$ for $\kappa = 2.28$. On the other hand, the variations of the impurity confinement time and the signal *fwhm* in the triangularity and toroidal magnetic field scans appear to be fully explained by the change in the radial convective velocity.

It may be a cause of concern that the value of the velocity has been found to be positive, i.e. outwardly directed, in the large majority of the injections. At the plasma edge, it has a constant value around 2m/s along the elongation scan, it varies between ~0.5m/s and ~5m/s in

the triangularity scan and between ~2m/s and ~4.5m/s in the scan of magnetic field, its behaviour being as expected correlated to the experimental observation of smaller confinement times for higher magnetic fields. The simulation of many other injections, not included in scans of plasma parameters, show a positive convective velocity as well. In some cases the variation of the *fwhm* as function of the convective velocity for constant τ_{imp} is slow and causes an incertitude on the value of both the edge transport parameters, but this incertitude, typically of the order of 1-2m/s is too small for a change of sign. The only exception to this behaviour is found in the scan of plasma current at the lower end, as in one case the velocity was inward with $v_{edge} \approx -3$ m/s and in similar configurations a central accumulation of impurities has been observed with $v_{edge} \approx -12$ m/s. In the diverted plasmas of the electron density scan the sign of bestfitting velocity was undetermined, as it was found that $v_{edge} \approx 0$. Similar experiments on other machines have almost always found inwardly directed convective velocities, with absolute values of the order of the 10m/s, of the same order of magnitude as predicted by the neoclassical theory. Theoretical calculations, referring to the intermediate Pfirsch-Schlüter regime, however allow the possibility of an impurity screening due to high enough ion temperature gradients[4]. Analogous considerations from theoretical calculations on the impurity behaviour in an ignited plasma[63] lead to negative values of *v/D* in case of flat ion temperature profiles and positive values if T_I is peaked; this effect is reported to be more evident with increasing *Z*. It has to be said however that these possibilities of a positive convective velocity are the result of calculations from the neoclassical theory and still wait for an experimental check. In any case, they are not relevant to TCV and this work. The transport coefficients which have been found in this Chapter are sensitively different from the theoretical values provided by the neoclassical theory, which has been presented in Section 2.3. This discrepancy is evident in the comparison between the bestfitting and the neoclassical values of the diffusion coefficient, which differ of a factor of 2 to 10 in almost all cases which have been analysed. The picture becomes more complex in the case of the convective velocity at the plasma edge, as its neoclassical values, calculated by the NE-OART routine included in STRAHL, are not unequivocally negative. On the contrary, there are many cases in which the neoclassical convective velocity show a regular trend which changes sign. Moreover, positive values are commonly found at the top end of the scans of electron density. In all cases, however, the neoclassical and experimental values of convective velocity share the same order of magnitude, being $0 \div 10$ m/s in magnitude.

5.3 Summary and discussion

The comparison between the bestfitting experimental values and the neoclassical values of the transport coefficients reveals the dominating role of the anomalous transport which overcomes the neoclassical contribution and leads to shorter impurity confinement times. The discrepancy between convective velocities suggests that impurity convection too is a result of anomalous processes.

6. SUMMARY

Analysis of impurity transport in TCV plasmas has revealed significant effects of the geometry on the confinement of moderate-Z particles, which have potentially important implications in the design of fusion reactors. The exceptional shaping capability of TCV has been used to explore a wide range of plasma parameters, including high elongations, negative and high positive triangularities, different values of the toroidal magnetic field, with a range of different plasma densities and currents.

The impurities injected in TCV for this work have been produced by a dedicated laser ablation system, which allows one injection per plasma. The radiative emission has been measured with a filtered 200-channel soft x-ray photodiode array and a SPRED spectrometer for ultraviolet radiation. The SXR diagnostic, because of its spatial sensitivity, has been the main diagnostic for the observation of impurities in the plasma core. Its spatial and temporal resolution have permitted the observation of the concentration of impurities with typical spatial and temporal resolutions of 3-4cm and 13μs. These measurements have been complemented by the detection of ultraviolet line radiation from partially stripped impurity ions emitted at the plasma periphery ($\rho > 0.9$).

The time evolution of the line integrated SXR signals has been used to investigate the transport properties of the non-recycling trace silicon and aluminum impurities. The duration of impurity source at the plasma edge was short enough to separately observe the particle influx and outflux phases. During the influx phase, inverted sawtooth jumps in the signal of central chords demonstrate the role of sawtooth crashes in the transport of the impurities towards the plasma core. During the outflux phase, all line integrated SXR signals and the line ultraviolet intensities appear to decay exponentially with almost equal time constants. This parameter, which is commonly referred to as the global impurity confinement time, constitutes the main experimental observation for the analysis of this thesis, as it has been measured in different plasma conditions, including a variety of plasma shapes. The similarity of the time evolution of central and edge signals from both diagnostics has been interpreted as a consequence of the formation of a fundamental impurity density profile during the outflux phase, which is the solution of the transport equation, although the complete physical description is compli-

cated by the presence of sawtooth activity and many ion species.

The impurity confinement time has been obtained for different plasma configurations, with injections into dedicated series of plasma discharges. The impurity confinement time is observed to depend on the plasma elongation, triangularity and magnetic field, while the electron density has little effect at least in limiter configuration. A remarkable increase in the confinement time is found in the scan of plasma current below a marked threshold. In a couple of discharges whose current was close to the threshold an accumulation of impurities in the plasma centre is observed. As far as the plasma geometry is concerned, the confinement time in the triangularity scan shows similar behaviour as the electron energy confinement, as an increase of τ_{imp} is observed for lower (negative) triangularity. The most interesting results have been observed in a scan of elongation, which was performed at constant sawtooth normalised radius. While the electron energy confinement time is constant over the elongation range, the impurity confinement time decreases at higher elongations, possibly providing a favourable option for future advanced reactor designs. A comparison between silicon and aluminum injections shows a marked difference in their confinement times, which was only partly explained by different plasma parameters.

The radial impurity transport in TCV has been analysed by means of the 1D code STRAHL, which reproduces the line integrated SXR signals from impurities. The plasma parameters, including sawtooth activity, have been taken from experimental plasmas, while the radial profiles of the diffusion coefficient and the convective velocity have been included as free input parameters. By means of "bestfit" routines, these parameters have been modified in order to reproduce the time evolution and the relative intensity of the experimental signals.
The parameters which most affect the confinement of impurities have been identified in the edge diffusion coefficient and the edge convective velocity. All transport mechanisms in the plasma core have shown little sensitivity to the confinement time. Sawtooth activity has been modelled in STRAHL as a sudden flattening of the density profiles of all ion species inside the sawtooth mixing radius. It is the most important component of the core transport, while the diffusivity and the convective velocity, in agreement to the experimental observations, yield only small changes to the impurity density profiles during the buildup phase.
The effect of the edge transport parameters has been established as a function of the plasma geometry, by means of the simulation of the experimental results. The long confinement

times in large highly elongated plasmas have been explained by an increase of the diffusion coefficient, the radial convective velocity being constant and outwardly directed. The changes in τ_{imp} at different triangularities or toroidal magnetic fields have been correlated to a change in the velocity, whose direction has been found to be outward. This feature, which is predicted in the frame of the neoclassical theory only in the case of high-Z impurities and high ion temperature gradients, was not observed in other experiments. In all cases, anomalous diffusivity dominates neo-classical predictions by a factor of 3 to 7 both in the plasma centre and at the edge. The experimental convective velocity is found to be inwardly directed only in the discharges with central impurity accumulation and at low values of the current (I_P<250kA), corresponding to values of the safety factor $q_{95} > 4.2$.

This thesis constitutes the first experimental work on the effects of plasma shaping on the confinement of impurities in a tokamak. Although silicon was the principal impurity injected into TCV, other elements are more likely to enter the plasma in a reactor. As in this work aluminum displays different confinement times, further analysis needs to be performed with various elements and a possible dependence on the mass and charge of the impurities may be found.

Further work should also explore more reactor relevant conditions with investigations of impurity transport behaviour in discharges with ECRH and neutral beam additional heating, current drive, and in plasmas with improved confinement such as H-modes and internal transport barriers.

A. THE GSVD METHOD

A.1 Mathematical features of the GSVD

One of the basic problems in experimental physics is the superposition in signals of an interesting dynamics with an uncontrollable but known and regular perturbation. In plasma physics, sawteeth are a typical example of periodic oscillations which affect plasma density, temperature and electromagnetic emissivity. In many cases the error of measure of the interesting phenomena is drastically reduced when sawteeth are filtered out.

The technique of the Generalised Singular Value Decomposition[87] (GSVD) is based on a linear technique which involves filtering in the phase or state space, and provides a net separation between sawteeth and the intrinsic emissions from plasma, or from impurities. Even if the process on which GSVD has been applied in this case, i.e. impurity radiation from plasma core, is non linear, the sawtooth period and radius are not affected by impurity injection, and the utilisation of this method is still useful. The variation of the sawtooth amplitude in the integrated signal is self-consistent and does not affect the propagation through the plasma, and it is consequently taken into account in this method.

The main requirement for a GSVD analysis is the possibility to make two different observations, one with only the regular perturbation and the other including as well the phenomenon of interest. Such observations come generally from different diagnostics of from a multichannel diagnostic, giving a set of trajectories in a space whose dimension is equal to the number of independent measurements.

The first step for the analysis is the reconstruction of the phase space. As it is supposed that the measurements take place at discrete identical times for all channels, the matrix formalism is well suited for this kind of problems. The matrix Y is built such as its element (i,j) is the measurement of the channel j at the time t_i, or $Y_{ij} = y(x_j, t_i)$, and the time averages are removed as they don't contain information about the transient phenomena.

Let $y(x, t)$ be the set of measurements containing the observations and $u(x, t)$ the set in which only the regular noise is present. The recording condition must be equal, in number of channels and sampling frequency, but the two measurements can contain a different number of time samples.

Following the SVD idea[88], the matrix $y(x, t)$ is decomposed in a unique set of orthonormal spatial and temporal modes:

$$y(x, t) = \sum_{k=1}^{K} \alpha_k a_k^*(t) v_k(x) \tag{A.1}$$

in which $\langle a_k a_l^* \rangle = \delta_{kl}$, $\langle v_k v_l^* \rangle = \delta_{kl}$ and K is the smallest between the numbers of samples or probes. The modes are sorted so to have $\alpha_1 \geq \alpha_2 \geq ... \geq \alpha_K \geq 0$. The further step in GSVD consists in considering a common basis to both $y(x, t)$ and $u(x, t)$. This basis is again complete and unique, but not necessarily orthogonal:

$$y(x, t) = \sum_{k=1}^{K} \alpha_k a_k^*(t) v_k(x) \tag{A.2}$$

$$u(x, t) = \sum_{k=1}^{K} \beta_k b_k^*(t) v_k(x)$$

where in general $\langle v_k v_l^* \rangle \neq \delta_{kl}$, however the temporal modes are orthonormal. By convention the weights are chosen to give $\alpha_k^2 + \beta_k^2 = 1$. The ratios $\sigma_k = \alpha_k / \beta_k$ are referred to as the generalised singular values of $y(x, t)$ and $u(x, t)$.

The basis vectors v_k are chosen in such a way that the largest of these values, σ_1, is maximised and the lowest, σ_K, is minimised. Thus the GSVD method projects the trajectory of $y(x, t)$ on the first vectors of the set v_k and the trajectory of $u(x, t)$ on the last. Clearly if a truncated summation of the kind of Eq.(A.2) is considered, most of the interesting signal will be retained:

$$y(x, t) = \sum_{k=1}^{L \leq K} \alpha_k a_k^*(t) v_k(x) \tag{A.3}$$

It can be shown[102] that the generalised eigenvalues and the basis functions are the solution of the symmetric eigenvalue problem, which can be written as:

$$\langle Y^* Y \rangle v_k = \sigma_k^2 \langle U^* U \rangle v_k \tag{A.4}$$

but anyway an algorithm for the derivation of the basis function exists and it is explained in Ref.[103].

A.2An application on TCV plasma sawteeth

As an example of application of the GSVD to real signals from the soft x-rays detection system on TCV, in the following an aluminum injection will be considered. The raw signal from the soft x-ray tomography channel 30 is shown in Fig.A.1, where the time intervals delimiting the pure sawtooth activity $u(x, t)$ and the signal to be "cleaned" $y(x, t)$ are highlighted.
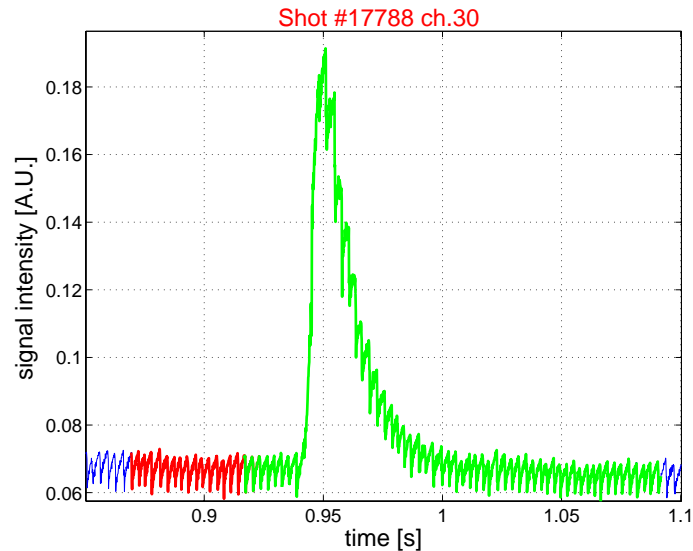
Fig.A.1 - The raw soft x-ray signal after injection of aluminum. In red, the pure sawtooth activity is shown, while in green the actual signal to be cleaned is highlighted.
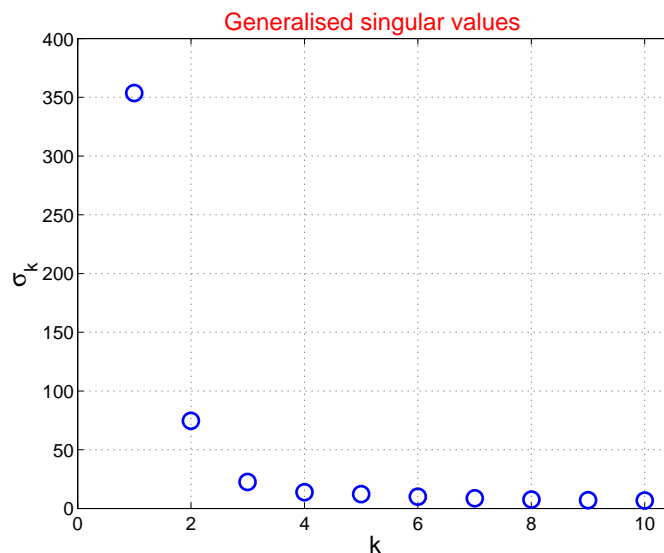
Fig.A.2 - The generalised singular values sorted in descending order for the signal shown in Fig.A.1. The first two are muck bigger than the following ones, so they contain almost all the information about the effective impurity signal.

By means of standard routines, the average value of $u(x, t)$ is removed as background from both signals and the GSVD routine is applied. The first ten resulting generalised singular values $\sigma_k = \alpha_k / \beta_k$ are shown in Fig.A.2, from which it is evident that the first 2 or 3 topos contain almost all the information about the impurity signals. The cleaned signal, superposed to the raw one, is shown in Fig.A.3 and in this case the minimisation of the sawtooth activity has been obtained considering the first three topos, giving to the last one a weight of 0.5. It can be remarked, in the plot of the difference between raw and clean data, that a deviation exists between the first and second sawteeth following injection. However, the short duration of this discrepancy does not affect the subsequent evolution of the cleaned signal.
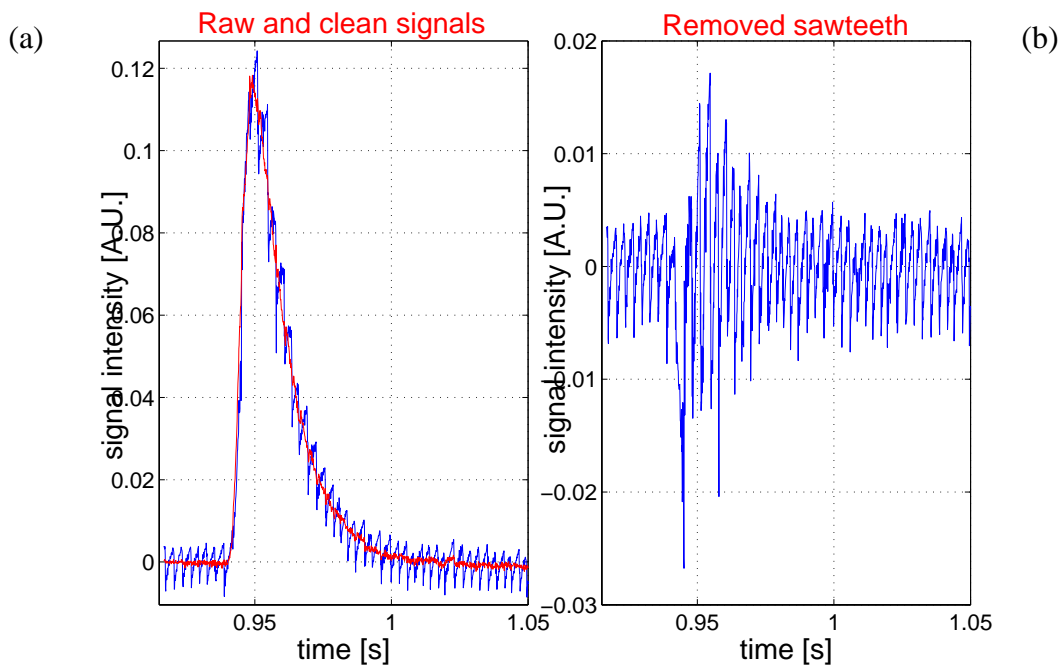
Fig.A.3 - (a) The raw and cleaned signals, superposed. (b) The difference between them, showing a discrepancy between the first two sawteeth following injection.

Bibliography

[1] D.R.O.Morrison, *Proc. 24th International Seminar on Planetary Emergencies,* Erice, Italy (1999)

[2] *Energy Statistics Yearbook 1993,* United Nations, Department of Economic and Social Infomation and Policy Analysis, Statistical Division, New York (1995)

[3] M.Verral, *Nature* **371** (1994), 274

[4] J.A.Wesson, *Tokamaks*. Clarendon Press, Oxford, 2nd Edition (1997)

[5] L.A.Artsimovitch et al., *Proc. 3rd Int. Conf on Plasma Physics and Controlled Nucl. Fusion Reasearch*, Novosibirsk (1968)

[6] R.V.Jensen et al., *Nucl. Sci. Eng.* **65** (1978), 282

[7] F.Troyon et al., *Plasma Phys. Control. Fusion* **26** (1984), 209

[8] R.V.Jensen et al., *Nucl. Fusion* **17** (1977), 1187

[9] ITER Physics Expert Groups on Confinement and Transport et al., *Nucl. Fusion* **39** (1999), 2175

[10] D.Reiter et al., *Nucl. Fusion* **30** (1990), 2141

[11] F.Hofmann et al., *Plasma Phys. Contr. Fusion* **36** (1994), B277

[12] J.M.Moret et al., *Phys. Rev. Lett.* **79** (1997), 2057

[13] H.Weisen et al., *Nucl. Fusion* **37** (1997), 1741

[14] H.Weisen et al., *Plasma Phys. Control. Fusion* **39** (1997), B135

[15] F.Hofmann et al., *Plasma Phys. Control. Fusion* **43** (2001), A161

[16] R.R.Parker et al., *Nucl. Fusion* **25** (1985), 1127

[17] J.V.Connor, *Plasma Phys. Control. Fusion* **37** (1995), A119

[18] N.A.Uckan et al., *ITER Physics design Guidelines: 1989* (1990)

[19] I.Furno, *Fast transient transport phenomena measured by soft x-ray emission in TCV tokamak plasmas*, PhD thesis No. 2434, Ecole Polytechnique Fédérale de Lausanne, Switzerland (2001)

[20] H.Reimerdes et al., *Plasma Phys. Control. Fusion* **42** (2000), 629

[21] A.Pochelon et al., *Nucl. Fusion* **41** (2001), 1663

[22] H.Weisen et al., *Nucl. Fusion* **42** (2002), 136

[23] B.B.Kadomtsev, *Fisika Plazmy* **1** (1975), 710

[24] H.Weisen et al., *Plasma Phys. Control. Fusion* **38** (1996), 1137

[25] H.Weisen et al., *Plasma Phys. Control. Fusion* **38** (1996), 1415

[26] J.M.Moret et al., *Plasma Phys. Control. Fusion* **37** (1995), A215

[27] J.F.Friichtenicht, *Rev. Sci. Instr.* **45** (1974), 51

[28] D.G.Whyte et al., *Nucl. Fusion* **34** (1994), 203

[29] E.S.Marmar et al., *Rev. Sci. Instr.* **46** (1975), 1149

[30] G.Kocsis et al., *IEEE Transaction on Plasma Science*, **24** (1996) 1120

[31] S.A.Cohen et al., *Proc. 7th European Conf. on Controlled Fusion and Plasma Physics*, Lausanne (1975), 137

[32] D.Pasini et al., *Nucl. Fusion* **30** (1990), 2049

[33] K.Behringer et al., *Nucl. Fusion Supplement* **1** (1987), 197

[34] D.G.Whyte et al., *Phys. Rev. Lett.* **81** (1998), 4392

[35] K.Behringer et al., *Nucl. Fusion* **29** (1989), 415

[36] P.B.Parks et al., *Nucl. Fusion* **28** (1988), 477

[37] R.Dux et al., *Nucl. Fusion* **39** (1999), 1509

[38] R.A.Pitts et al., *Jour. Nucl. Mat.* **266** (1999), 648

[39] R.Giannella et al., *Nucl. Fusion* **34** (1994), 1185

[40] M.Mattioli et al., *Nucl. Fusion* **38** (1998), 1629

[41] P.G.Carolan et al., *Nucl. Fusion* **30** (1990), 2616

[42] M.Mattioli et al., *Nucl. Fusion* **35** (1995), 1115

[43] K.H.Burrell et al., *Nucl. Fusion* **21** (1981), 1009

[44] S.A.Cohen et al., *Phys. Rev. Lett.* **35** (1975), 1507

[45] K.W.Gentle et al., *Plasma Phys. Control. Fusion* **26** (1984), 1407

[46] E.S.Marmar et al., *Nucl. Fusion* **22** (1982), 1567

[47] V.V.Parail et al., *Nucl. Fusion* **37** (1997), 481

[48] P.Galli et al., *Nucl. Fusion* **38** (1998), 1355

[49] H.Weisen et al., *Rev. Sci. Instr.* **62** (1991), 1531

[50] R.P.Mc Whirter, *Plasma diagnostic techniques*, R.H.Huddlestone and S.L.Leonard eds., New York (1965)

[51] K.Behringer, *Jet report JET-R(87)* **08** (1987)

[52] I.H.Hutchinson, *Principles of plasma diagnostics*, Cambridge University Press, Cambridge (1992)

[53] H.Ryufuku et al., *Phys. Rev. A* **20** (1979), 1828

[54] M.Bornatici et al., *Nucl. Fusion* **23** (1983), 1153

[55] A.A.Galeev et al., *Soviet Physics JETP* **26** (1968), 233

[56] S.I.Braginskii, *Reviews of plasma physics*, M.A.Leontovich ed., New York (1965)

[57] S.P.Hirshman et al., *Nucl. Fusion* **21** (1981), 1079

[58] R.D.Hazeltine et al., *Plasma confinement*, Addison-Wesley Publishing Company, Redwood City (1992)

[59] R.Dux, STRAHL User Manual (2000)

[60] A.G.Peeters, *Phys. Plasmas* **7** (2000), 268

[61] A.A.Ware, *Phys. Rev. Lett.* **25** (1970), 916

[62] R.C.Isler, *Nucl. Fusion* **24** (1984), 1599

[63] R.Dux et al., *Nucl. Fusion* **40** (2000), 1721

[64] J.Rapp et al., *Plasma Phys. Control. Fusion* **39** (1997), 1615

[65] F.Miskane et al., *Phys. Plasmas* **7** (2000), 4197

[66] J.Nycander et al., *Phys. Plasmas* **2** (1995), 2874

[67] D.R.Baker et al., *Phys. Plasmas* **5** (1998), 2936

[68] R.E.Waltz et al., *Phys. Plasmas* **4** (1997), 2482

[69] J.Weiland, *Collective modes in inhomogeneous plasmas*, IOP Publishing Ltd., Bristol & Philadelphia (2000)

[70] X.Garbet et al., *Turbulent particle transport in magnetized plasmas*, submitted to *Phys. Rev. Lett.* (2003)

[71] A.J.Wootton et al., *Phys. Fluids B* **2** (1990), 2879

[72] A.Zabolotsky et al., *Observation and empirical modelling of the anomalous particle pinch in TCV*, submitted to *Plasma Phys. Control. Fusion* (2003)

[73] Apollo Laser Inc., Operation and Service Manual, Model 35

[74] H.Reimerdes, *MHD stability limits in the TCV tokamak*, PhD thesis No. 2399, Ecole Polytechnique Fédérale de Lausanne, Switzerland (2001)

[75] F.Hofmann et al., *Nucl. Fusion* **28** (1988), 1871

[76] S.Franke, *Application of Thomson scattering at 1.06μm as a diagnostic for spatial profile measurements of electron temperature and density on the TCV tokamak*, PhD thesis No. 1654, Ecole Polytechnique Fédérale de Lausanne, Switzerland (1997)

[77] R.Behn et al., *Proc. 7th Int. Symp. Laser Aided Plasma Diagnostics*, Fukuoka (1995), 392

[78] S.Barry, *The extension of the FIR interferometer on TCV to a polarimeter and measure-*

ments of the Faraday rotation caused by the poloidal magnetic field, PhD thesis, National University of Ireland, Cork, Ireland (1997)

[79] D.Veron, *Infrared and millimeter waves*, Academic Press, New York, 1979

[80] M.Anton et al., *Plasma Phys. Control. Fusion* **38** (1996), 1849

[81] M.Anton et al., *Rev. Sci. Instrum.* **66** (1995), 3762

[82] R.J.Fonck et al., *Appl. Optics* **21** (1982), 2115

[83] R.C.Wolf et al., *JET report JET-P(95)* **34** (1995)

[84] M.A.Lennon, *J.Phys.Chem.Ref.Data* **17** (1988), 1285

[85] S.Gunter et al., *Nucl. Fusion* **39** (1999), 1793

[86] M.Z.Tokar et al., *Nucl. Fusion* **37** (1997), 1691

[87] T.Dudok de Wit et al., *Phys. Plasmas* **5** (1998), 1360

[88] J.Stoer and R.Bulirsh, *Introduction to numerical analysis*, Springer, New York (1980)

[89] F.H.Seguin et al., *Phys. Rev. Lett.* **51** (1983), 455

[90] M.Mattioli et al., *Nucl. Fusion* **38** (1998), 189

[91] Jet Team, *Proc. 15th International Conf. on Plasma Physics and Controlled Nuclear Fusion Research*, IAEA, Vienna (1995), 307

[92] M.W.Kissick et al., *Nucl. Fusion* **36** (1996), 1691

[93] K.W.Gentle et al., *Phys. Rev. Lett.* **74** (1995), 3620

[94] S.Fairfax et al., *Nucl. Fusion Supplement* **1** (1981), 439

[95] M.Greenwald et al., *Phys. Plasmas* **2** (1995), 2308

[96] S.Kalvin, *Phys. Lett. A* **232** (1997), 119

[97] V.I.Pistunovitch et al., *Jour. Nucl. Mat.* **248** (1997), 85

[98] D.Jablonski et al., *Jour. Nucl. Mat.* **241** (1997), 782

[99] E.Haddad et al., *Nucl. Fusion* **36** (1996), 613

[100]A.Weller et al., *Jet report JET-IR(87)* **10** (1987)

[101]F.L.Hinton et al., *Rev. Mod. Physics* **48** (1976), 239

[102]G.H.Golub et al., *Matrix computations*, The John Hopkins University Press, Baltimore (1988)

[103]C.S. Van Loan, *Numer. Math.* **46** (1985), 479

Acknowledgements

Curriculum Vitae

I was born in Fossano, Italy, on Sept. 17th, 1970. I attended primary, junior and high school in Savigliano, Italy where I obtained the "Maturita' Scientifica" in 1988. In the same year I started my university studies at the Politecnico di Torino where I graduated in 1994 in Nuclear Engineering with a thesis on the high temperature superconductors. Starting in 1995 I spent two years at CERN in Geneva as Scientific Associate, and I collaborated in the Material Support group, with the aim of defining the inner surface properties for particle accelerators. In Sept. 1997 I joined the TCV team in the Ecole Polytechnique of Lausanne for a PhD thesis in Plasma Physics, in the domain of non recycling impurity transport.